NASA-CR-191622

2

P. 130

NGR-559

THE DETECTION AND CHARACTERIZATION OF HIGH FREQUENCY AND HIGH WAVENUMBER SOLAR OSCILLATIONS

A DISSERTATION
SUBMITTED TO THE DEPARTMENT OF PHYSICS
AND THE COMMITTEE ON GRADUATE STUDIES
OF STANFORD UNIVERSITY
IN PARTIAL FULFILLMENT OF THE REQUIREMENTS
FOR THE DEGREE OF
DOCTOR OF PHILOSOPHY

By
David Neil Fernandes
June 1992

(NASA-CR-191622) THE DETECTION AND CHARACTERIZATION OF HIGH FREQUENCY AND HIGH WAVENUMBER SOLAR OSCILLATIONS Ph.D. Thesis (Stanford Univ.) 130 p
[illegible]
Unclas
[illegible]

THE DETECTION AND CHARACTERIZATION OF HIGH FREQUENCY AND HIGH WAVENUMBER SOLAR OSCILLATIONS

A DISSERTATION
SUBMITTED TO THE DEPARTMENT OF PHYSICS
AND THE COMMITTEE ON GRADUATE STUDIES
OF STANFORD UNIVERSITY
IN PARTIAL FULFILLMENT OF THE REQUIREMENTS
FOR THE DEGREE OF
DOCTOR OF PHILOSOPHY

By
David Neil Fernandes
June 1992

© Copyright 1992 by David Neil Fernandes
All Rights Reserved

I certify that I have read this thesis and that in my opinion it is fully adequate, in scope and in quality, as a dissertation for the degree of Doctor of Philosophy.

Philip H. Scherrer
(Principal Advisor)

I certify that I have read this thesis and that in my opinion it is fully adequate, in scope and in quality, as a dissertation for the degree of Doctor of Philosophy.

Robt V. Wagoner

Robert V. Wagoner

I certify that I have read this thesis and that in my opinion it is fully adequate, in scope and in quality, as a dissertation for the degree of Doctor of Philosophy.

Arthur B C Walker

Arthur B. C. Walker

Approved for the University Committee on Graduate Studies:

Abstract

Doppler shift measurements of the Na D_1 absorption line have revealed solar oscillations in a new regime of frequency and wavenumber. Oscillations of vertical velocities in the temperature minimum and low chromosphere of the Sun are observed with frequencies ranging up to 9.5 mHz. There is no evidence for chromospheric modes of 3 minute period. This indicates that the chromosphere does not form a good cavity for acoustic waves.

The fundamental-modes appear with wavenumbers up to 5.57 Mm^{-1} (equivalent spherical harmonic degree, 3877). The frequencies lie below the predicted values at wavenumbers above 1 Mm^{-1}. The values are in agreement with previous measurements that exist for wavenumbers up to 2.67 Mm^{-1}.

Spatial maps of velocity power show that high wavenumber oscillations are suppressed in active regions. The shape of the power depression indicates that wave motion is affected in the layer of atmosphere where the measurement is made. The f-modes are suppressed in the same way as p-modes, indicating that the mechanism for wave suppression affects velocity fluctuations. Mode frequencies are not affected by the magnetic fields by more than 50 μHz, the precision of the measurement.

Acknowledgments

In the course of my graduate student career at Stanford, I have made many friends, and benefited from the knowledge and experience of many people. My advisor, Phil Scherrer, has always made himself available for discussions, and shared his insight in the field. He has also provided guidance for this dissertation from beginning to end. I am grateful to him for encouraging my participation in workshops and conferences while, at the same time, giving me the freedom to explore my interests outside the field of solar physics. Dave Burke, my former advisor at the Stanford Linear Accelerator Center, deserves thanks as well, for giving me a solid grounding in experimental physics.

Ted Tarbell and Alan Title at the Lockheed Palo Alto Research Laboratories (LPARL) have both taken a personal interest in this project. They provided the instrument and expertise to make the observations, as well as many ideas and topics for research. They also offered many useful comments on this manuscript. All of the data analysis was done at LPARL, with support from Kermit Smith and Zoe Frank. I am especially grateful to Dick Shine for his help and consultation in software development.

I would like to thank Douglas Gough, Pawan Kumar, and Ed Lu for illuminating discussions that have greatly increased my understanding of helioseismology theories. Thanks also to Ellen Zweibel, Neil Hurlburt, and Colin Rosenthal for interesting discussions of the results, to Tim Brown, Göran Scharmer, and Louis Strous for their suggestions concerning data analysis, to Paco Armas and Rolf Kevar for their support at the Swedish Solar Observatory, and to Bob Wagoner for his suggestions for improving this manuscript. Margie Stehle, Gail Ragsdale, and Marcia Keating

have good-humoredly and patiently guided me through the mountains of paperwork and miles of redtape of Stanford administration.

I have enjoyed my years at Stanford, and learned a great deal thanks to the friendship and support of some wonderful people. My classmates and peers in physics, Anna Green, Bruce King, Robin & Pete Wright, Lee Anne Kowalski, and Steve Pollock helped me keep my sanity through a year of problem set hell, and *The Qual.*

Interaction with Columbaens, Synergites, and assorted new-age hippies has reshaped my views and changed my long-term goals. Suzanne Jones, Sally Otto, Matt Price, Neil Switz, and my sister, Karen, are all awesome, and I hope to be just like them when I grow up (without the long hair, though). Darlene Zanker, Greg Hollon, and Lise Schickel were part of a most memorable summer class at the Hopkins Marine Station, as was our instructor, Jim Watanabe. Leslie Roldan, Suttirat-Anne Larlarb, Sunit Mahajan, and Ann Fridlind from Columbae, and Ethan Pride, Cecil Scheib, and Myia Johnson from Synergy have all been willing to listen to my grumbling about *Writing* and, to provide me with distractions and diversions.

Finally, I wish to thank Peter Vitousek, Carla D'Antonio, and Jim Raich for advice and help getting me on my feet in a new field.

This work was funded by NASA contracts for SOUP (NAS 8-32805), OSL-CIP (NAS 5-26813), and SOI/MDI (NAS 5-30386), by NASA grant NGR-559, NSF grant ATM 90-22249, ONR grant N00014-89-J-1024, and by Lockheed Independent Research Funds.

Contents

Abstract iv

Acknowledgments v

1 Introduction 1

1.1 Wave Properties 2

1.1.1 Acoustic Waves 2

1.1.2 Surface Waves 4

1.2 High Frequency Modes 6

1.3 High Wavenumber Modes 8

1.4 Height of Observations 9

2 Measurement Techniques 11

2.1 Three-Point Measurements of Line Parameters 12

2.1.1 Algebraic Solution 13

2.1.2 Error Estimates 13

2.2 Four-Point Measurements of Line Parameters 14

2.2.1 Implementing the Algorithm 17

2.2.2 Spectral Simulation 20

2.2.3 Sources of Systematic Error 21

2.2.4 Statistical Error 25

2.2.5 Discussion of the Method 29

2.3 Magnetograms 30

2.3.1 Inverse Zeeman Effect 30

2.3.2 Longitudinal Field Measurement 30
2.4 Transform Methods 31
2.4.1 Practical Considerations 33
2.4.2 Apodization 34
2.4.3 Normalization 35
2.4.4 Statistical Error Estimates 35

3 Telescope and Instrumentation **36**
3.1 Telescope 36
3.2 Postfocus Instrumentation 36
3.2.1 Tunable Filter 36
3.2.2 CCD Camera 42
3.2.3 Image Stabilization System 43
3.3 Optical Layout 44
3.4 Modulation Transfer Function of the System 48
3.4.1 Entrance Pupil 49
3.4.2 CCD Camera 49

4 Observations **51**
4.1 Observing Procedure 51
4.2 Calibration Method 52
4.3 Solar Observations 55

5 Data Reduction **61**
5.1 Flat Fielding 62
5.2 CCD Flaw Correction 63
5.3 Image Rotation 63
5.4 Atmospheric Distortion 63
5.4.1 MTF Normalization 64
5.4.2 Destretching 66
5.5 Dopplergrams and Intensities 67
5.6 Image Drift 68

5.7 Angular Scale Determination 68

6 Measurements from Power Spectra **71**

6.1 Collapsing 3-d Power Spectra 74

6.1.1 Distance Scale Determination 74

6.1.2 Azimuthal Projection 76

6.2 Parametrization and Least-Squares Fitting 78

6.2.1 Fitting Procedure 78

6.2.2 Levenberg-Marquardt Method for Nonlinear Regression 80

6.3 Results of Fits 82

6.3.1 Background 82

6.3.2 Mode Frequencies 83

6.3.3 Mode Widths 87

6.3.4 Mode Power 88

6.3.5 Comparison of Magnetic and Nonmagnetic Regions 91

7 Spatial Distribution of Power **94**

7.1 Mode Masks 94

7.2 Results 95

8 Conclusions and Discussion **102**

8.1 Surfaces and Cavities 102

8.2 Waves in Magnetic Fields 103

8.3 Directions for Future Work 104

A Frequency Tables **106**

Bibliography **112**

List of Tables

4.1 Filter Parameters for SEISNAFE Sequence. 56

4.2 La Palma Observing Runs using SEISNAFE Sequence. 57

4.3 Filter Parameters for NAFAST Sequence. 57

A.1 Mode Frequencies from Dopplergrams 106

A.2 *f*-mode Frequencies from Intensities 110

List of Figures

1.1 Acoustic cutoff ω_c vs. k 3

1.2 Propagation of an acoustic wave in a plane-parallel atmosphere. From Gough (1983) 4

1.3 Temperature and density of the solar atmosphere. From Avrett (1992). 5

1.4 Mode frequencies vs. wavenumber with a chromospheric cavity present. From Ulrich & Rhodes (1977). 7

1.5 Profiles and contribution functions for the Na D lines. From Schleicher (1976) 10

2.1 Measurements of the Na D_1 line 12

2.2 Spectral profiles. 15

2.3 Ratio α vs. velocity 16

2.4 Ratio β vs. velocity 17

2.5 Transmission product for Lyot and Michelson filters vs. wavelength . 22

2.6 Transmission ratio $\int t_3\,d\lambda / \int t_1\,d\lambda$ as a function of *fwhm* of the Lyot filter. 22

2.7 Systematic error ϵ_v vs. velocity for line-depth variations 23

2.8 Systematic error ϵ_v vs. velocity for Lyot drifts 24

2.9 Systematic error ϵ_v vs. velocity for line-width increments: 0, 10, 20, 30% (α-only method). 24

2.10 Systematic error ϵ_v vs. velocity for line-width increments: 0, 10, 20, 30% (α, β method). 25

2.11 Geometry of modeled line asymmetry. 26

2.12 Depth of measured velocity vs. velocity for bisector shape *hwhm:* $-7.5, \ldots, 7.5$ mÅ (α-only method). 26
2.13 Depth of measured velocity vs. velocity for bisector shape *hwhm:* $-7.5, \ldots, 7.5$ mÅ (α, β method) 27
2.14 Statistical error σ_v vs. velocity for different line-widths (α-only method). 28
2.15 Statistical error σ_v vs. velocity for different line-widths (α, β method). 28
2.16 Measurement of Zeeman splitting 31

3.1 Schematic diagram of the Swedish 50 cm Vacuum Solar Telescope. From Scharmer *et al.* (1985). 37
3.2 Swedish Solar Observatory, La Palma (photograph) 38
3.3 Pulse propagation through a simple element. From Title & Rosenberg (1981). 39
3.4 Lyot filter with four elements. From Title & Rosenberg (1981). 39
3.5 Transmission vs. frequency for a Lyot filter. From Title & Rosenberg (1981) 40
3.6 Birefringent tuning element. From Title & Rosenberg (1981). 41
3.7 Transmission profile of the SOUP tunable filter 43
3.8 Relative transmission of the SOUP tunable filter 44
3.9 Optical bench setup (photograph) 46
3.10 Optical layout at Swedish Solar Observatory 47
3.11 Timing offset for images 48
3.12 Squared MTF of telescope and CCD detector 50

4.1 Line scan of Na D_1 Line using the CCD camera 53
4.2 Full-disk magnetogram from KPNO 58
4.3 Continuum intensity image of AR6181 59
4.4 La Palma magnetogram of AR6181 59
4.5 H α image of AR6181 60

5.1 Spatial frequency log-spectra of Na D_1 -40 mÅ filtergrams 65
5.2 Image drift during observing run. 69

6.1 Magnetogram of AR6181 showing subfields for study 72
6.2 Surfaces of power in $(\vec{k}, \nu)$ space. 73
6.3 Constant frequency slice of the 3-d power spectrum 75
6.4 Scaled velocity-power spectrum. From Fernandes *et al.* (1992) 77
6.5 Constant wavenumber slices of the 3-d power spectrum 79
6.6 Power law exponent for background fit 82
6.7 Background velocity power integrated over frequency. From Fernandes *et al.* (1992) 83
6.8 Calculated Doppler velocity vs. height. From Nesis & Mattig (1989) . 84
6.9 Measured mode frequencies (from velocity spectra): ν vs. $\log_{10} k$ . . . 85
6.10 Comparison of measured p-mode frequencies with Libbrecht *et al.* (1990) 86
6.11 Comparison of f-mode frequencies measured from velocity and intensity 87
6.12 Comparison of measured f-mode frequencies with Libbrecht *et al.* (1990) 88
6.13 Comparison of measured f-mode frequencies with theory 89
6.14 Frequency and ridge width vs. k 90
6.15 Velocity power vs. mode frequency. From Fernandes *et al.* (1992). . . 91
6.16 Mode frequency differences for canopy and quiet subfields 92
6.17 Mode frequency differences for sunspot and quiet subfields 93

7.1 Masks for power distribution maps 96
7.2 Comparison of power maps with magnetic fields 97
7.3 Power distribution for selected masks 98
7.4 RMS velocity vs. k 99
7.5 Slice of f-mode map 100
7.6 Comparison of f-mode slice with magnetic field 101

Chapter 1

Introduction

Solar oscillations were first observed by Leighton (1960), and were explained by Ulrich (1970) and Leibacher & Stein (1971) as being the superposition of many global standing waves. They have subsequently become an important tool for the determination solar structure. Measurements from helioseismology include the depth of the convection zone (Gough 1976), helium abundance in the convection zone (Christensen-Dalsgaard & Gough 1980), and internal rotation rate (Duvall *et al.* 1984; and others).

In the past, observational limitations have restricted helioseismology to long wavelength oscillations ($\gtrsim 4$ Mm). New instruments and techniques are beginning to make shorter wavelengths accessible to study. This opens the door to the exploration of structure at much smaller spatial scales. Stratification of the atmosphere, and vertical structure of magnetic regions are becoming active areas of investigation.

The term *solar oscillations* conventionally refers to two types of waves. Because they exist in a resonant cavity, these waves are also called modes (eigenmodes of the cavity). Compressional or acoustic waves (p-modes) are longitudinal waves with pressure as the restoring force. They have at least one nodal surface in the radial direction. Gravity waves have gravity as the restoring force. A special case of these are the surface waves. Because they have no radial nodes, surface waves are called fundamental modes (f-modes). These transverse waves propagate at the interface between two media. The remainder of the gravity waves are called g-modes. To date, g-modes have not been unambiguously detected, and they will not be considered here.

1.1 Wave Properties

1.1.1 Acoustic Waves

Sound waves can propagate vertically at frequencies greater than the acoustic cutoff or critical cutoff frequency ω_c. At lower frequency, a disturbance moves the whole atmosphere up and down in phase. Hence, waves do not propagate. At low horizontal wavenumber k $\left(k \ll \frac{1}{2H}\right)$, the acoustic cutoff can be expressed in terms of the adiabatic sound speed c and the density scale height H. For an isothermal atmosphere, the scale height is given by

$$H = \frac{c^2}{\gamma g} \tag{1.1}$$

and, the acoustic cutoff, by

$$\omega_c = \frac{c}{2H} \tag{1.2}$$

where g is the acceleration due to gravity; and, γ is the adiabatic index (Lamb 1932). Taking $c = 7.1$ km/s, $g = 278$ m/s^2, and $\gamma = \frac{5}{3}$ in the photosphere, we find $H = 110$ km and $\omega_c/2\pi = 5.2$ mHz for $k \ll 4.5$ Mm^{-1}.

In general, the acoustic cutoff depends on wavenumber. The relationship is given by (Kumar & Goldreich 1989)

$$\omega_c{}^2 = \left(\frac{c}{2H}\right)^2 \frac{1}{2}\left\{[1 + (2kH)^2] + \sqrt{[1 + (2kH)^2]^2 - \frac{96}{25}(2kH)^2}\right\} \tag{1.3}$$

Figure 1.1 shows ω_c as a function of k.

Oscillations with wavelength greater than a few Mm propagate around the sun without excessive dissipation. A periodic boundary condition is, therefore, imposed on these waves. The wave equation is separable into radial and angular parts and has eigensolutions of the form,

$$\Psi_{nlm}(r,\theta,\phi,t) = R_{nl}(r)\, Y_l^m(\theta,\phi)\, e^{-i\omega t} \tag{1.4}$$

$$n = 1,2,3,\ldots \qquad l = 0,1,2,\ldots \qquad m = -l, -l+1, \ldots, l$$

Short wavelength oscillations are dissipated before traveling around the sun. Moreover, at their small spatial scales, the medium can be approximated as plane-parallel.

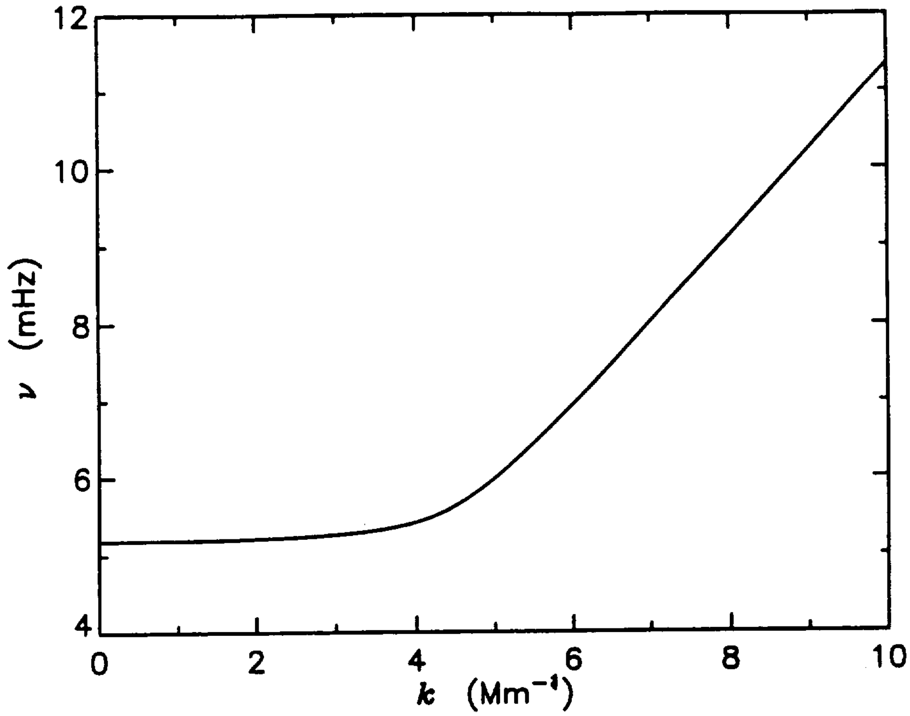

Figure 1.1: Acoustic cutoff ω_c vs. k

Plane waves, therefore, provide a more natural basis set for the horizontal eigenfunctions.

$$\Psi_{nk}(r,x,y,t) = R_{nk}(r)\, e^{i(\vec{k}\cdot\vec{x}-\omega t)} \tag{1.5}$$

The horizontal wavenumber $k = |\vec{k}|$ can be related to the spherical harmonic degree l as follows.

$$k = \frac{\sqrt{l(l+1)}}{R_{\text{sun}}} \tag{1.6}$$

Ray paths for a p-mode are diagrammed in figure 1.2. As waves travel downward, they encounter higher temperatures and an increasing sound speed. This causes them to refract back upward where they encounter increasing values of ω_c. When the wave can no longer propagate ($\omega < \omega_c$), it is reflected back down. The resonance condition is met when crests of downgoing waves are superposed on crests of refracted waves returning to the surface. For waves trapped in an adiabatic and polytropic layer (polytropic index = 4), this condition gives a dispersion relation of approximate form,

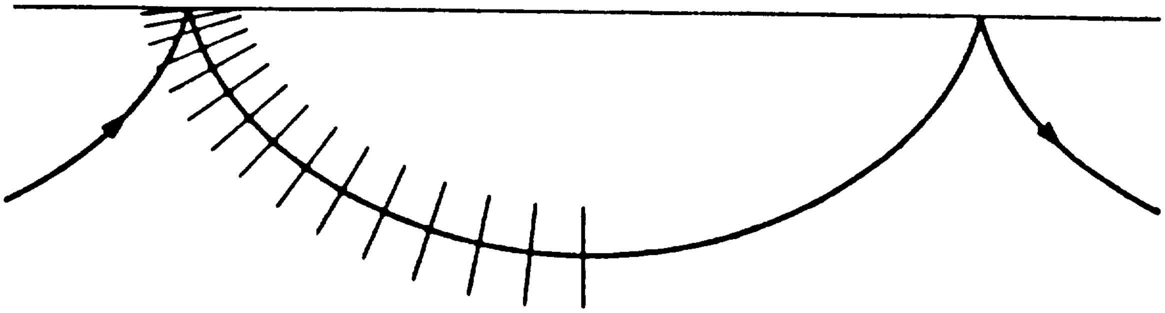

Figure 1.2: Propagation of an acoustic wave in a plane-parallel atmosphere. The wave is refracted as it propagates downward, and reflected at the surface. The maximum depth reached by the wave is called the lower turning point. From Gough (1983).

$$\omega^2 = \left(\frac{n}{2} + 1\right) gk \qquad n = 1, 2, 3, \ldots \tag{1.7}$$

where g is the acceleration due to gravity at the surface.

This dispersion relation can be measured directly from the ridges of power in a spectral decomposition (a plot of power vs. ω and k) of solar velocities or intensities. The exact relation depends on the variation of sound speed with depth.

The lower turning point d of the waves is approximately given by,

$$d = \frac{3\,(n+2)}{4k} \tag{1.8}$$

The excitation source of the p-modes is thought to be turbulent convection at the top of the convection zone. The efficiency of acoustic emission from convection is proportional to approximately the eighth power of the Mach number (Goldreich & Kumar 1988). Hence, only a few of the granules on the high velocity tail of the distribution are expected to contribute to the acoustic noise driving the p-modes (Brown 1991).

1.1.2 Surface Waves

Surface waves can propagate on the interface between convectively stable media (e.g., air over water). On the Sun, the transition region between chromosphere and corona provides such a boundary (Jones 1969). The model of Avrett (1992) describes the

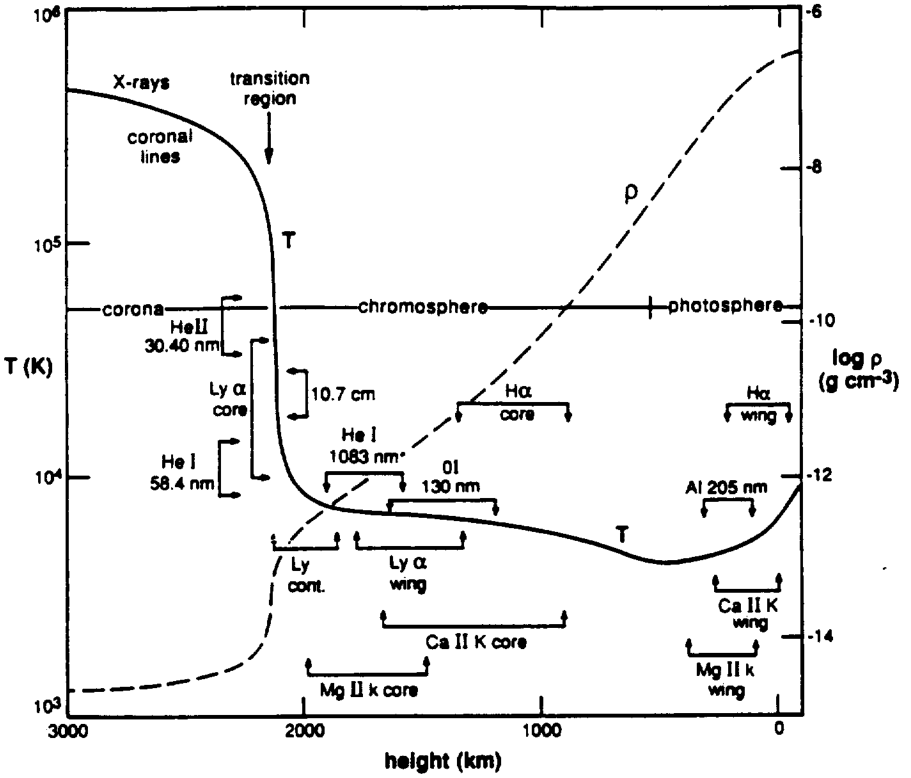

Figure 1.3: Temperature and density of the solar atmosphere. From Avrett (1992).

temperature and density discontinuities shown in figure 1.3. For purely vertical density stratification of a compressible fluid, surface waves obey the dispersion relation (Whitney 1958),

$$\omega^2 = gk \tag{1.9}$$

where g is the local acceleration due to gravity.

The simple form of this relation has prompted the remark that, "There is no interesting physics in the f-modes." It wasn't until f-modes were found not to obey the above relation at high wavenumber that this conclusion was reexamined. Libbrecht, Woodard & Kaufman (1990) found f-mode frequencies to lie below the predicted values for wavenumbers above 1.4 Mm^{-1}. At least three possible explanations exist, though numerical predictions have not yet been offered.

Campbell & Roberts (1989) and Evans & Roberts (1990, 1991) predict that a horizontal magnetic field in the chromosphere would increase the frequencies of the f-modes by increasing the restoring force on the surface waves. The sign of the frequency shift may reverse at high wavenumber, however, in a more realistic model of the chromosphere with an appropriate magnetic field structure (Roberts 1991).

Rosenthal (1992) finds that evanescent waves dissipated in the corona would cause power to leak out of the f-modes. This would lower the frequency of the modes at a given wavenumber by an amount dependent on the temperature difference between chromosphere and corona.

Finally, structures in the atmosphere, such as flux tubes and convection cells, violate the assumption of horizontal homogeneity. It is not known whether this should increase or decrease the mode frequencies (Gough 1992).

1.2 High Frequency Modes

For the purpose of discussion here, the high frequency regime includes modes with $\omega > \omega_c$, where $\omega_c/2\pi = 5.2$ mHz. This value of ω_c is the photospheric value for low wavenumbers. Because waves with $\omega > \omega_c$ can propagate, they are not trapped by the photosphere. So, in the model illustrated by figure 1.2, there should be no upper reflecting surface at frequencies > 5.2 mHz. Removal of the top surface of the cavity eliminates the possibility of resonance, and hence, the mode structure.

It was a surprise, therefore, when the p-mode ridges were found to continue above the acoustic cutoff (Jeffries *et al.* 1988; Libbrecht 1988; Duvall *et al.* 1991). Two explanations have been put forward for the origin of the high frequency ridges. Balmforth & Gough (1990) propose that strong reflection from the base of the corona defines a chromospheric cavity which couples to the subphotospheric cavity. Waves with frequency high enough to pass through the photosphere would still be trapped by the corona.

The presence of a chromospheric cavity has further consequences, however. The chromosphere is of order one wavelength in thickness for 5-minute modes; and waves of appropriate wavelength λ_r will resonate in this cavity. The p-modes propagate almost vertically in the atmosphere (angle of incidence ≈ 0). Thus, $\lambda_r = c/\nu_r$, independent of horizontal wavenumber. The chromospheric modes should, therefore, have a dispersion relation,

$$\omega = const. \tag{1.10}$$

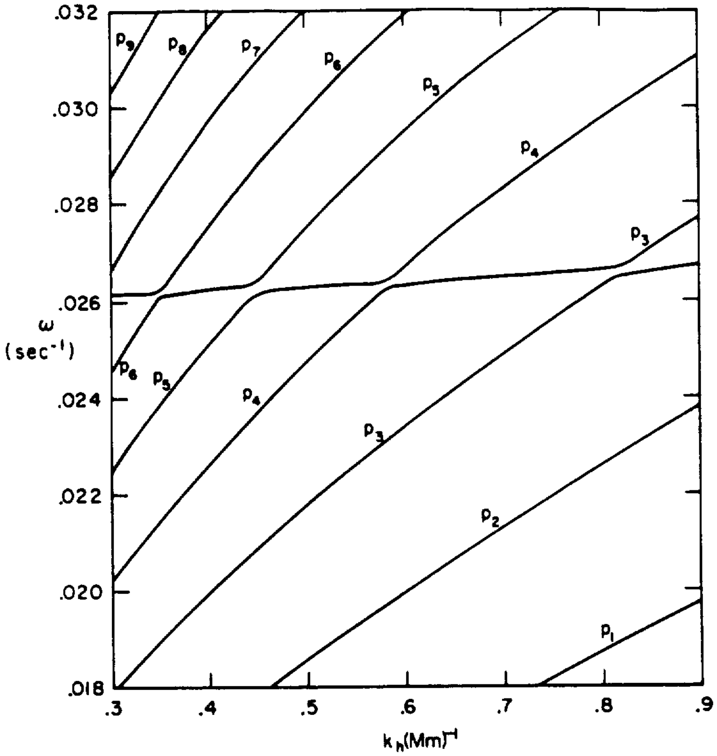

Figure 1.4: Mode frequencies vs. wavenumber with a chromospheric cavity present. From Ulrich & Rhodes (1977).

Ulrich & Rhodes (1977) found that the p-mode ridges would merge with a set of chromospheric modes at about 5.5 mHz. See figure 1.4. The p-modes would continue on above the 5.5 mHz band with an "avoided crossing" between the ridges above and below the chromospheric resonance.

Damé, Gouttebroze & Malherbe (1984) claim to have seen the chromospheric modes in Ca II K-line observations. Their power spectra are very noisy, however, and it is difficult to discern any definite ridges of power. Deming *et al.* (1986) find a peak in the one-dimensional power spectrum (power versus ω) at 4.3 mHz. Its significance is difficult to assess, though, without knowledge of the wavenumber dependence of the power. Woodard & Libbrecht (1991) do not find this peak in similar one-dimensional power spectra.

The other explanation for the high frequency ridges was offered by Kumar *et al.* (1990). They propose that waves are emitted isotropically from a source near the top of the convection zone. Waves traveling directly toward an overlying observed surface interfere (in Fourier space) with waves refracted upward from below to produce "mock modes." It must be stressed that this interference is not physical. In fact, the directly emerging wave trains and refracted wave trains may arrive at the surface at different times and in different places. The basis functions, used to represent the waves, can only distinguish time, modulo $2\pi/\omega$, and position, modulo $2\pi/k$. Frequencies of the mock modes can be used to determine the depth of the acoustic source layer (Kumar & Lu 1991).

The two models for high frequency waves can be distinguished by observations that resolve the ridge structure in the 5.5 mHz frequency range.

1.3 High Wavenumber Modes

Most of the literature in helioseismology refers to the (spherical harmonic) degree l of a mode rather than the wavenumber k. By convention, low degree refers to $0 \leq l < 4$, intermediate degree, to $4 \leq l < 100$, and high degree to $100 \leq l$. The oscillations presented in this dissertation have $500 < l \leq 3877$. By analogy with the electromagnetic spectrum, they should, perhaps, be called very high or ultrahigh degree, but I will stick to the term, high wavenumber.

Previous observations of the f-modes exist up to wavenumbers of 2.67 Mm^{-1} (Libbrecht, Woodard & Kaufman 1990). As mentioned above, the frequencies do not agree with equation 1.9 at wavenumbers above 1.4 Mm^{-1}. The variation of g with height accounts for only a 0.5% modification to equation 1.9. This is an order of magnitude less than the observed effect. It would be desirable to confirm the observational result and determine the trend at higher wavenumbers.

The size of structures that can be resolved by oscillations is roughly equal to the wavelength of the modes. For active regions, spatial scales range from 200 km (flux tubes) to 25 Mm (large sunspots). The corresponding wavenumbers range from 0.25 to 30 Mm^{-1}. Although the high end of this range is not attainable with any current instrument, there is still much room for investigation.

Woods & Cram (1981) have reported a suppression of oscillation amplitudes in plage as compared to quiet regions. Tarbell *et al.* (1988) and Title *et al.* (1992) find a suppression of both convective motions and wave amplitudes. The suppression of the oscillations coincides with the boundary of the photospheric magnetic field to within one wavelength.

Braun, Duvall & LaBonte (1987, 1988) and Braun *et al.* (1992b) have reported absorption of p-mode power by sunspots. The mechanism for this is not understood. Resonant absorption (Hollweg 1988; Chitre & Davila 1991), scattering to short wavelength (Bogdan & Zweibel 1987), and enhanced viscous dissipation (LaBonte & Ryutova 1992) are among the explanations offered. It is by no means clear whether only propagating acoustic waves below the photosphere are absorbed, or whether evanescent waves are also affected. A spatial map of oscillation amplitudes above the photosphere, where the magnetic fields are different, would help untangle the two effects.

Global oscillations have been found to have frequency shifts correlated with solar activity (Palle, Regulo & Roca Cortes 1989; Woodard *et al.* 1991). This may be due to a change in the shape of the cavity surface with sunspots present. Waves of a given frequency may have different wavenumbers within magnetic and nonmagnetic regions. Global measurements would then find a weighted average of the two dispersion relations. Comparison of high resolution observations in quiet sun and active regions could resolve this issue by direct measurement of dispersion relations in the two types of regions.

1.4 Height of Observations

Oscillations can be observed as fluctuations in intensity and line-of-sight velocity. Both p-modes and f-modes produce motions of gas particles, and cause Doppler shifts of absorption lines. Pressure fluctuations due to p-modes produce temperature/intensity fluctuations. The f-modes also produce intensity fluctuations, though the reason is not well understood. It may be that the $\sim$ 100 km vertical displacements of parcels of gas affect the process of absorption line formation.

Different parts of an absorption line are formed in different layers of the atmosphere. Hence, the height at which the velocities and intensities are determined depends on the positions in the absorption line at which measurements are made. In

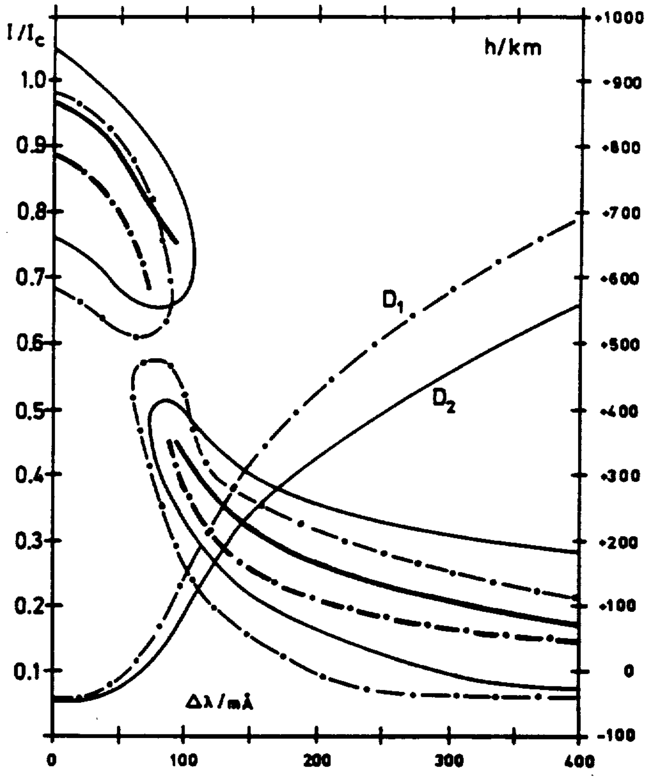

Figure 1.5: Na D line profiles on left hand scale. Contribution functions for emergent intensity on right hand scale. Thick lines show the maximum of the contribution function at each wavelength. Thin lines show 1/3 of the maximum of the contribution function. From Schleicher (1976).

the core of deep lines such as Na D_1, very little continuum light emerges from the photosphere. The height of a measurement, therefore, depends in the contribution function for the emergent line emission (Gurtovenko, Sheminova & Sarychev 1991; Schleicher 1992). This function is shown in figure 1.5.

The original intention of the observations described in chapter 4 was to make one set of measurements in the core and one in the wings of the Na D_1 line. Problems described in section 4.1 resulted in a measurement weighted mostly in the core (600–850 km), but with some contribution from below the temperature minimum (150–500 km).

Chapter 2

Measurement Techniques

Producing power spectra from uncalibrated images involves several stages of data analysis and reduction. This chapter reviews some general procedures, standard and nonstandard, for measuring line-of-sight components of velocity and magnetic field, and for determining wave amplitudes and phases. The details of calibration to remove artifacts of the instrument and atmosphere are left to chapter 5.

The line-of-sight velocity is found from the Doppler shift of an absorption line. The Doppler shift, in turn, is determined by measuring intensity as a function of wavelength at a series of fixed-wavelength positions in the absorption line. The more points in the measurement, the better the velocity estimate will be. Unfortunately, more points require proportionately more time to make the measurements, and geometrically more time to analyze them.

In this chapter are described two new techniques for making velocity images (dopplergrams) and line-center intensity measurements using three-point and four-point methods. The four-point method was developed for the *Solar Oscillations Investigation / Michelson Doppler Imager* (SOI/MDI) experiment for the *Solar and Heliospheric Observatory* (SOHO) spacecraft. It was not applied to the data used for this dissertation.

Images of line-of-sight magnetic field strength (magnetograms) are an important tool in this study. The tried and tested "two-point magnetogram" method is described below.

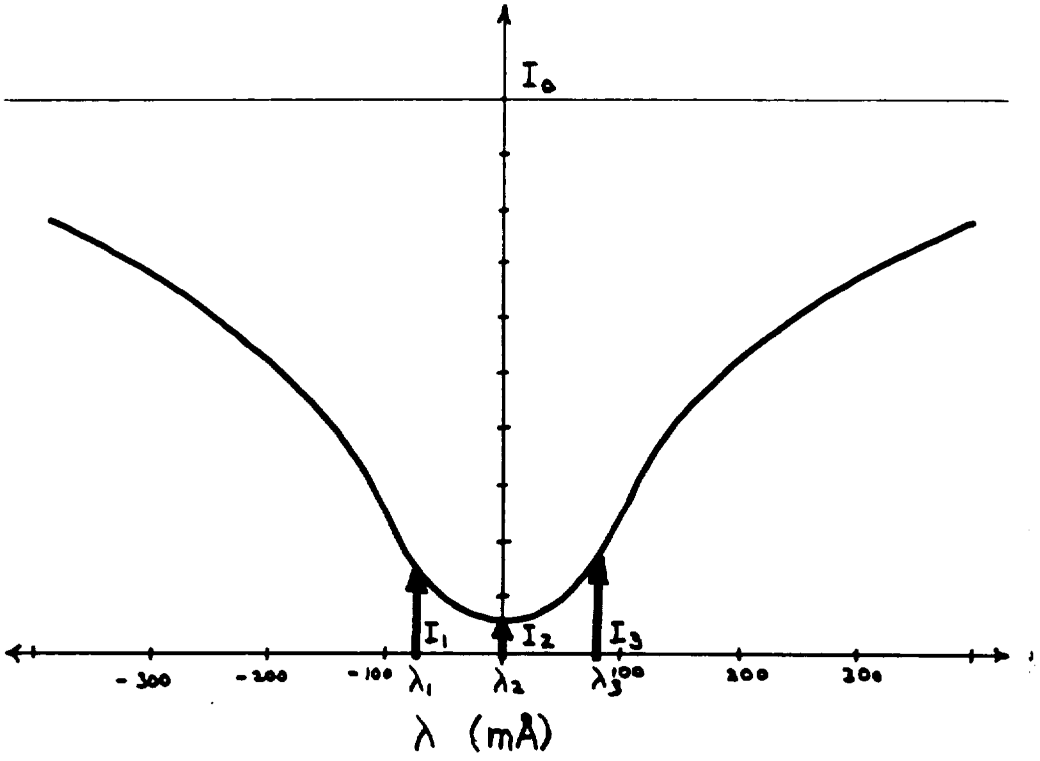

Figure 2.1: Measurements of the Na D_1 line

Finally, the Fourier transform is essential to the study of waves propagating in a linear medium. Procedures used to extract information about the oscillations are described in the last section of this chapter.

2.1 Three-Point Measurements of Line Parameters

The three-point method for finding Doppler shifts and line center intensities assumes a parabolic absorption line profile. This assumption is valid when the three intensity measurements are positioned relatively close to the line core. Figure 2.1 shows the measurements schematically for the Na D_1 (5896 Å) line. The Doppler shift and line center intensity are the x and y coordinates of the vertex, respectively.

2.1.1 Algebraic Solution

Assuming a parabolic line profile

$$I(\lambda) = I_0 + \left(\frac{\lambda - \lambda_0}{const.}\right)^2, \qquad (2.1)$$

we can solve for the vertex (λ_0, I_0) in terms of three intensities I_1, I_2, I_3 measured at wavelengths $\lambda_1, \lambda_2, \lambda_3$, respectively.

$$\lambda_0 = \frac{\overline{\lambda}_1 c_1 + \overline{\lambda}_3 c_3}{c_1 + c_3} \qquad (2.2)$$

$$I_0 = I_2 + \frac{(\delta_1 c_1 - \delta_3 c_3)^2}{4\delta_1\delta_3(\delta_3 - \delta_1)(c_3 - c_1)} \qquad (2.3)$$

$$\begin{aligned} \text{where}\quad \overline{\lambda}_1 &= \tfrac{1}{2}(\lambda_1 + \lambda_2), & \overline{\lambda}_3 &= \tfrac{1}{2}(\lambda_3 + \lambda_2), \\ \delta_1 &= \lambda_1 - \lambda_2, & \delta_3 &= \lambda_3 - \lambda_2, \\ c_1 &= \delta_1(I_3 - I_2), \text{ and} & c_3 &= \delta_3(I_1 - I_2). \end{aligned}$$

2.1.2 Error Estimates

The errors on the measured quantities I_1, I_2, I_3 are due to limitations of the instrument. The transmission of the tunable filter varies with wavelength as shown in figure 3.8. The phase of each Fourier component of this modulation is independent, and drifts with time. In addition, the wavelengths tuned by the filter are quantized in units of the smallest step size (3.14 mÅ). These sources of error were used in a simulation to estimate errors for the velocity and intensity.

The simulation assumed a parabolic line profile with parameters measured from the data. A range of velocities of ±2000 m/s with a flat distribution, and a range of line-center intensities of ±8% with a Gaussian distribution were used in the model. Intensity "measurements" I_1, I_2, I_3 were modeled assuming a random jitter of up to ±1.57 mÅ (flat distribution) in the location of each measurement, and assuming phases for the transmission modulation which varied randomly between sets of 3 filtergrams, but not within a set. The velocities and intensities were then calculated using equations 2.2 and 2.3. The errors had approximately Gaussian distributions with standard deviations,

$$\sigma_v = 300 \text{ m/s, and } \sigma_I = 7.7\%. \tag{2.4}$$

2.2 Four-Point Measurements of Line Parameters

An algorithm was developed for the SOI/MDI experiment to determine Doppler shifts using four measured intensities. The measurements are used to solve a system of simultaneous equations for the four absorption line parameters. Since computing time must be kept to an absolute minimum, the nonlinear equations are solved (numerically) using a look-up table approach.

The model included only the Lyot and Michelson filter elements, and the following parameters were used:

- Lyot filter: profile — Gaussian
  fwhm — 500 mÅ (see section 2.2.3)
- Michelson elements (2): profile — $\cos^2(k\lambda)\cos^2(2k\lambda)$
  fwhm — 105 mÅ
  where $k = \frac{2}{fwhm}\cos^{-1}\left(2^{-\frac{5}{6}}\left[\left(1+\sqrt{\frac{23}{27}}\right)^{\frac{1}{3}}+\left(1-\sqrt{\frac{23}{27}}\right)^{\frac{1}{3}}\right]\right)$
- Ni I (6768 Å) Line: profile — Gaussian
  fwhm — 130 mÅ
  depth — 58%
- Measurement Spacing — 85 mÅ (symmetric about nominal line center)

See figure 2.2 for illustration.

Four measurements are made at increasingly longer wavelengths across the absorption line, to yield intensities I_1 through I_4. The ratios, α and β, are formed as shown:

$$\alpha = \frac{I_1 - I_3}{I_4 - I_2} \tag{2.5}$$

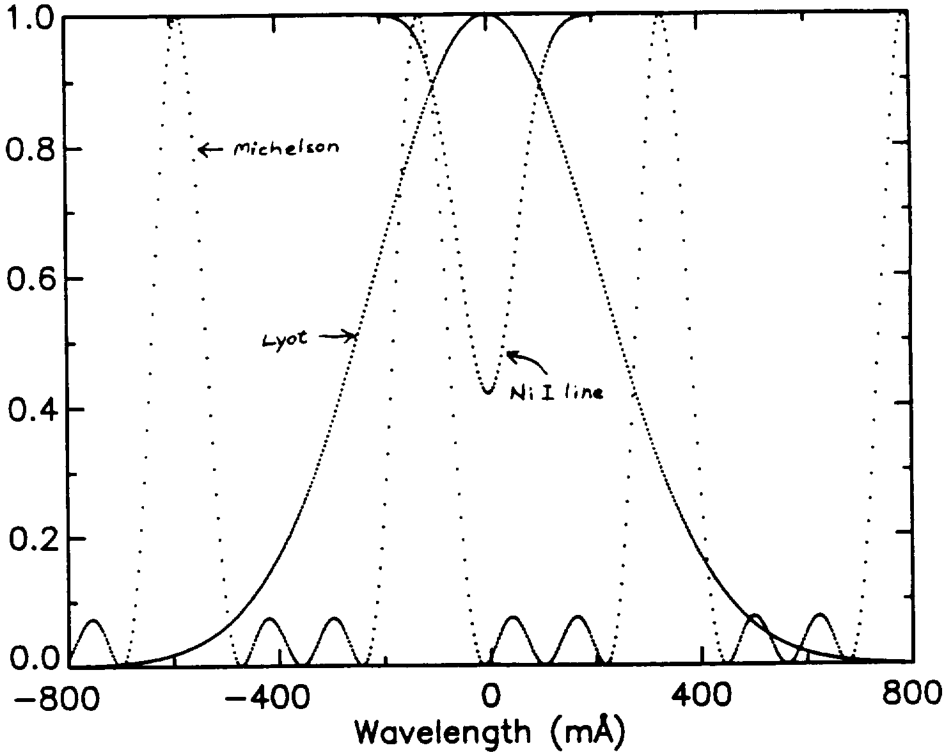

Figure 2.2: Spectral profiles.

$$\beta = \frac{I_2 - I_3}{I_1 - I_4} \tag{2.6}$$

The quantities α and β are independent of CCD dark current and gain variations. They are also independent of continuum intensity and line-depth if a suitable choice is made for the Lyot filter profile (see section 2.2.3).

We can solve exactly for the Doppler shift λ_0, line depth d, and continuum intensity I_0 if we assume a cosine shaped absorption line with measurement spacing equal to the *hwhm*:

$$I(\lambda) = I_0 \left[1 - \frac{d}{2}\left(\cos\frac{\pi(\lambda - \lambda_0)}{fwhm} - 1\right)\right] \tag{2.7}$$

Solving, we find,

$$\lambda_0 = fwhm \cdot \left(\frac{1}{4} - \cot^{-1}\alpha\right) \tag{2.8}$$

$$I_0 = \frac{1}{2}(I_1 + I_3 - s) \tag{2.9}$$

$$d = \frac{s}{I_0} \tag{2.10}$$

where $s = \sqrt{(I_1 - I_3)^2 + (I_4 - I_2)^2}$

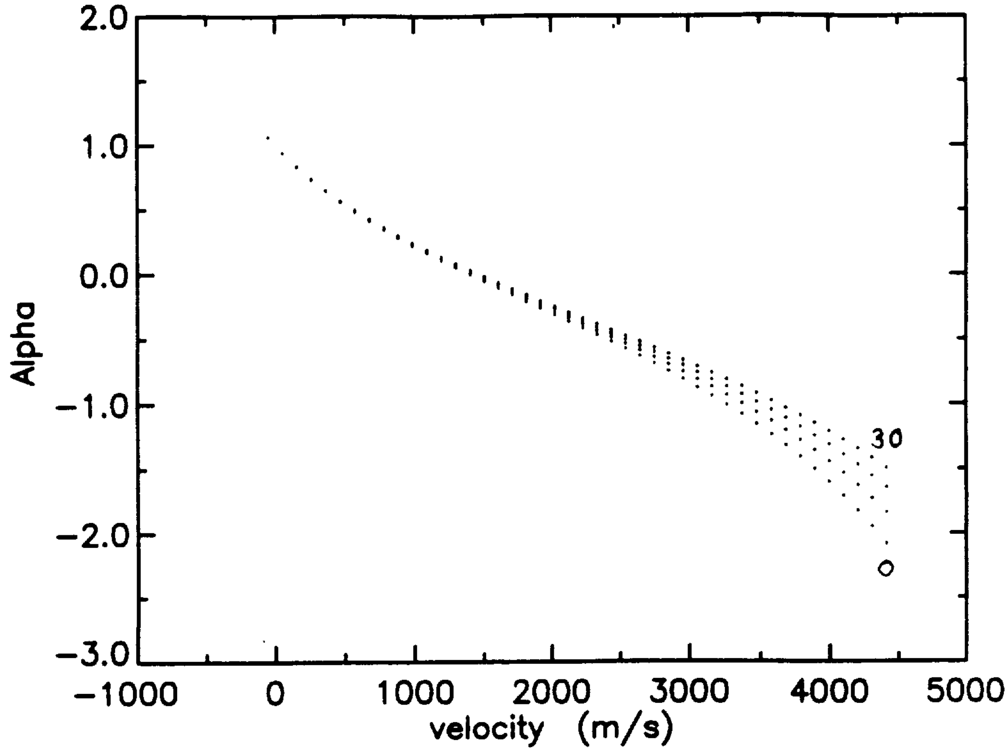

Figure 2.3: Ratio α vs. velocity for width increments: 0, 10, 20, 30%.

Note that α has a one-to-one correspondence with the ratio $r = \frac{(I_1-I_3)-(I_4-I_2)}{(I_1-I_3)+(I_4-I_2)}$ which appears in the SOI/MDI proposal (i.e., $r = (\alpha-1)/(\alpha+1)$). Hence determining the velocity from α alone is equivalent to determining it from $\tan^{-1} r$.

For a Gaussian line-profile,

$$I(\lambda) = I_0\left[1 - de^{-\frac{(\lambda-\lambda_0)^2}{2\sigma^2}}\right] \tag{2.11}$$

$$\text{where } \sigma = fwhm/2.36$$

The ratios α and β are plotted as functions of velocity for different line-widths in figures 2.3 and 2.4, respectively. It is apparent that the velocity determined from α alone would be in error if the calibration table were not made for the "right" line-width.

This caveat can be removed by determining the velocity v from both α and β: $v = v(\alpha, \beta)$. An algorithm for doing this is outlined below.

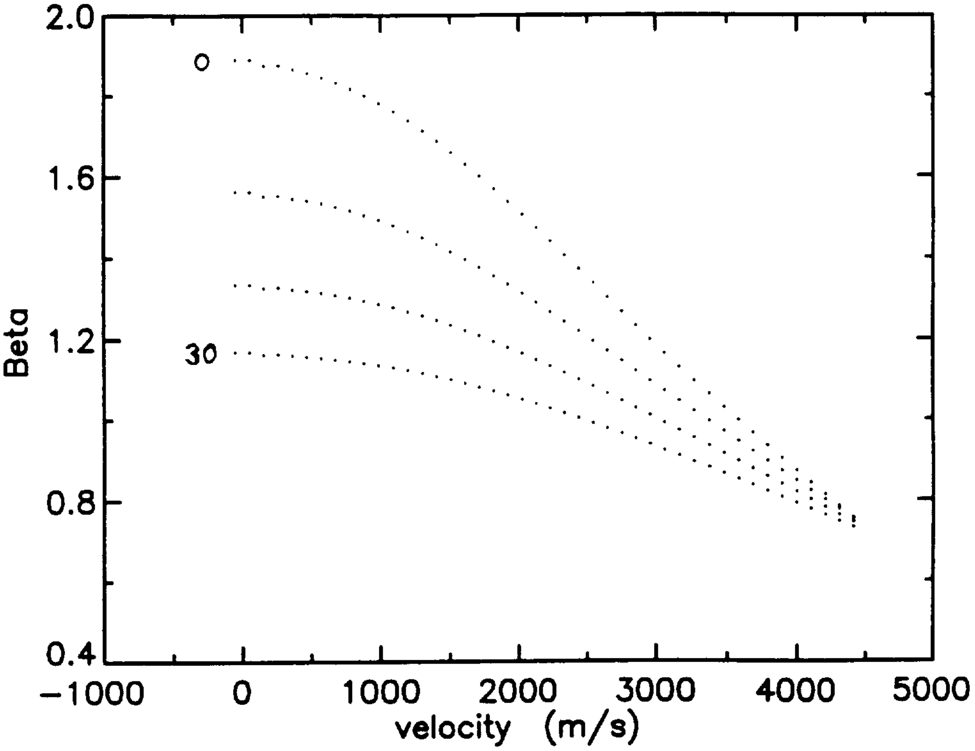

Figure 2.4: Ratio β vs. velocity for width increments: 0, 10, 20, 30%.

2.2.1 Implementing the Algorithm

Look-Up Table Approach

It is possible in principle to compute velocity by using a two-dimensional look-up table in α and β (i.e., $v = v(\alpha, \beta)$). This, however, would require an inordinate amount of memory ((12 bits in α) × (9 bits in β) = 2M words) to achieve an accuracy of a few m/s. A better strategy is to take advantage of the fact that α, alone, provides a pretty good estimate of velocity; and write:

$$v(\alpha, \beta) = v_1(\alpha) + v_2(\alpha, \beta) \tag{2.12}$$

where v_2 is a correction to the velocity v_1 and, hence, does not vary with α as quickly as does v_1.

This approach can achieve an accuracy similar to the previous approach but with much less memory overhead. The table, $v_1(\alpha)$, requires a 12 bit address; and the table, $v_2(\alpha, \beta)$, requires 7 bits in α by 9 bits in β (this has not been optimized); for a total of 66k words.

Domain and Range of α and β

The ratio α has a pole in the negative velocity-domain (i.e., a red-shifted line). To avoid this, a test is made to determine the sign of the velocity. For positive velocities: $\alpha = \frac{I_1 - I_3}{I_4 - I_2}$. For negative velocities: $\alpha = \frac{I_4 - I_2}{I_1 - I_3}$.

$$\text{The velocity is negative if and only if: } I_1 - I_3 > I_4 - I_2 \tag{2.13}$$

As can be seen from figure 2.3, α covers a more-or-less symmetric range about zero. Therefore, it can be scaled-up to provide an address for a look-up table without having to subtract an offset.

The function β is symmetric in the velocity domain and is continuous for symmetric line profiles. For asymmetric lines (and noisy lines) β has a pole near $v = 0$. In practice this does not cause problems because, near $v = 0$, v is independent of β (i.e., $v_2(\alpha, \beta) \approx 0$ for small v). An offset may have to be subtracted from β when scaling it for use as an address.

Finally, note that:

$$\beta = \frac{I_2 - I_3}{I_1 - I_4} = \frac{(I_1 - I_3) - (I_4 - I_2)}{(I_1 - I_4)} - 1 \tag{2.14}$$

Hence, both α and β can be obtained from the differences $(I_1 - I_3)$, $(I_1 - I_4)$, and $(I_4 - I_2)$.

The Algorithm

It is assumed here that the differences: $A_1 = I_1 - I_3$, $A_2 = I_1 - I_4$, and $A_3 = I_4 - I_2$ have been accumulated in image buffers.

```
For all pixels:

    Calculate $\beta$ and sign of velocity:

        $numerator = A_1 - A_3$
        $sign = \begin{cases} -1, & \text{if } numerator \geq 0; \\ +1, & \text{otherwise.} \end{cases}$
        $\beta = \frac{numerator}{A_2} - C_1$
```

Calculate α:

$$\alpha = \begin{cases} \frac{A_1}{A_3}, & \text{if } sign > 0; \\ \frac{A_3}{A_1}, & \text{otherwise.} \end{cases}$$

Calculate velocity:

$$v = sign \cdot [V_1(C_2\,\alpha) + V_2(C_3\,\alpha, C_4\,\beta)]$$

$C_1, \ldots, C_4$ are constants; V_1 and V_2 are look-up tables.

It should be noted that noise in the data may cause a "division by zero" error in the algorithm.

Constructing the Calibration Tables

The following procedures are used to construct the calibration tables V_1 and V_2. Parameters used for this study appear in square brackets.

The table $V_1(\alpha)$ is made for a line-profile of nominal width [130 mÅ] as follows:

1. Calculate α for a representative number [44] of discreet (evenly spaced) velocities ranging between some number slightly less than zero [-40 m/s] and some number slightly larger than the largest velocity expected from the data [4500 m/s].
2. Invert the table of α versus v to get a table of v versus α.
3. Interpolate (cubic spline) between the endpoints to get $V_1(\alpha)$, a table of velocities for an evenly spaced abscissa α.

The table $V_2(\alpha, \beta)$ is made for the same range of velocities as is V_1; and, for a given range of widths [100 to 295 mA]. The minimum width should not be less the measurement spacing [85 mA].

There are two "unphysical" regions in the table V_2. The highest values of α cannot occur with the highest values of β, and the lowest values of α cannot occur with the lowest values of β. These portions of the table will not normally be addressed by the Doppler algorithm.

V_2 is calculated as follows:

1. Calculate α and β for a representative grid of velocities [22] and widths [14].
2. Interpolate (spline) to get a much finer grid [512 in velocity by 256 in width].
3. For each "real" velocity v [512 of them] calculate the velocity correction v_2:

$$v_2 = v - V_1(\alpha)$$

   using the table $V_1(\alpha)$ computed above.
4. Sort the ordered triplets (v_2, α, β) into a 2-dimensional table $V_2(\alpha, \beta)$, keeping track of how many times each bin gets filled.
5. Fix uncooperative bins:
   a) If a bin accumulated more than one value of v_2, normalize to get the "average" v_2 for that (α, β).
   b) If a bin in a "physical" region did not get filled [there were 6 of them], interpolate [linearly] using adjacent bins.
   c) Fill "unphysical" bins with the value of v_2 from the nearest "physical" bin. This is done because noise in a measurement may produce an ordered pair (α, β) which does not lie quite where it should in the table.

Tables V_1 and V_2 were made in units of m/s, and rounded to the nearest integer.

2.2.2 Spectral Simulation

The instrument and Doppler algorithm were simulated in order to determine the magnitude of statistical and systematic errors. The simulation program stored the line and transmission profiles in single-precision 512-element tables covering the range ±800 mÅ about nominal line-center. The intensities, $I_1, \ldots, I_4$, were calculated for a discrete set of velocities as follows:

1. Offset the index of the line-profile table to simulate a Doppler shift.

2. Take the product of the transmission-profile and the offset line-profile.
3. Integrate [sum] over wavelength to get "measured" intensity.

The Riemann interval and limits of integration were varied to verify that they did not affect the results.

The error estimates are described in the next two sections.

2.2.3 Sources of Systematic Error

Line-Depth Variations

The ratio α will be sensitive to variations in line depth if measurements I_1 and I_3 (or I_4 and I_2) do not integrate the same amount of continuum.

Figure 2.5 shows the transmission through the Lyot and Michelson filters as a function of wavelength for the first and third measurements. The ratio of integrals of these curves is plotted as a function of Lyot filter *fwhm* (assuming a Gaussian Lyot-profile) in figure 2.6. The two integrals are equal when the Lyot *fwhm* is $\sim$ 625 mÅ. They are different by 2% when the *fwhm* is 500 mÅ.

This 2% difference causes a velocity error $\epsilon_v$which depends on line-depth as shown in figure 2.7. If the Lyot *fwhm* were 400 mÅ, ϵ_v would be larger by a factor of 4.

Lyot Filter Drift

If the Lyot filter profile drifts in wavelength space, the four measured intensities may not integrate the same amount of continuum. This would give erroneous values for α and β and, hence, v. To eliminate this source of error the transmission profile $t_{lyot}(\lambda)$ should satisfy:

$$\int t_{lyot}(\lambda - \delta_\lambda)\, t^i_{mich}(\lambda)\, d\lambda = constant \qquad i = 1, \ldots, 4 \tag{2.15}$$

for some small range δ_λ over which the Lyot filter might drift; $t^i_{mich}(\lambda)$ is the transmission of the Michelson filter at wavelength setting i;

For a Gaussian Lyot-profile, it turns out, this condition is more or less satisfied for the same *fwhm* that minimizes ϵ_v due to line-depth variations. The reason can be

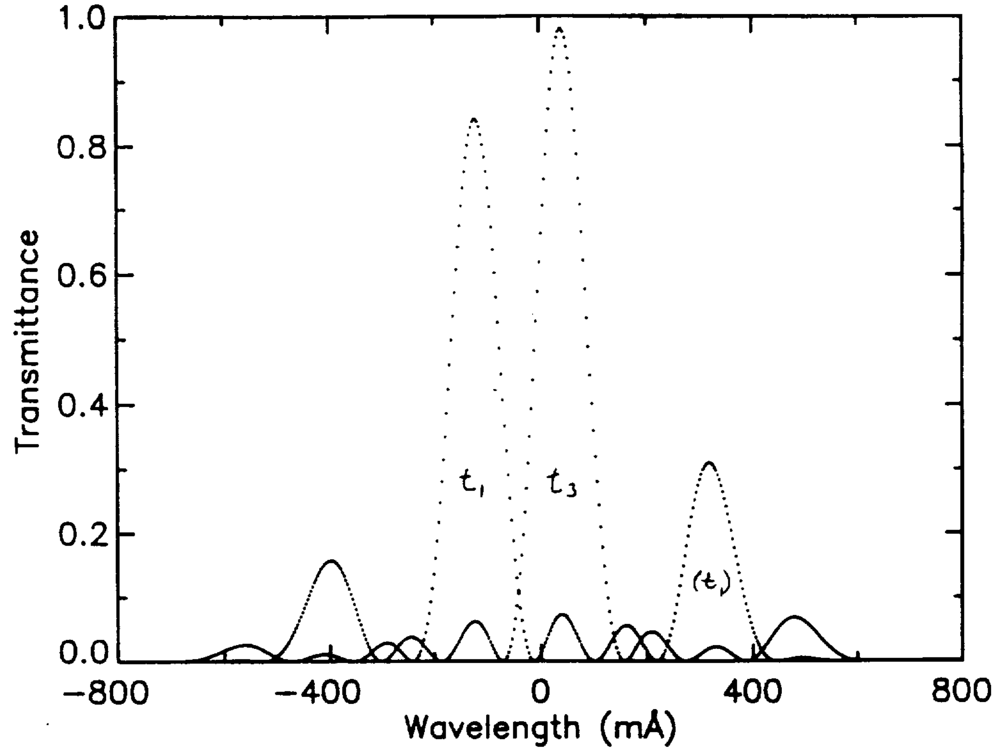

Figure 2.5: Transmission product for Lyot and Michelson filters vs. wavelength. t_1 and t_3 are the transmission profiles for measurements I_1 and I_3.

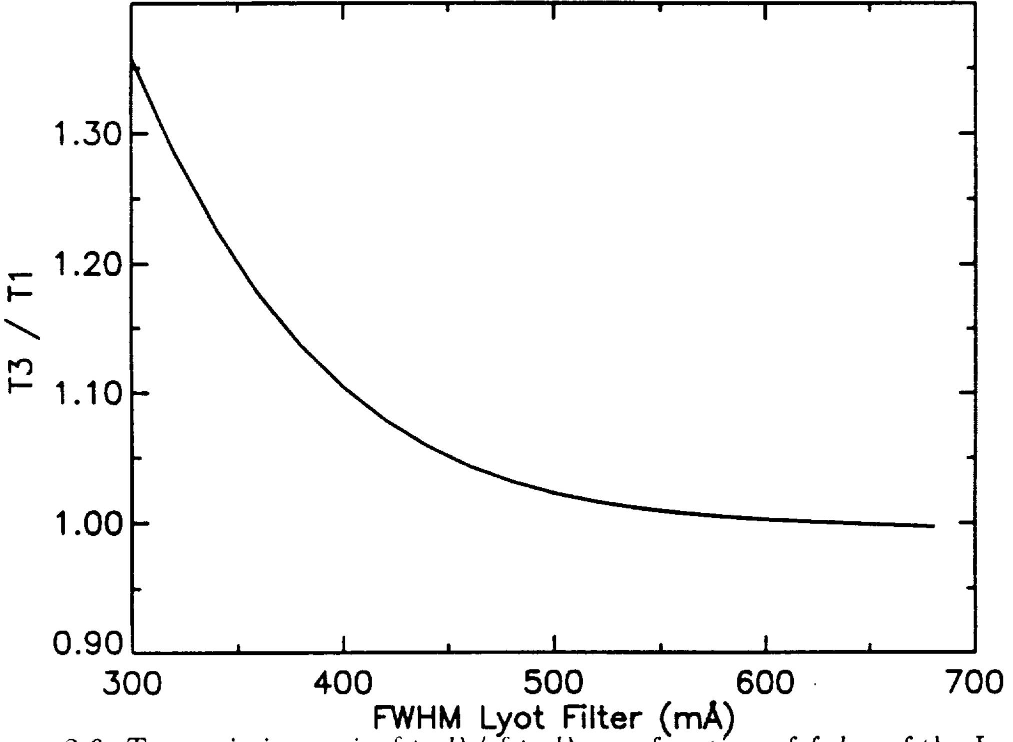

Figure 2.6: Transmission ratio $\int t_3\,d\lambda / \int t_1\,d\lambda$ as a function of *fwhm* of the Lyot filter.

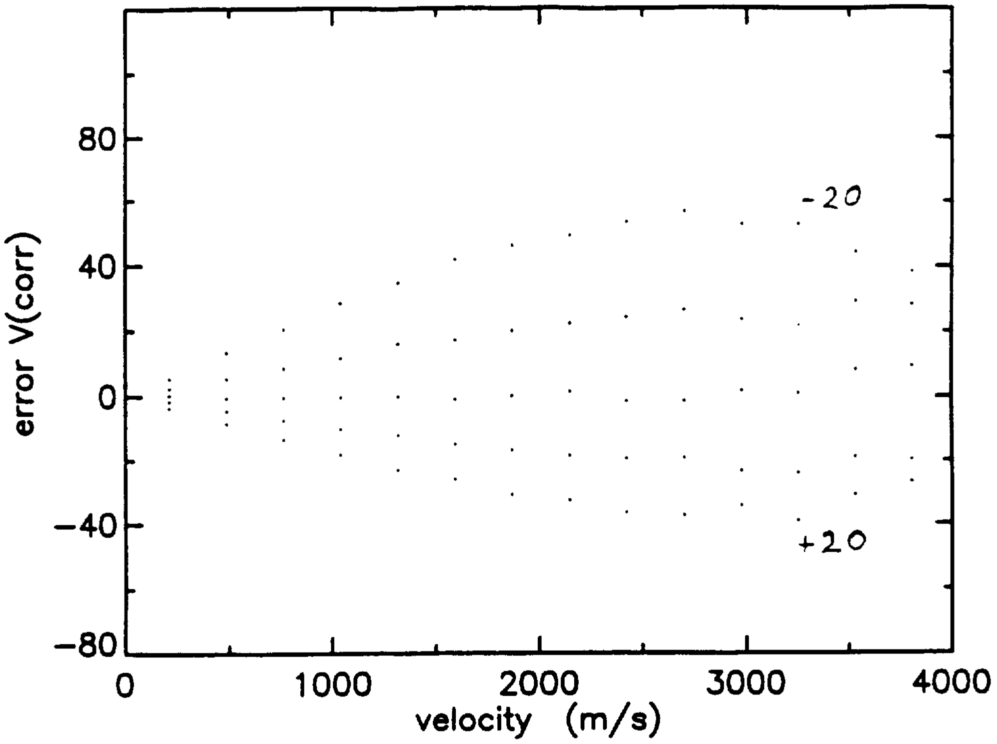

Figure 2.7: Systematic error ϵ_v vs. velocity for line-depth increments $-20, -10, 0, 10, 20\%$.

seen from figure 2.5. For transmission profile, t_1, if the Lyot profile shifts to the left (right), any increase (decrease) in the area under the main-lobe is compensated by a decrease (increase) in the area under the largest side-lobe. Transmission profile t_3 is unchanged to first order since it lies close to the maximum of the Lyot-profile.

Figure 2.8 shows ϵ_v for 8 mÅ offsets of the Lyot filter.

Line-Width Variations

As stated above, if α alone is used to compute v, an error will be introduced which depends on the line-width. Figure 2.9 shows the error incurred if the line-width is 10, 20, and 30% larger than the nominal width for which the calibration table was made. If both α and β are used, the error is reduced to a few m/s as shown in figure 2.10.

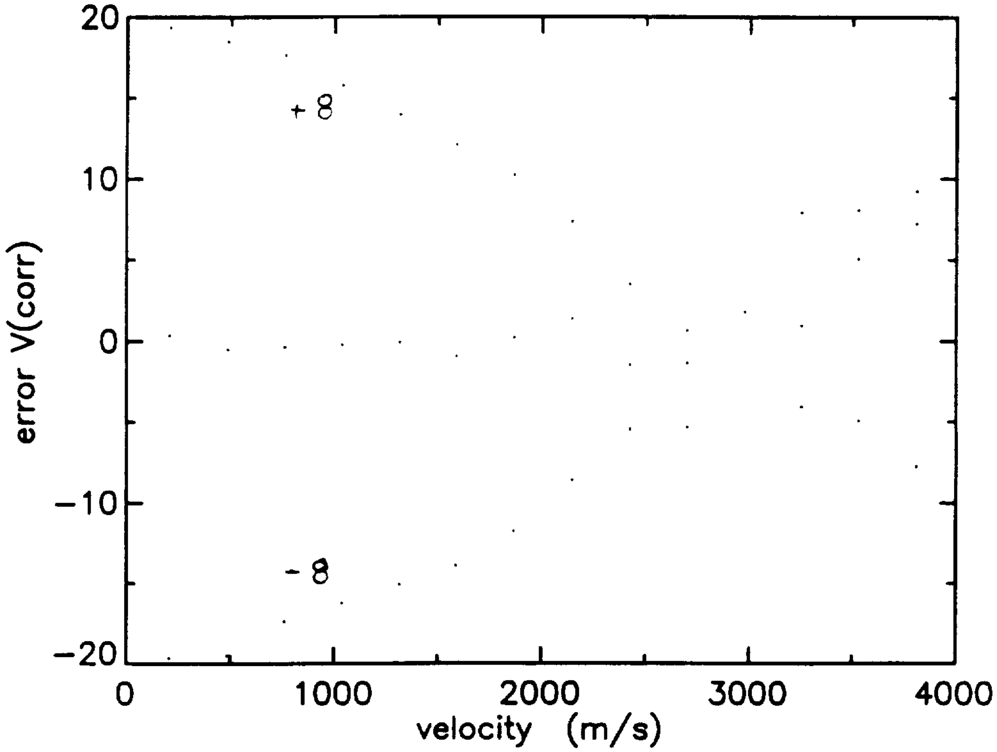

Figure 2.8: Systematic error ϵ_v vs. velocity for Lyot drifts: $-8, 0, 8$ mÅ.

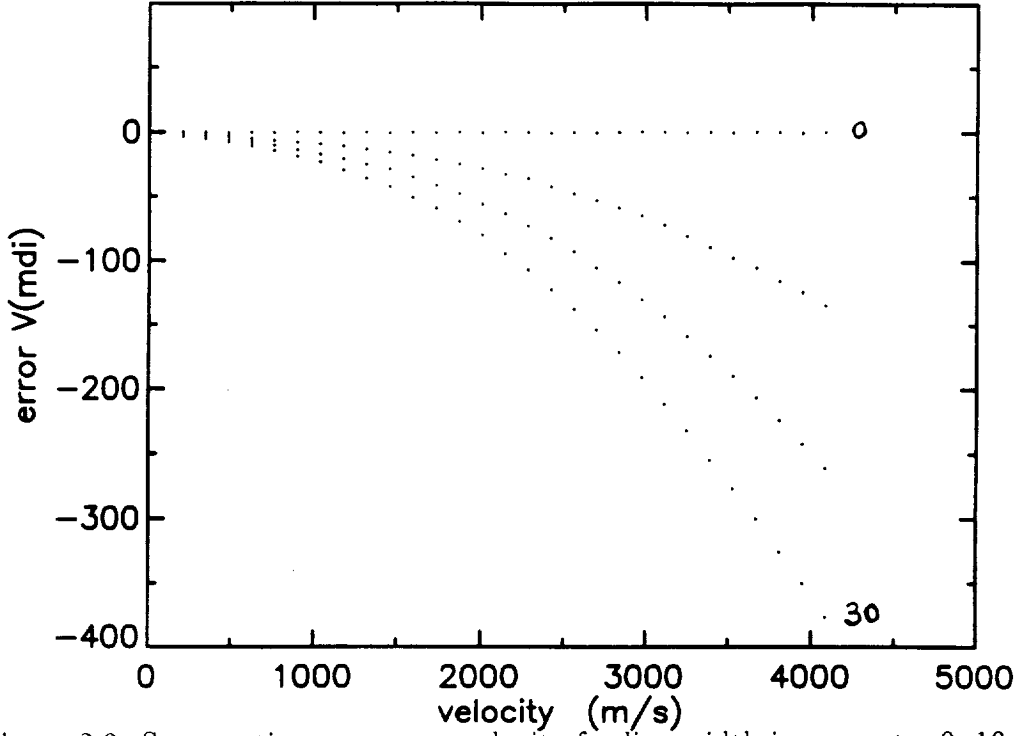

Figure 2.9: Systematic error ϵ_v vs. velocity for line-width increments: 0, 10, 20, 30% (α-only method).

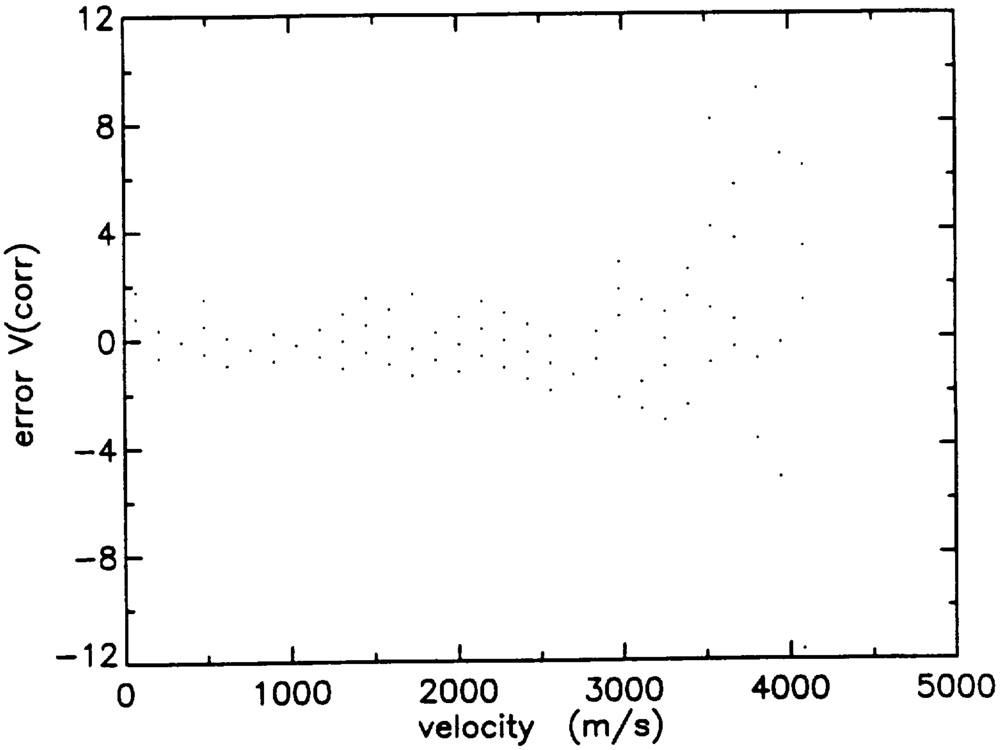

Figure 2.10: Systematic error ϵ_v vs. velocity for line-width increments: 0, 10, 20, 30% (α, β method).

Line-Asymmetries

The effect of line-asymmetry was explored by using a line-profile with a Gaussian-shaped bisector as shown in figure 2.11. It was found that the depth at which the velocity is measured depends on the velocity, but is independent of bisector shape. The velocity dependence is plotted for different bisector shapes in figure 2.12 (α-only method), and figure 2.12 (α, β method). Note that ϵ_v does depend on the precise shape of the bisector, but its magnitude cannot be determined until a measurement is made of the bisector shape at the spatial resolution of the MDI instrument.

2.2.4 Statistical Error

Statistical errors were found by a standard propagation of error calculation. Derivatives of the functions $v_1(\alpha)$ and $v_2(\alpha, \beta)$ were approximated by finite differences.

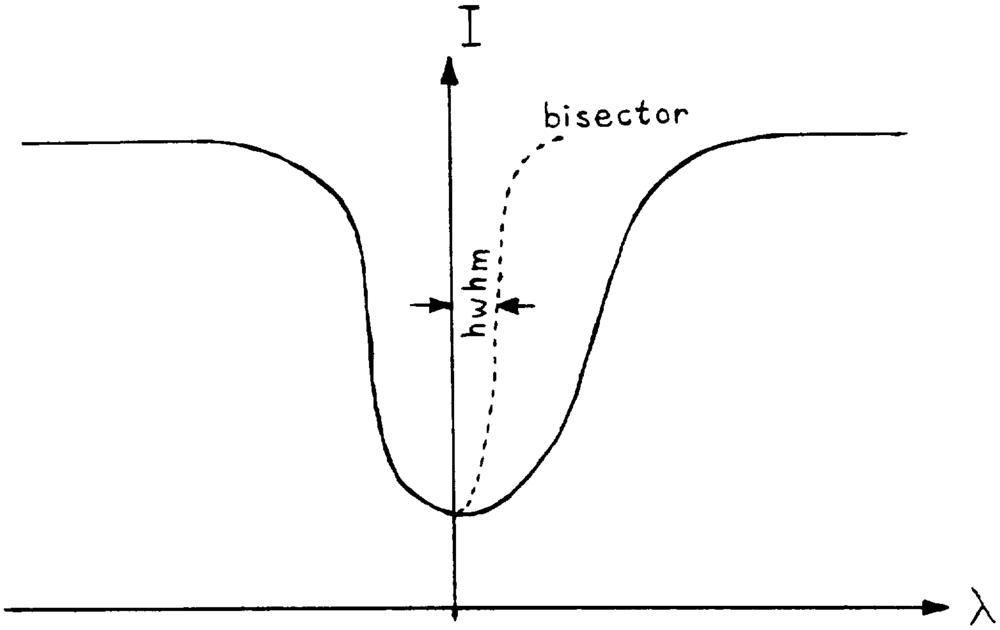

Figure 2.11: Geometry of modeled line asymmetry.

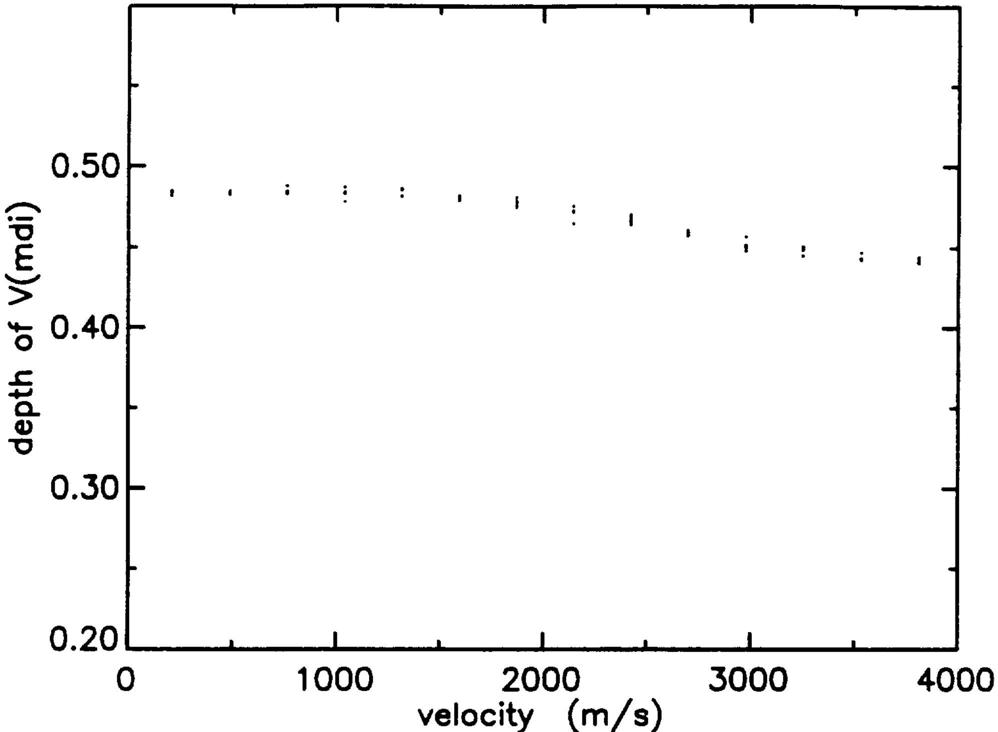

Figure 2.12: Depth of measured velocity vs. velocity for bisector shape *hwhm*: −7.5, …, 7.5 mÅ (α-only method).

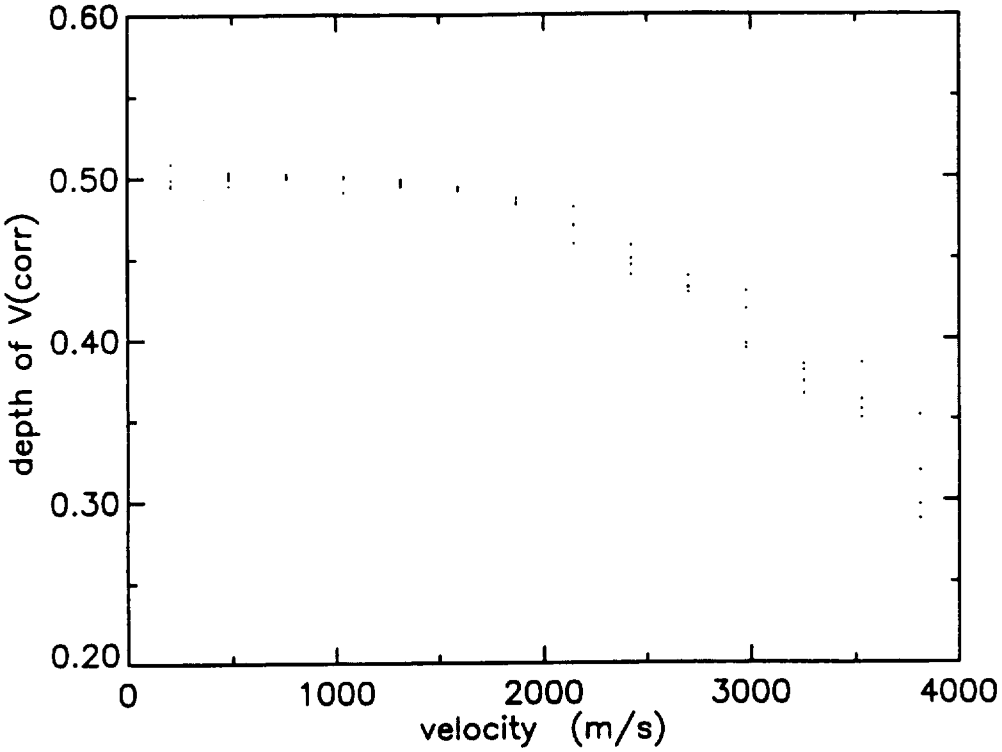

Figure 2.13: Depth of measured velocity vs. velocity for bisector shape *hwhm:* $-7.5, \ldots, 7.5$ mÅ (α, β method)

For a sinusoidal line-profile with delta-function transmission-profiles, the statistical error σ_v can be written down in a form like that shown in the SOI/MDI proposal.

$$\sigma_v = \frac{2cs}{\pi\lambda} \frac{1}{\sqrt{I_0}} \frac{\sqrt{2-d}}{d} \tag{2.16}$$

where, s is the measurement spacing; d, the line depth; and, I_0, the number of photons collected at continuum intensity (half the well depth for the CCD).

Numerically, σ_v from this calculation is 16 m/s (with $d = .58$, $I_0 = 10^5$). The finite spectral resolution, however, tends to wash out the signal. For Gaussian transmission-profiles (*fwhm* = 100 mÅ), σ_v is 25 m/s. For the transmission-profiles in figure 2.5, σ_v is 30 m/s as shown in figure 2.14 (α-only method) and figure 2.15 (α, β method). The scatter in figure 2.15 is due to the method by which the calibration table $V_2(\alpha, \beta)$ is calculated.

The sudden increase of σ_v for velocities above 3500 m/s is due to the increasing dependence of v on β together with the fact that β is only allotted 9 bits in the calibration-table address. Allotting more bits to β would proportionately reduce this

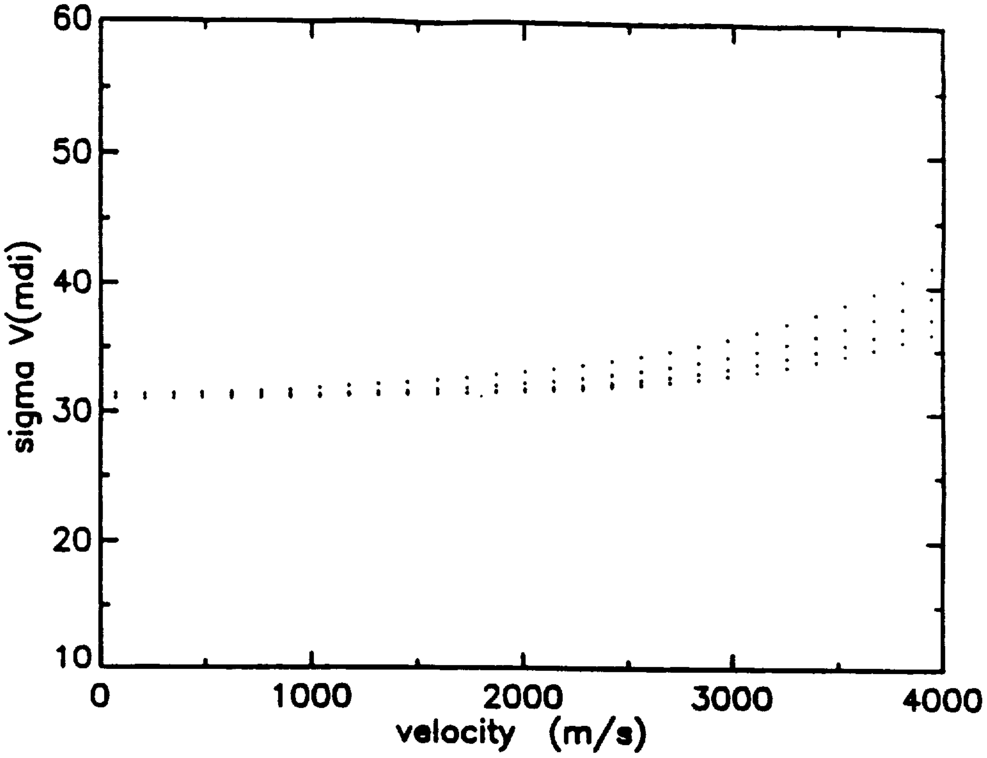

Figure 2.14: Statistical error σ_v vs. velocity for different line-widths (α-only method).

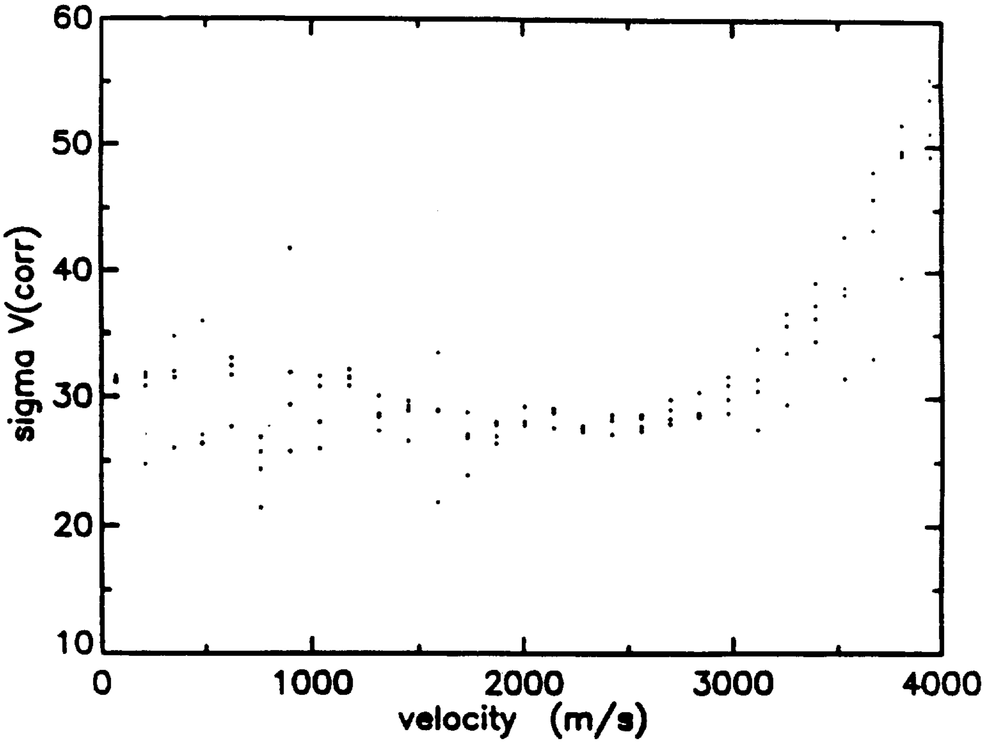

Figure 2.15: Statistical error σ_v vs. velocity for different line-widths (α, β method).

behavior.

2.2.5 Discussion of the Method

The studies indicate that velocity errors due to line-depth variations and Lyot filter drift can be minimized by proper design of the Lyot filter profile. In principle it should be possible to eliminate the errors entirely, though only a crude optimization has been done here.

Line-width variations can produce velocity errors of up to a few hundred m/s when the velocity is calculated from a single rational function of the data (α-only method). The error is reduced to a few m/s by using two rational functions (α, β method). The more accurate computation requires an extra image buffer and entails doing 2.2 times as many operations.

A line-asymmetry will affect the measured velocity because the line-bisector is sampled at different depths across the solar disk. This happens because the average velocity is a function of disk position, and the data tend to sample more of the line-wings for large Doppler shifts.

Data taken at La Palma in 1988 show that the averaging of subresolution velocity elements produces a "noise" level of $\sim \pm 20$ m/s. Hence, it seems reasonable to set this as an upper limit for systematic errors.

The statistical error for a four point measurement is $\sim \pm 30$ m/s with a CCD well-depth of 2×10^5 photons. The error becomes significantly larger at $v \gtrsim 3500$ m/s for the α, β method. This can be rectified by use of a larger calibration table. The errors for 2 pass (8 point) and 4 pass (16 point) measurements are 21 m/s and 15 m/s, respectively.

In order to minimize the statistical error, sidelobes should be kept to a minimum. Hence the optimum Lyot filter-profile would have a flat peak with wings just large enough to ensure integration of equal amounts of continuum at each wavelength setting.

This recommendation for the Lyot filter width has been used in the design of the MDI instrument. The choice of velocity calculation method is still pending further study. It is not yet known whether line-width or line-asymmetry variations will contribute more to measurement errors. Only if line-asymmetry variations are small can the α, β method used.

2.3 Magnetograms

2.3.1 Inverse Zeeman Effect

Spectral lines of atoms in a magnetic field are split by the Zeeman effect. For a field component $H_{||}$ pointing toward the observer, an emission line of wavelength λ_0 is split into two components (σ components) with opposite circular polarizations. The left and right circular polarizations (LCP and RCP) are displaced from λ_0 by $-\Delta_\lambda$ and $+\Delta_\lambda$, respectively.

$$\Delta_\lambda = \frac{e H_{||}}{4\pi m_e c^2} {\lambda_0}^2 (g'M' - g''M'') \tag{2.17}$$

where g' and g'' are the Landé factors, and M' and M'' are the magnetic quantum numbers for the initial and final states (Bray & Loughhead 1964). The magnetic quantum numbers are subject to the selection rule $M'' - M' = \pm 1$. For the Fe I (6302.508 Å) line,

$$\frac{\Delta_\lambda}{H_{||}} = 47.4 \text{ mÅ/kgauss}. \tag{2.18}$$

For absorption lines, the LCP and RCP components will be preferentially absorbed at $\lambda_0 - \Delta_\lambda$ and $\lambda_0 + \Delta_\lambda$, respectively. This is termed the inverse Zeeman effect.

2.3.2 Longitudinal Field Measurement

From figure 2.16 we can write down the measured LCP and RCP intensities.

$$I_L = I_0 + \left|\frac{\partial I}{\partial \lambda}\right| \Delta_\lambda \tag{2.19}$$

$$I_R = I_0 - \left|\frac{\partial I}{\partial \lambda}\right| \Delta_\lambda \tag{2.20}$$

where $\frac{\partial I}{\partial \lambda}$ is assumed to be constant over the range $\lambda_w \pm \Delta_\lambda$.

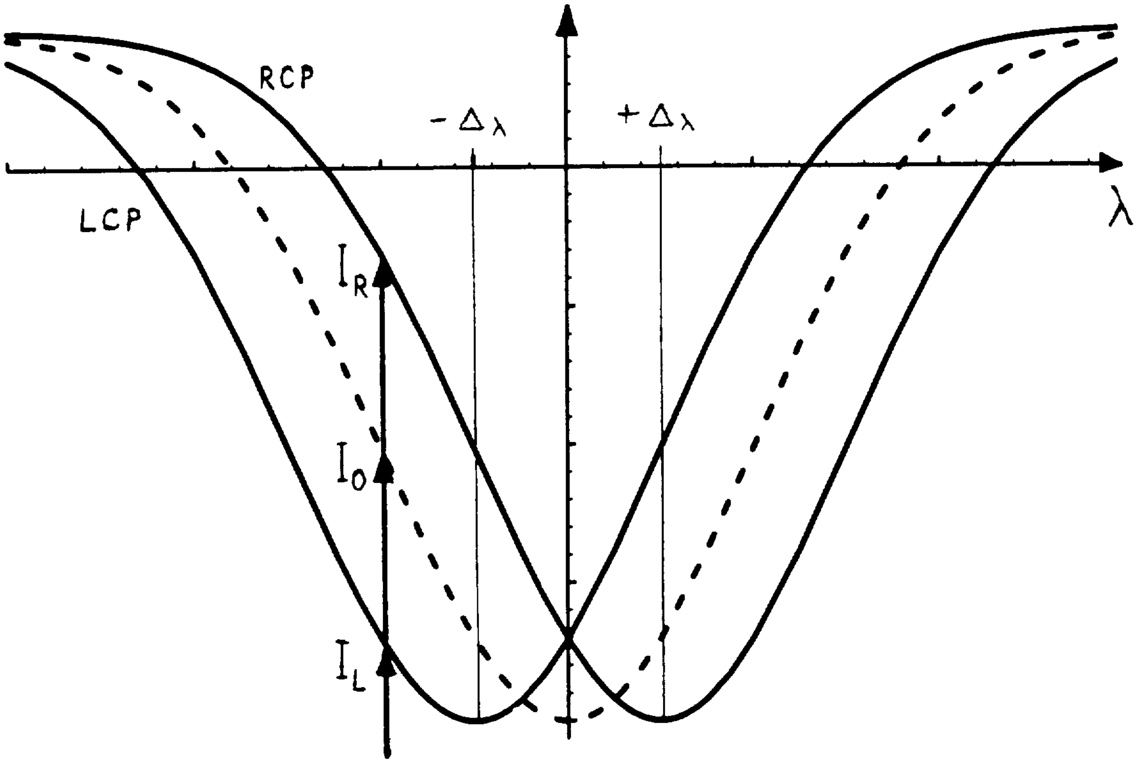

Figure 2.16: Measurement of Zeeman splitting

We can now define the magnetogram signal $\mathcal{M}$,

$$\mathcal{M} = \frac{I_L - I_R}{I_L + I_R} = \frac{1}{I_0}\left|\frac{\partial I}{\partial \lambda}\right| \Delta_\lambda \tag{2.21}$$

Combining this with equation 2.18, we have,

$$H_{||} = c\mathcal{M} \tag{2.22}$$

where the constant of proportionality c depends on the profile of the absorption line and of the filter through which the intensities are measured. The constant is independent of continuum intensity. For the filter parameters in table 4.1,

$$c \approx 10^4 \text{ gauss.} \tag{2.23}$$

2.4 Transform Methods

The goal of the data analysis is to measure the dispersion relation and amplitude of waves. The natural method for plane wave decomposition in a linear medium is the Fourier transform. Consider a monochromatic plane wave $\hat{p}$ with wave vector $\vec{k}_0 = (k_{0x}, k_{0y})$ and frequency ω_0:

$$\hat{p}(\vec{x}, t) = \cos(\vec{k}_0 \cdot \vec{x} - \omega_0 t) \tag{2.24}$$

The Fourier transform of $\hat{p}$ is defined as,

$$\mathcal{F}^3\{\hat{p}\} = \int_{-\infty}^{\infty} \int_{-\infty}^{\infty} \int_{-\infty}^{\infty} \cos(\vec{k}_0 \cdot \vec{x} - \omega_0 t) e^{-i(\vec{k}\cdot\vec{x}+\omega t)} d^2x\, dt \tag{2.25}$$

Evaluating the integral,

$$\mathcal{F}^3\{\hat{p}\} = \frac{1}{2}\delta^2(\vec{k} - \vec{k}_0)\,\delta(\omega - \omega_0) + \frac{1}{2}\delta^2(\vec{k} + \vec{k}_0)\,\delta(\omega + \omega_0) \tag{2.26}$$

The two delta functions, lying opposite one-another in $(\vec{k}, \omega)$ space, illustrate a general property of Fourier transforms. For real valued functions, the (complex) Fourier transform will have a factor of 2 redundancy in information. In fact, we only need to look at a half-space (containing the origin) to obtain all the information about the original function. It is conceptually easiest to eliminate the negative frequency half-space, and consider only:

$$-\infty < k_x < \infty, \qquad -\infty < k_y < \infty, \qquad 0 \leq \omega < \infty$$

It is important to account for relative motion of the observers field of view with respect to the observed medium. If the medium is moving at constant velocity $\vec{v}$ with respect to the observer, we have $\vec{x} \rightarrow \vec{x} - \vec{v}t$. This produces a measured frequency shift $\omega \rightarrow \omega + \Delta_\omega$ for the plane wave, where

$$\Delta_\omega = \vec{k} \cdot \vec{v}. \tag{2.27}$$

A final and extensively used property of Fourier transforms is the convolution theorem. It states that the Fourier transform of the convolution of two functions $f(x)$ and $g(x)$ is equal to the product of the Fourier transforms of the functions.

$$\mathcal{F}\left\{\int_{-\infty}^{\infty} f(\xi)\, g(x - \xi)\, d\xi\right\} = \mathcal{F}\{f(x)\}\; \mathcal{F}\{g(x)\} \tag{2.28}$$

2.4.1 Practical Considerations

The discrete Fourier transform, or Fourier series, can be viewed as an extreme example of a Fourier transform (Bracewell 1986). The series representation F_k is useful for discrete, evenly spaced data f_n with periodic boundaries. It is defined by,

$$F_k = \mathcal{F}\{f_n\} = \frac{1}{N}\sum_{n=1}^{N} f_n e^{-2i\pi nk/N} \tag{2.29}$$

The inverse transform is defined by,

$$f_n = \mathcal{F}^{-1}\{F_k\} = \frac{1}{N}\sum_{k=1}^{N} F_k e^{2i\pi nk/N} \tag{2.30}$$

For measurements made at an interval δ, the maximum Fourier frequency that can be represented is the Nyquist frequency.

$$f_{\mathrm{Nyq}} = \frac{1}{2\delta} \tag{2.31}$$

The discrete transform has the advantage that it can be evaluated using a very efficient algorithm, the Fast Fourier Transform (FFT) algorithm. The data from the series of Doppler and intensity images is indeed binned discretely on an evenly spaced grid in the spatial dimensions (by pixel) and temporal dimension (by image number). The condition of periodic boundaries must be enforced, however, by apodizing (see below).

There are several algorithms available for discrete Fourier and related transforms. For handling real valued data, it is more efficient (by a factor of 2) in computing time and memory usage to construct the Fourier transform from a Fast Sine-Cosine Transform. For doing convolutions to smooth and filter data, it is most efficient and conceptually simplest to use the Fast Hartley Transform. The abbreviation FFT is used generically hereafter to refer to the Sine-Cosine and Hartley transforms.

The FFT algorithms used were designed for data series containing N points, where N is even and factorable into low primes. The spatial dimensions were 512 pixels in both x and y ($N_x = N_y = 2^9$). The temporal dimension was 480 images ($N_t = 2^5 \cdot 3 \cdot 5$). This number was chosen because it entailed the largest "nice" number of filtergrams that would fit on a single data tape.

2.4.2 Apodization

To approximate periodic boundaries, the data is multiplied in each dimension by a function which tapers to zero at the edges. The exact form of the function must be chosen very carefully to avoid disturbing the Fourier spectrum. The convolution theorem tells us that multiplying the data by an apodizing function is equivalent to convolving the Fourier spectrum with the Fourier transform of the apodizing function. Therefore, the apodizing function should be constructed such that its transform has a narrow bandwidth and very small sidelobes.

Several standard apodizing functions are listed in Harris (1978). The 3-term Blackman-Harris function was chosen. Its discrete Fourier transform has a 3 dB width of 1.56 bins, and largest sidelobes of −61 dB. The windowing function for N bins is given by

$$W_n = a_0 + a_1 \cos\left(\frac{2\pi}{N}n\right) + a_2 \cos\left(\frac{4\pi}{N}n\right) \tag{2.32}$$

$$\text{for } n = -\tfrac{N}{2}, -\tfrac{N}{2}+1, \ldots, \tfrac{N}{2}-1$$

$$\begin{aligned} \text{where } a_0 &= 0.44959 \\ a_1 &= 0.49364 \\ a_2 &= 0.05677 \end{aligned}$$

When filtering data as done in chapter 7, it is not, in principle, necessary to apodize the data. For the La Palma data sets, however, the image rotates during the observations. Removal of this rotation from the images leaves the corners of the images without real information. To minimize round off errors from the corners, the data were masked before filtering. The mask used had a cosine taper (to zero) at the edges of a flat central disk:

$$W_{mn} = \begin{cases} 1 & \text{if } r_{mn} \le N - 32 \\ 0 & \text{if } r_{mn} \ge N \\ \cos\left(\frac{\pi}{32}(r_{mn} - N + 32)\right) & \text{otherwise} \end{cases} \tag{2.33}$$

$$\begin{aligned} \text{where } r_{mn} &= \sqrt{m^2 + n^2}, \\ m, n &= -\tfrac{N}{2}, \ldots, \tfrac{N}{2} - 1 \end{aligned}$$

2.4.3 Normalization

The FFT's are normalized such that the spectral power of a sine wave is equal to the square of the wave-height before apodization.

$$\sum_{k=-\frac{N}{2}}^{\frac{N}{2}-1} \left|\mathcal{F}\left\{W_n \cdot \tfrac{1}{2}\sin k_0 n\right\}\right|^2 = 1 \tag{2.34}$$

The exact normalization is a weak function of k and is different for the real and imaginary parts of the transform. However, it can be approximated by a constant.

$$|\mathcal{F}\{f_n\}|^2 = A|\mathcal{F}\{W_n f_n\}|^2 \tag{2.35}$$

$$\text{where } A = \left[\sum_{n=-\frac{N}{2}}^{\frac{N}{2}-1} |W_n|^2\right]^{-1} \tag{2.36}$$

This approximation is valid for wavelengths that are short compared to the scale of variation of the apodizing function W_n, as is the case for all wavelengths and frequencies of interest.

There is an additional wavenumber-dependent normalization factor that corrects for the attenuation of spatial frequencies by the atmosphere and optics. This correction is described in sections 3.4 and 5.4.1.

2.4.4 Statistical Error Estimates

An error estimate can be obtained for the spectral power $|F_k|^2$ by a standard propagation of error calculation. If we assume a constant error σ_f on the data f_n, we can use equation 2.29 to find the error on the power $\sigma_{|F_k|^2}$.

$$\sigma_{|F_k|^2} = \frac{\sigma_f}{\sqrt{2N}}|F_k| \tag{2.37}$$

In three dimensions, this becomes:

$$\sigma_{|F_{jk\nu}|^2} = \frac{\sigma_f}{\sqrt{8N_x N_y N_t}}|F_{jk\nu}| \tag{2.38}$$

Chapter 3

Telescope and Instrumentation

3.1 Telescope

The 50 cm Vacuum Solar Telescope at the Swedish Solar Observatory is shown schematically in figure 3.1. A photograph of the tower at Roque De Los Muchachos on the island of San Miguel De La Palma (Canary Islands, Spain) appears in figure 3.2. The telescope is a refractor with an f number of 45.

The image forming lens is a 50 cm achromatic doublet. Two flat mirrors M1 and M2 in the altazimuth turret guide the beam down an evacuated tube. The first lens of the achromat forms the vacuum window. At the bottom, the flat mirror M3 directs the beam through a vacuum window to the (Ursies) observing room. Extreme care was taken by the designers of the optics to ensure the telescope would perform at the diffraction limit (Scharmer *et al.* 1985).

3.2 Postfocus Instrumentation

3.2.1 Tunable Filter

Lyot Filter Operation

A Lyot filter is constructed from a series of simple birefringent elements. A representation of one such element is shown in figure 3.3. An incident pulse of light is polarized

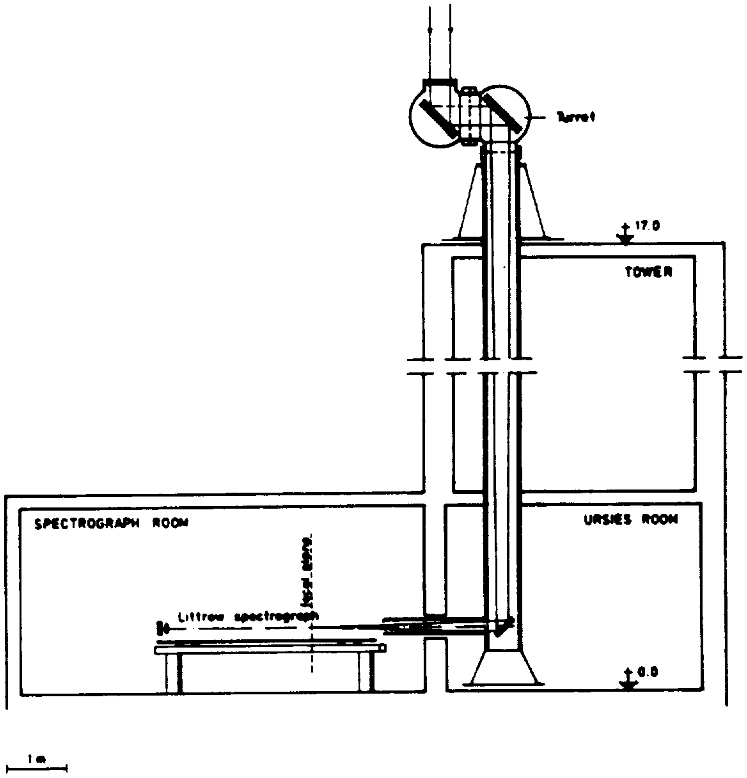

Figure 3.1: Schematic diagram of the Swedish 50 cm Vacuum Solar Telescope. From Scharmer *et al.* (1985).

at 45° to the optical axes of a birefringent crystal. Fast and slow pulses emerge from the crystal, and pass through an exit polarizer. The output of the element is, thus, a pair of identically polarized, equal amplitude pulses, with a temporal separation proportional to the crystal thickness. The spectral response of such an element is given by the Fourier transform of its impulse response. The Fourier transform of a pair of delta functions is a cosine.

A Lyot filter consists of a cascade of elements, each double the length of the previous one (see figure 3.4). The transmission of each element as a function of frequency is shown in figure 3.5. The longest element has the most closely spaced maxima. The next longest has minima that fall on every second maximum of the longest element, and so forth. The net effect is to produce a transmission profile with a mainlobe width approximately equal to that for the longest element; and a free spectral range, or distance between peaks, equal to the period for the shortest element.

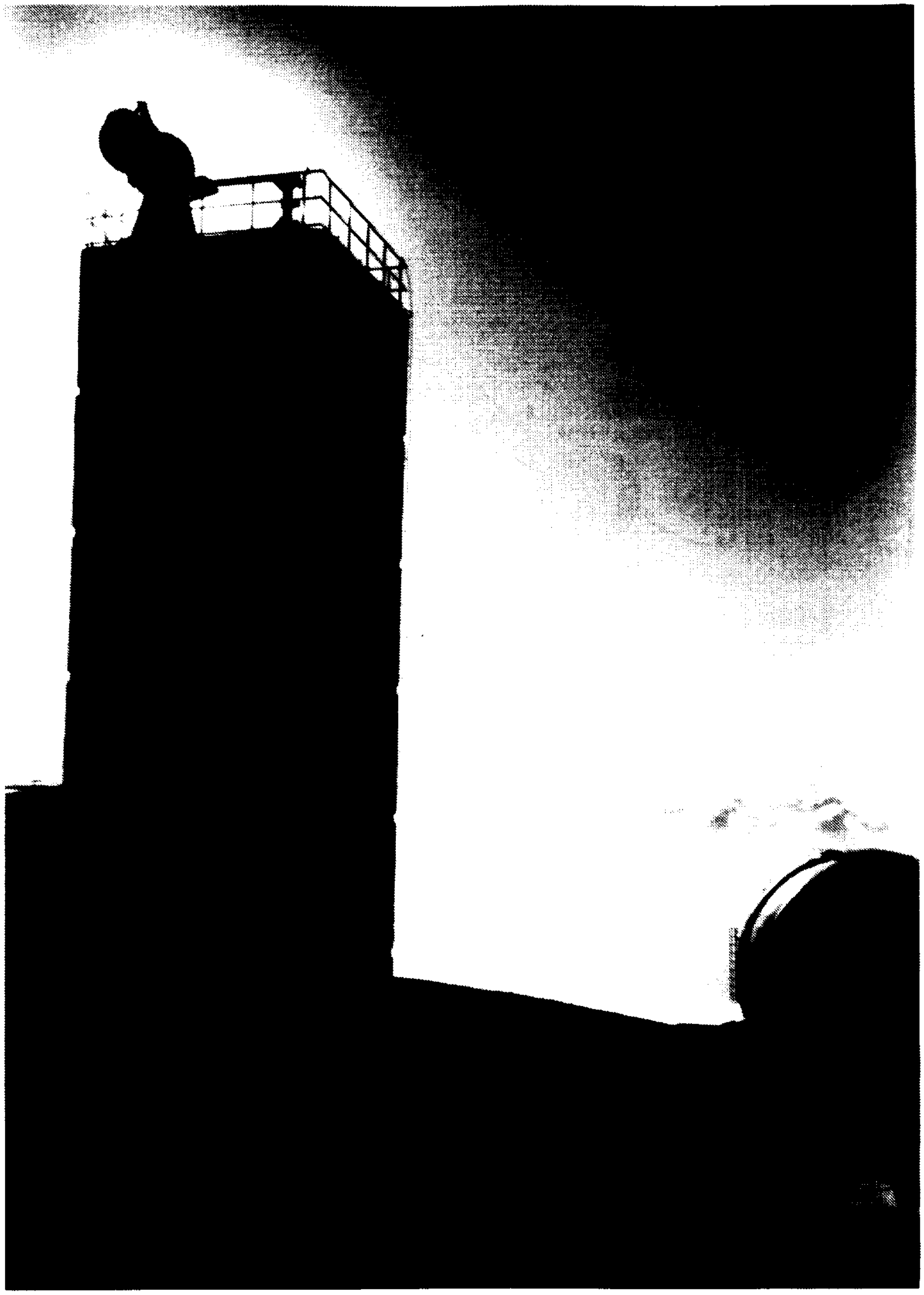

Figure 3.2: Swedish Solar Observatory, La Palma, Spain.

ORIGINAL PAGE
BLACK AND WHITE PHOTOGRAPH

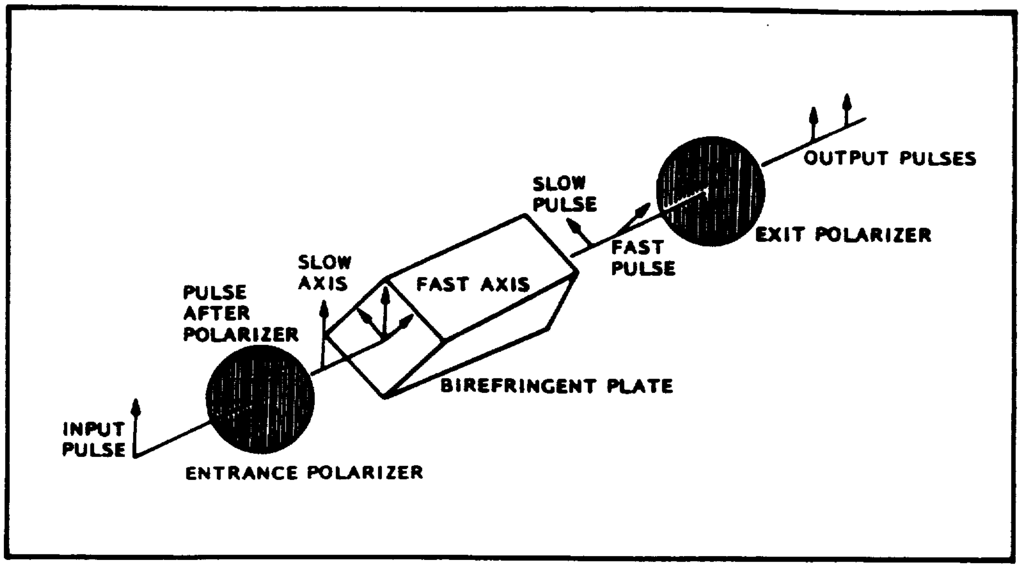
OUTPUT PULSES
SLOW PULSE
EXIT POLARIZER
FAST PULSE
SLOW AXIS
FAST AXIS
PULSE AFTER POLARIZER
BIREFRINGENT PLATE
INPUT PULSE
ENTRANCE POLARIZER

Figure 3.3: Pulse propagation through a simple element. From Title & Rosenberg (1981)

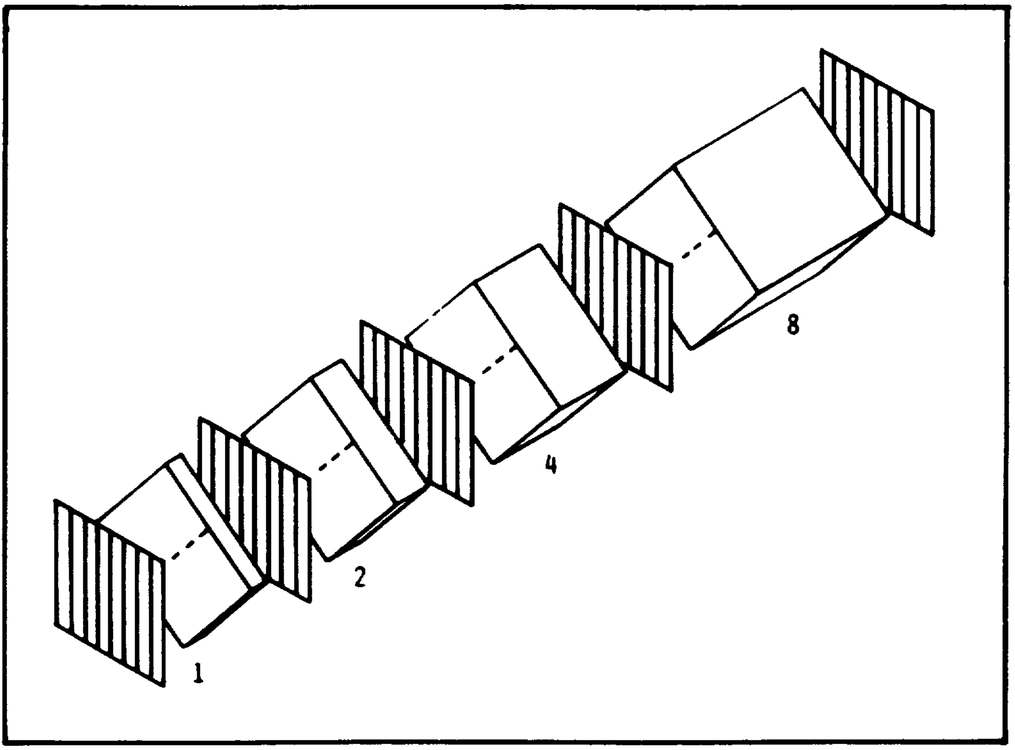

Figure 3.4: Lyot filter with four elements. From Title & Rosenberg (1981).

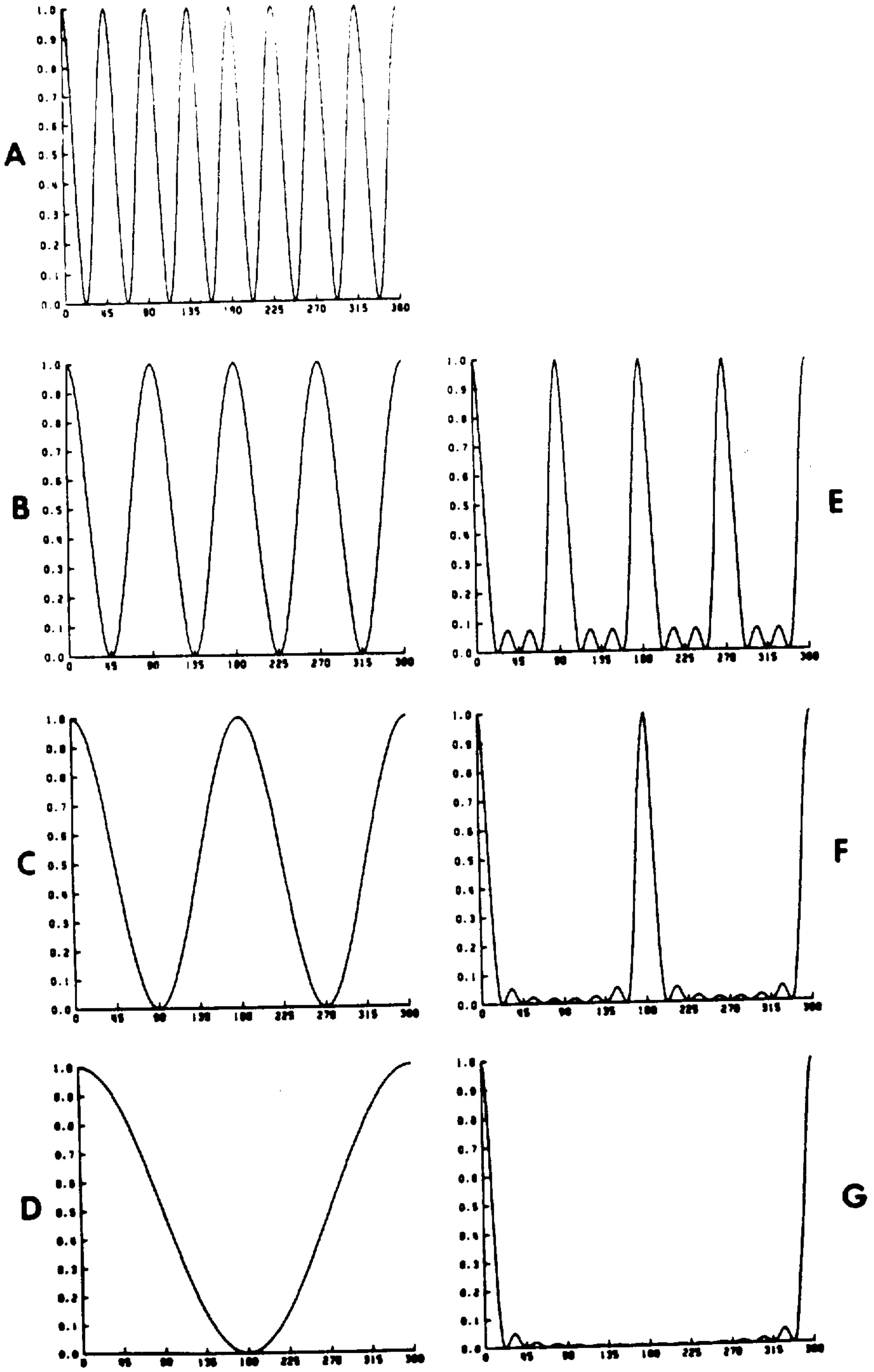

Figure 3.5: Transmission vs. frequency for the components of a Lyot filter (A, B, C, D) and the transmission through successive stages of the cascade (E, F, G). From Title & Rosenberg (1981).

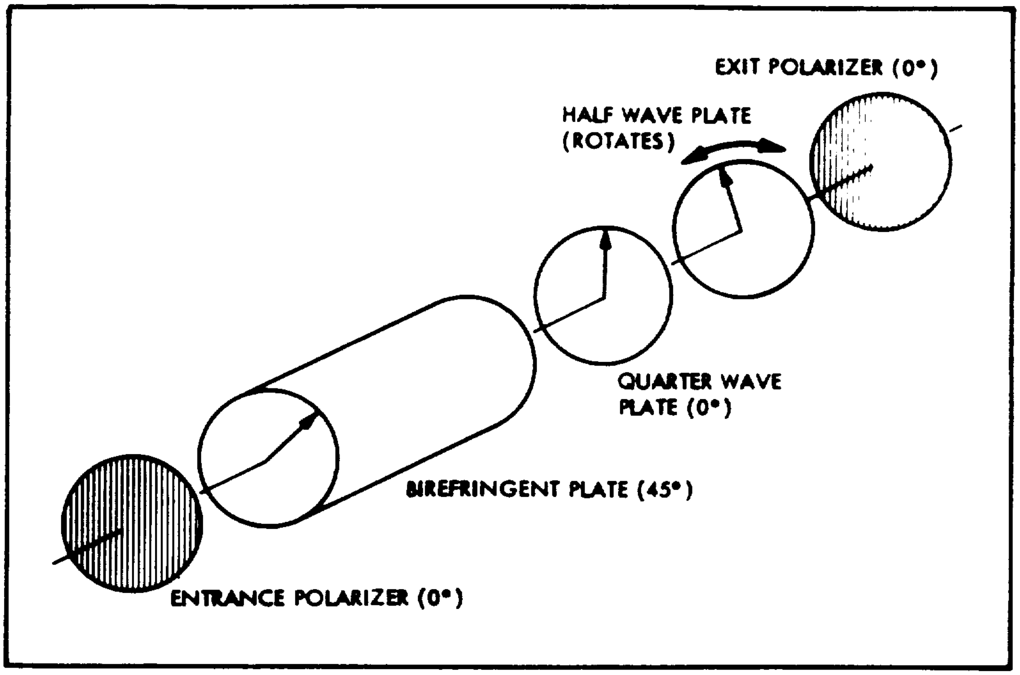

Figure 3.6: Birefringent tuning element. From Title & Rosenberg (1981).

Tuning a Birefringent Element

The bandpass of a birefringent filter can be tuned over the full free spectral range by individually tuning the component elements. The best practical method for doing this is illustrated in figure 3.6 (Title & Rosenberg 1981). As in figure 3.3, a fast and slow pulse emerge from the crystal parallel to the fast and slow axes. The delay between the pulses is inversely proportional to wavelength. Reconstituting the two polarizations gives elliptically polarized light. The axes of the ellipse are horizontal and vertical, and the ratio of the axes, the ellipticity, is a function of wavelength.

A quarter wave plate transforms the polarization from elliptical to linear, and the orientation of the resulting polarization vector is dependent on ellipticity. Finally, a rotatable half wave plate and fixed exit polarizer are used to select the linear polarization, and hence, the wavelength.

The Solar Optical Universal Polarimeter

The Solar Optical Universal Polarimeter (SOUP), developed by LPARL, employs a nine element tunable birefringent filter. It is similar in design to a Lyot filter, but each birefringent element contains a partial polarizer to apodize its transfer function. The result is a filter with smaller sidelobes than a Lyot filter. The SOUP instrument was used on the Spacelab 2 shuttle flight, and the filter has become the evaluation model for the *Orbiting Solar Laboratory — Coordinated Instrument Package* (OSL-CIP). Software-selectable blocking filters, each 6–8 Å wide, are centered on solar absorption lines. Waveplates can also be selected to measure left and right circular polarizations as well as linear polarizations spaced every 45°.

At a wavelength of 5896 Å, the free spectral range of the tunable filter is 14 Å, and the *fwhm* of the passband is 62 mÅ. A "wide mode" is also available by rotating a half wave plate within the longest element. This effectively shortens the element by a factor of 3, and increases the bandwidth to 103 mÅ. The stepping motors that rotate the tuning half wave plates permit tuning in 3.14 mÅ steps. Tuning is repeatable to within half a step.

Temperature gradients and imperfections in the filter components produce small, but measurable, variations in filter characteristics over the field of view. The center of the passband varies by up to 10 mÅ and the *fwhm*, by up to 5 mÅ over the field of view. In addition, the total amount of light transmitted (integrated over wavelength) is modulated as the filter is tuned. (See figure 3.8.) This modulation accounts for most of the error in the velocity and intensity measurements.

3.2.2 CCD Camera

The CCD (charge coupled device) camera uses a Texas Instruments 1024 × 1024 pixel, virtual phase detector. It is also an evaluation model for OSL-CIP. Subareas of the full detector can be read out to reduce the time required to write data to tape. In addition, 2 × 2 groups of pixels can be summed to decrease exposure time by a factor of 4. This 2 × 2 summing mode was used for the majority of observations listed in chapter 4.

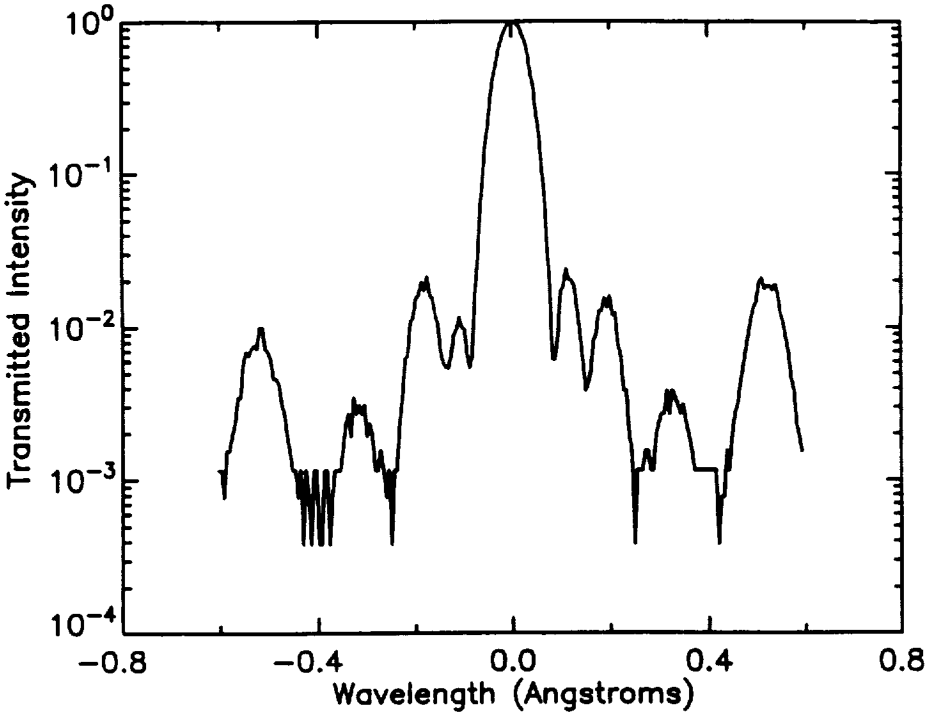

Figure 3.7: Transmission profile of the SOUP tunable filter vs. wavelength. Transmission was measured using a spectrometer, with the filter tuned to 6328 Å.

The detector geometry consists of a rectangular grid of pixels. Each pixel is efficient at collecting light up to the boundary with its adjacent pixels. Thus, the full area of the CCD array is sensitive to light.

The charge accumulated on a pixel is proportional to the integrated light falling on that pixel. The signal also integrates a current present in the absence of light, the "dark current." The dark current depends on device temperature. To keep this effect constant, and to a minimum, the CCD is kept in a vessel at low pressure, and is cooled thermoelectrically to −20° C.

3.2.3 Image Stabilization System

Compensation is made for small image displacements, caused by seeing and inaccurate telescope tracking, by an active tilt mirror in the beam path. The mirror is moved in accordance with signals from a sunspot tracker which senses image motion. The active mirror is mounted on three piezoelectric actuators which can tilt the mirror on

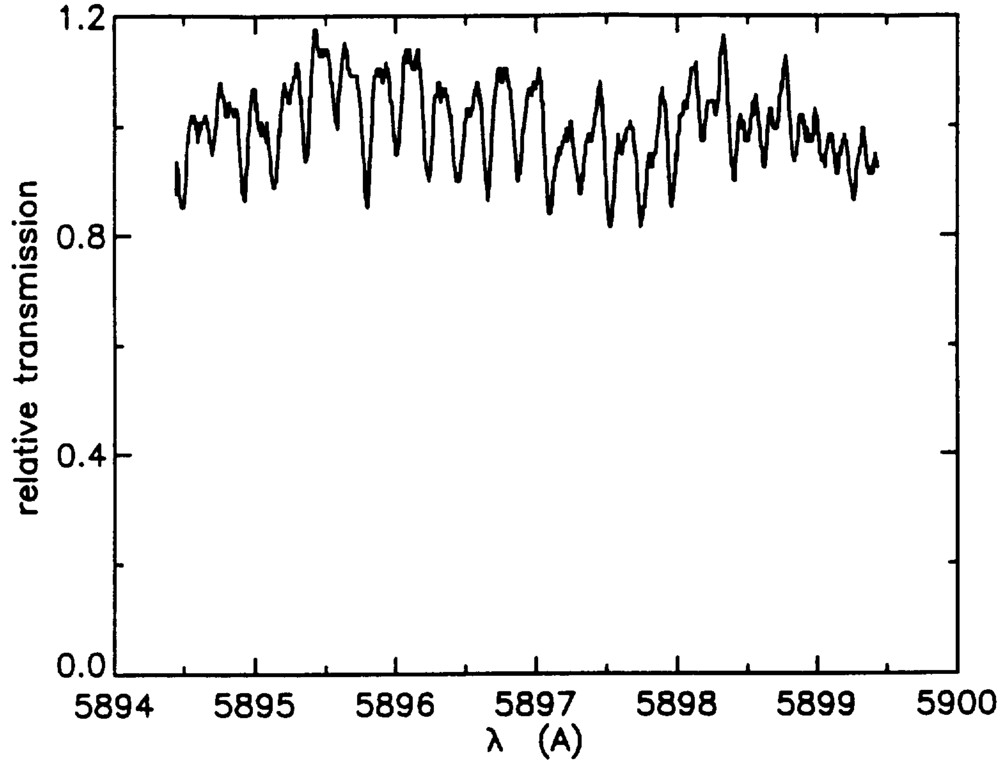

Figure 3.8: Relative transmission of the SOUP tunable filter vs. tuned wavelength. Transmission was measured using a continuum illumination source.

two axes. The system has a bandwidth of 65 Hz.

The spot tracker is an array of four photodiodes (a quad-cell). A sunspot image centered on the quad-cell will produce equal signals from each diode. If the image moves toward one of the four quadrants, however, that quadrant will experience less illumination and produce a smaller signal. The differences of signals from the four quadrants are used to determine compensatory signals for the active mirror. The integrated compensatory signals are used as a feedback to the telescope tracking system.

3.3 Optical Layout

The optical bench was set up in the Ursies room as shown in the photograph in figure 3.9. The schematic layout of components is shown in figure 3.10. The beam from the telescope strikes the active mirror, and is deflected through a field stop slightly larger than the active area of the CCD. The heat stop, used to filter out infrared wavelengths, was removed from the light path because it produced fringing patterns.

Wavelengths of 5000–7000 Å are reflected by the dichroic beam splitter to the tunable filter path. Infrared wavelengths are not reflected. Other wavelengths are reimaged through the Ca II K-line filter and the 4308 Å bandpass filter to the K-line and "white light" cameras, respectively. The white light images were used to monitor the seeing conditions and the focus in real-time. The K-line camera was not used for these observations.

After reflection from the dichroic beam splitter, the beam is collimated by a lens on a motor driven stage. The magnification of the system is chosen by substituting lenses of different focal length. The stage is moved automatically to compensate for the chromatic dispersion of the telescope, and the whole assembly, moved manually to adjust the focus. The beam passes through an aperture stop and is reimaged through a set of selectable waveplates and blocking filters, and the tunable filter. For solar observations, the beam passes through a sector shutter to the CCD camera. To check the position of a spectral line, the flip mirror was inserted into the beam to deflect it to the photometer.

Part of the beam is diverted, before the polarizer wheel, to the spot tracker. There is a neutral density filter and adjustable zoom lens system in this path to optimize the intensity and magnification of the image for the spot tracker.

The motor driven stage, polarizer wheel, blocking filter wheel, and tunable filter were controlled by a (PC compatible) COMPAQ computer. The shutter and CCD camera were controlled by a VAX Station 3200. The system was free-running, with no timebase to control the data acquisition. The timing of the images, therefore, varied as shown in figure 3.11. The time mark given to each image came from a crystal controlled clock, and is accurate to ~ 1 ms.

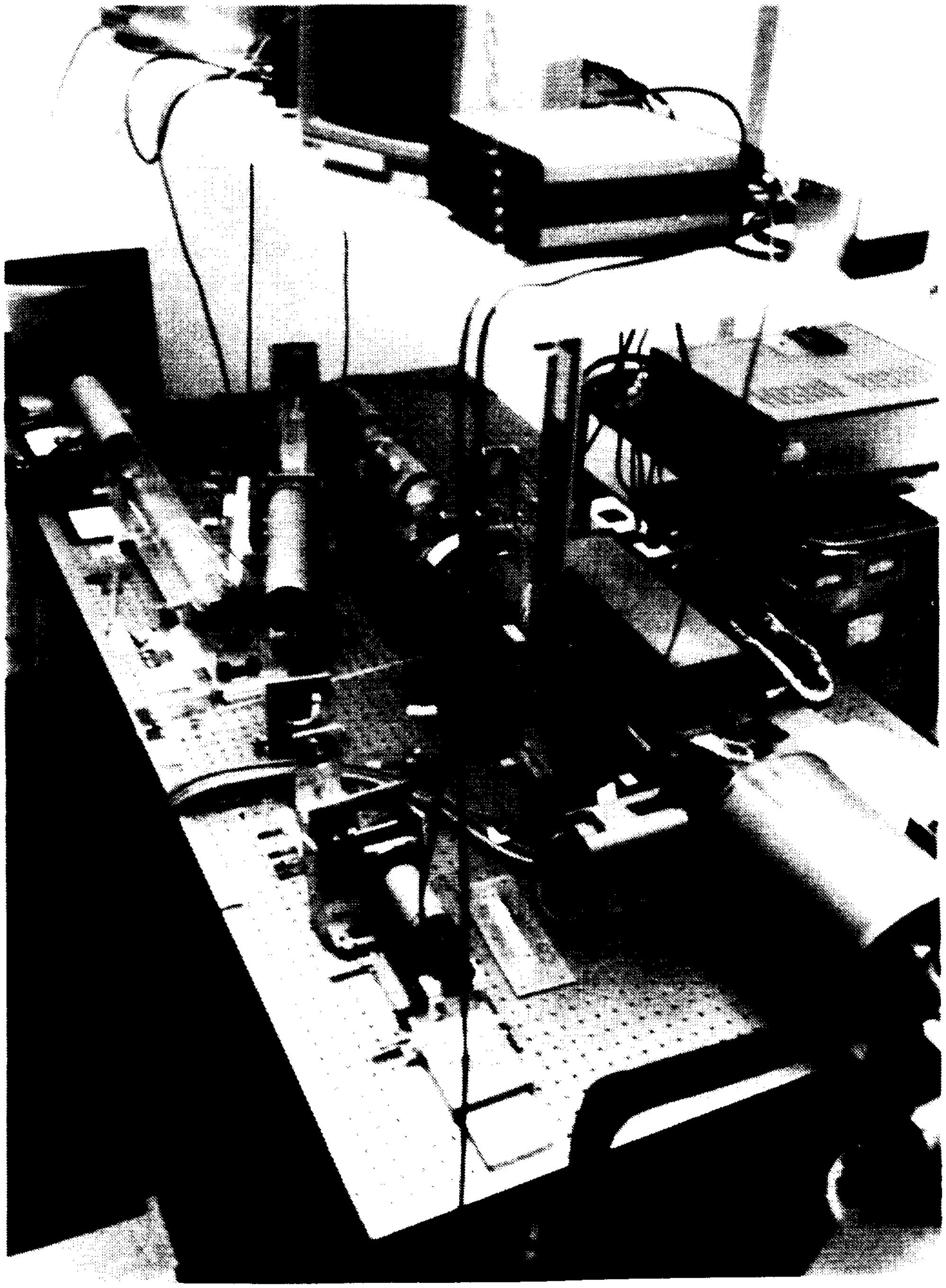

Figure 3.9: Optical bench setup.

ORIGINAL PAGE
BLACK AND WHITE PHOTOGRAPH

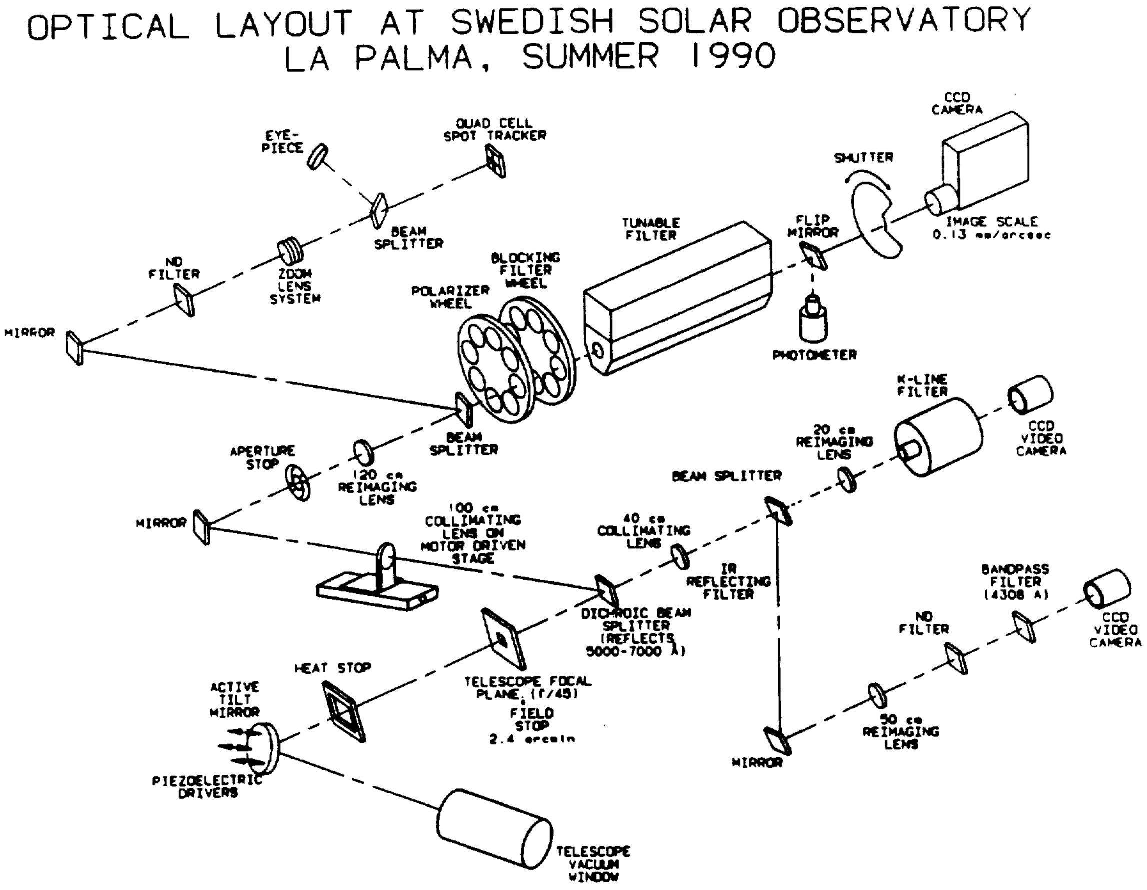

OPTICAL LAYOUT AT SWEDISH SOLAR OBSERVATORY
LA PALMA, SUMMER 1990

CCD CAMERA
EYE-PIECE
QUAD CELL SPOT TRACKER
SHUTTER
BEAM SPLITTER
TUNABLE FILTER
FLIP MIRROR
IMAGE SCALE 0.13 mm/arcsec
ND FILTER
ZOOM LENS SYSTEM
BLOCKING FILTER WHEEL
POLARIZER WHEEL
MIRROR
PHOTOMETER
K-LINE FILTER
CCD VIDEO CAMERA
20 cm REIMAGING LENS
BEAM SPLITTER
APERTURE STOP
120 cm REIMAGING LENS
BEAM SPLITTER
MIRROR
100 cm COLLIMATING LENS ON MOTOR DRIVEN STAGE
40 cm COLLIMATING LENS
IR REFLECTING FILTER
BANDPASS FILTER (4308 Å)
CCD VIDEO CAMERA
DICHROIC BEAM SPLITTER (REFLECTS 5000-7000 Å)
ND FILTER
HEAT STOP
ACTIVE TILT MIRROR
TELESCOPE FOCAL PLANE (f/45) & FIELD STOP 2.4 arcmin
50 cm REIMAGING LENS
MIRROR
PIEZOELECTRIC DRIVERS
TELESCOPE VACUUM WINDOW

Figure 3.10:

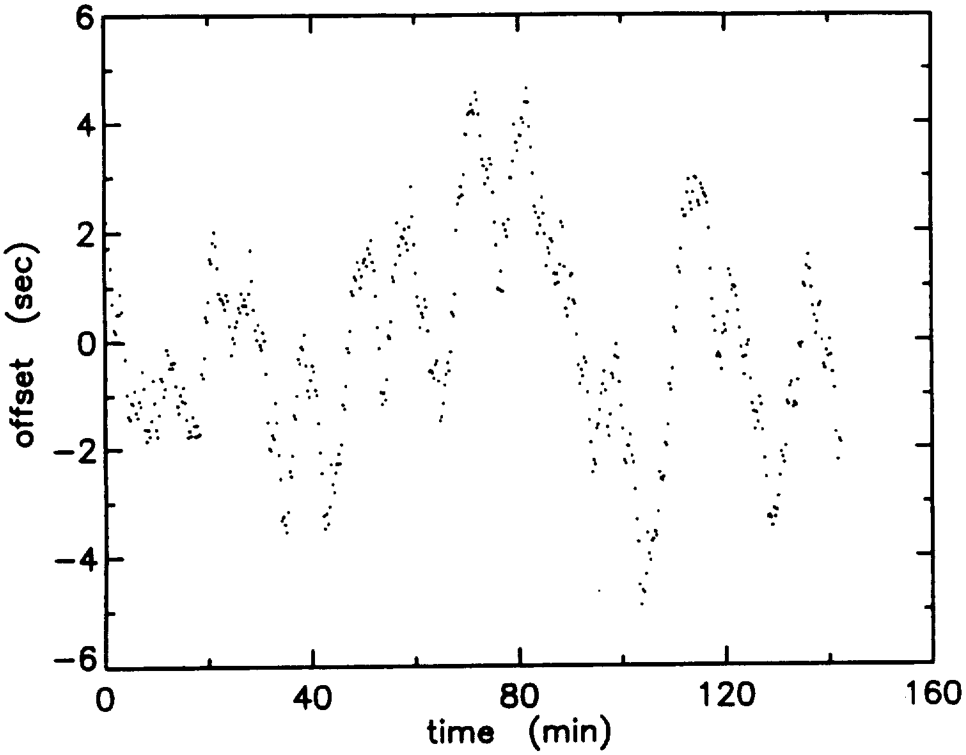

Figure 3.11: Timing offset for images vs. time from start of run. The offset is the difference between the image time mark and a straight line fit to the time marks.

3.4 Modulation Transfer Function of the System

The modulation transfer function (MTF) of an optical system describes the effect of aberrations and diffraction on an image formed through the system. If $I_g(\vec{x})$ is the image intensity distribution expected from aberration-free geometrical optics, then the real image intensity distribution $I_r(\vec{x})$ is given by,

$$I_r(\vec{x}) = \mathcal{F}^{-1}\left\{\mathrm{MTF}(\vec{k}) \cdot \mathcal{F}\{I_g(\vec{x})\}\right\} \tag{3.1}$$

The attenuation of the spectral power $|\mathcal{F}\{I_g\}|^2$ is given by the square of the MTF functions.

The components which contributed significantly to the total MTF are the entrance pupil, the detector pixel shape, and the earth's atmosphere. The total MTF is the product of the MTF's of these individual components. The atmospheric MTF will be treated in section 5.4.1.

3.4.1 Entrance Pupil

The entrance pupil is defined by the diameter d (48 cm) of the heat shield diaphragm in front of the objective. The MTF of the pupil is given by the autocorrelation of the pupil function (a disk). For wavenumbers, $0 \leq k \leq k_{\mathrm{Nyq}}$,

$$\mathrm{MTF}(k) = \frac{2}{\pi}\left[\cos^{-1}\kappa - \kappa\sqrt{1-\kappa^2}\right] \tag{3.2}$$

$$\text{where } \kappa = \frac{\lambda}{2d}\left(\frac{\#\text{ pixels}}{\text{field of view}}\right)\frac{k}{k_{\mathrm{Nyq}}}$$

3.4.2 CCD Camera

The effect of summing light over the area of a CCD pixel is equivalent to convolving the image distribution with the pixel shape, and sampling the new distribution at points centered on each pixel. Thus, the MTF of the detector is the modulus of the Fourier transform of the pixel function (a square).

$$\mathrm{MTF}(\vec{k}) = \operatorname{sinc}\kappa_x \operatorname{sinc}\kappa_y \tag{3.3}$$

$$\text{where } \vec{\kappa} = \frac{1}{2}\frac{\vec{k}}{k_{\mathrm{Nyq}}}$$

$$\text{and } \operatorname{sinc} x \equiv \frac{\sin \pi x}{\pi x}$$

This can be approximated by a cylindrically symmetric function with no more than a 2% error.

$$\mathrm{MTF}(k) = \operatorname{sinc}\kappa \tag{3.4}$$

The square of the MTF functions are plotted in figure 3.12 for the entrance pupil and CCD detector.

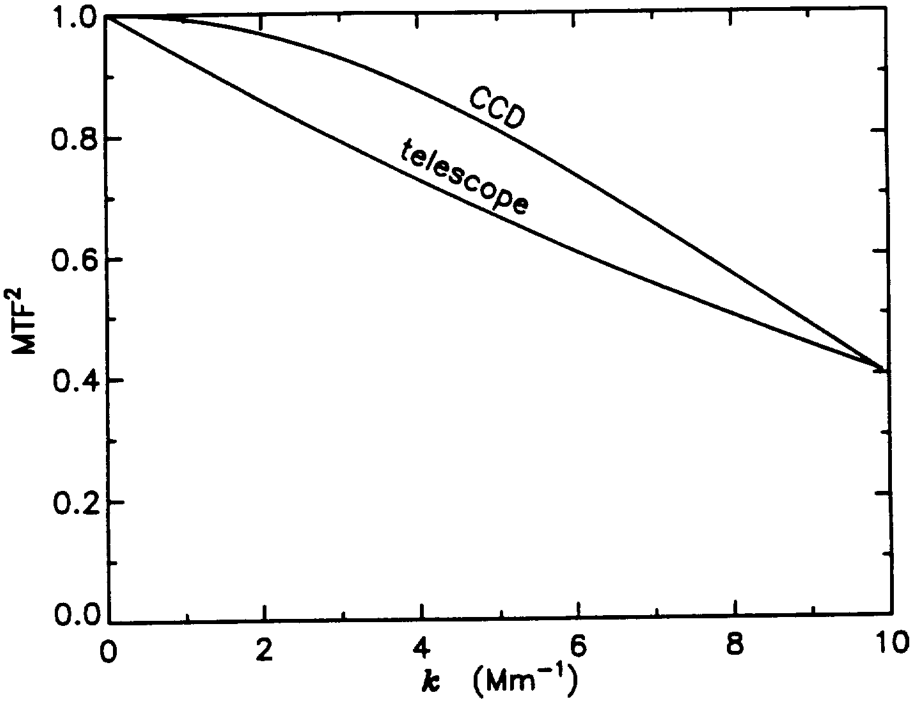

Figure 3.12: Squared MTF of telescope and CCD detector

Chapter 4

Observations

The original topic of this dissertation was "sunspot seismology," that is, the study waves propagating into and out of sunspots. That topic was set aside when waves were discovered at substantially higher wavenumber and frequency than had previously been observed. The new topic of analysis became the characterization of properties of these waves. Many of the observing runs are, therefore, extraneous to the analysis described here. They have been included in the list of data in this chapter, but no calibration or reduction has been performed on them.

4.1 Observing Procedure

The observing runs consist of a repeating sequence of filtergrams with a temporal spacing of about 3.5 s between filtergrams. The wavelength, filter width, polarization, and relative exposure time for each filtergram in the sequence is defined in the sequence file residing on the COMPAQ computer that runs the filter.

Calibration data was taken before and after observing runs. The order of calibration and observations was as follows:

1. Dark Currents: 4 measurements of dark currents for each exposure setting. Done at the beginning and end of each day.

2. Line Centering: Definition of the nominal line center from which wavelength offsets are measured. The photometer detector was used to integrate light over the field of view with the target region centered in the field.
3. Slide Projector Flats: 4 repetitions of flat field measurements using slide projector source.
4. Observing Run: One or more tapes-worth of observations of target region.
5. Solar Flats: 4 repetitions of flat field measurements using defocused sunlight source.
6. Slide Projector Flats: Repeat of step 3.

The line centering step is performed by scanning the filter through a range of wavelengths (from short to long), and plotting intensity versus wavelength. This step was not performed correctly due to a design flaw in the photometer interface with the COMPAQ computer. The computer did not wait for the full signal integration time before reading the light intensity. In the resulting line profile scan, the intensity points lagged behind the wavelength points. This caused the line to appear shifted to longer wavelength. The line was, therefore, "centered" to an erroneously short wavelength. This offset of -40 mÅ for the Na D_1 line was discovered by making a line scan using the CCD camera instead of the photometer (see figure 4.1).

4.2 Calibration Method

The purpose of calibration is to produce images with a signal to illumination ratio that is independent of both the pixel location and the wavelength setting of the tunable filter. The procedure described here is more complicated than the standard one used by the Lockheed group. This is necessary to provide an accurate calibration for dopplergrams. The flat fielding procedure calibrates the whole system, optics and detector together.

The CCD is a very linear device, provided the light intensity stays below saturation levels. Response of a pixel can be characterized by a gain and an offset. The offset

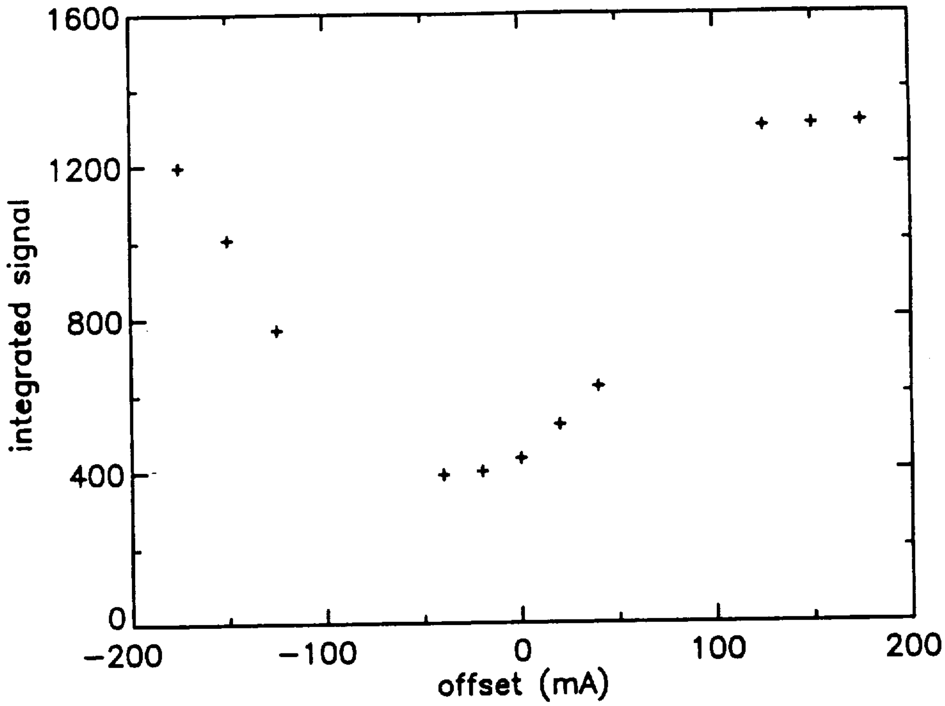

Figure 4.1: Line scan of Na D_1 Line using the CCD camera. Signal, integrated over the field of view, vs. wavelength offset.

is determined by the amount of charge that accumulates on the CCD in the absence of illumination (the "dark current"). It must be measured for each exposure time. Each pixel has a characteristic gain and dark current. The tunable filter is also responsible for some variation of the signal strength as a function of wavelength λ and spatial position $\vec{x}$. The net response of the system is to produce filtergrams $F_i(\vec{x})$ at wavelengths λ_i, given a source intensity distribution $\hat{S}(\vec{x}, \lambda)$.

$$F_i(\vec{x}) = \int \hat{S}(\vec{x}, \lambda)\, A_i(\vec{x}, \lambda)\, d\lambda + D(\vec{x}) \tag{4.1}$$

where $A_i(\vec{x}, \lambda)$ is the product of filter transmission and CCD gain at filter setting λ_i, and $D(\vec{x})$ is the CCD dark current.

Because the filter bandpass is narrow compared with spectral features in the source, we can approximate:

$$\int \hat{S}(\vec{x}, \lambda)\, A_i(\vec{x}, \lambda)\, d\lambda = \hat{S}(\vec{x}, \lambda_i) \int A_i(\vec{x}, \lambda)\, d\lambda. \tag{4.2}$$

Thus

$$F_i(\vec{x}) = \hat{S}(\vec{x}, \lambda_i)\, B_i(\vec{x}) + D(\vec{x}) \tag{4.3}$$

$$\text{where } B_i(\vec{x}) = \int A_i(\vec{x},\lambda)\,d\lambda. \tag{4.4}$$

In order to determine $\hat{S}$, the quantity of interest, we must first measure B_i and D. The dark current D is easily measured by making filtergrams with no illumination source. For $\hat{S} = 0$, we have $D = F_i$.

If we had an illumination source that were both flat in spectrum and flat across the field of view, we could measure B_i directly. The sources available, however, were:

1. Defocused Sunlight $\hat{S}_S(\lambda)$: Flat across field, but not spectrally flat.
2. Slide Projector Lamp $\hat{S}_L(\vec{x})$: Flat in spectrum, but not flat across field.

The technique is to make one filtergram F_c^S at wavelength λ_c in the continuum (away from the absorption line), using defocused sunlight. And, to make filtergrams F_c^L at λ_c and F_i^L at λ_i using the slide projector lamp. This gives us the following three measurements:

$$F_c^S(\vec{x}) = \hat{S}_S(\lambda_c)\,B_c(\vec{x}) + D_S(\vec{x}) \tag{4.5}$$

$$F_c^L(\vec{x}) = \hat{S}_L(\vec{x})\,B_c(\vec{x}) + D_L(\vec{x}) \tag{4.6}$$

$$F_i^L(\vec{x}) = \hat{S}_L(\vec{x})\,B_i(\vec{x}) + D_L(\vec{x}) \tag{4.7}$$

Given the dark currents D_L and D_S, we can solve for the gain correction $\mathcal{G}_i$ at λ_i defined as $\mathcal{G}_i(\vec{x}) = B_i(\vec{x})^{-1}$.

$$\mathcal{G}_i(\vec{x}) = \frac{[F_c^L - D_L]}{[F_i^L - D_L][F_c^S - D_S]} \tag{4.8}$$

There is some arbitrary overall normalization which depends on $\hat{S}_S(\lambda_c)$. In practice the spatial average of $\mathcal{G}_i$ at the λ_c filter position was defined as unity, and the other gain corrections, normalized accordingly.

With the gain corrections and dark currents in hand, we can determine arbitrary source distributions from filtergrams.

$$\hat{S}(\vec{x},\lambda_i) = \mathcal{G}_i(\vec{x})\,[F_i(\vec{x}) - D(\vec{x})] \tag{4.9}$$

4.3 Solar Observations

The sequence of filtergrams for the sunspot seismology study was named SEISNAFE. It was designed to determine the following quantities:

1. Doppler shift in mid-chromosphere (in sunspot umbrae).
   [H I (Balmer) α—line core]
2. Doppler shift in photosphere.
   [Na D_1—wings]
3. Doppler shift in low chromosphere.
   [Na D_1—core]
4. Doppler shift in photosphere.
   [Fe I (5576Å)]
5. Continuum intensity in green and red.
   [5575Å, 5894Å]
6. Photospheric magnetic field (line of sight component).
   [Fe I (6302Å)]

The sequence repeated every 47 s. Filter parameters appear in table 4.1. The corresponding calibration sequences were NAFEFLAT for solar flats, and SEISSP for slide projector flats. The observing runs of appreciable length are listed in table 4.2.

The sequence of filtergrams used for the high-frequency oscillation study was named NAFAST. It was designed to make dopplergrams in the low chromosphere and photophere, using filtergrams in the core and wings of Na D_1, respectively. All other measurements were eliminated to increase the repetition rate to once every 17.7 s. The sequence parameters appear in table 4.3 and the corresponding calibration sequences were NAFEFLAT for solar flats, and NAFASTSP for slide projector flats.

The NAFAST sequence was run only once on August 2, 1990 beginning 13:51 UT. The target region was an active region (AR6181) containing a small, decaying sunspot. This is shown on a full-disk magnetogram in figure 4.2. The run lasted

Table 4.1: Filter Parameters for SEISNAFE Sequence.

Line	(Å)	Offset (mÅ)	Filter Mode (width)	Polarization (0 = linear)	Purpose
H I α	6562.8	-400 0 400	wide	0	dopplergram
Na D_1	5895.9	-40 0 40	narrow	0	dopplergram
Na D_1	5895.9	-175 -125 125 175	narrow	0	dopplergram
Na D_1	5895.9	-2000	narrow	0	continuum
Fe I	5576.1	-90 -30 0 30 90	wide	0	dopplergram
Fe I	5576.1	-750	wide	0	continuum
Fe I	6302.5	-60 -60	narrow	LCP RCP	magnetogram

Table 4.2: La Palma Observing Runs using SEISNAFE Sequence.

Date (1990)	Time (UT)	Duration (min)	Seeing	FOV	Target Region
28 Jul	7:47	113	good/v.good	75″	AR6168 (medium sunspot)
	10:26	112	fair/var.	150″	AR6168
29 Jul	8:39	156	fair/var.	150″	AR6174 (medium sunspot)
	16:53	126	good/var.	150″	
30 Jul	7:50	281	variable	224″	
	13:12	293	variable	224″	
31 Jul	8:34	237	good/var.	224″	— flare in morning
	13:09	347	variable	224″	
1 Aug	8:08	256	good/var.	224″	AR6181 (small sunspot)
1 Aug	13:35	310	good/fair	224″	AR6179 (big sunspot)
2 Aug	7:46	151	good/fair	150″	— overexp'd for umbral osc.
2 Aug	10:52	101	fair/var.	224″	AR6186 (big sunspot on limb)
5 Aug	9:20	190	fair/var.	224″	quiet region near AR6192

Table 4.3: Filter Parameters for NAFAST Sequence.

Line	(Å)	Offset (mÅ)	Filter Mode (width)	Polarization (0 = linear)	Purpose
Na D_1	5895.9	-40 0 40	narrow	0	dopplergram
Na D_1	5895.9	-175 -125 125 175	narrow	0	dopplergram
Na D_1	5895.9	-2000	narrow	0	continuum

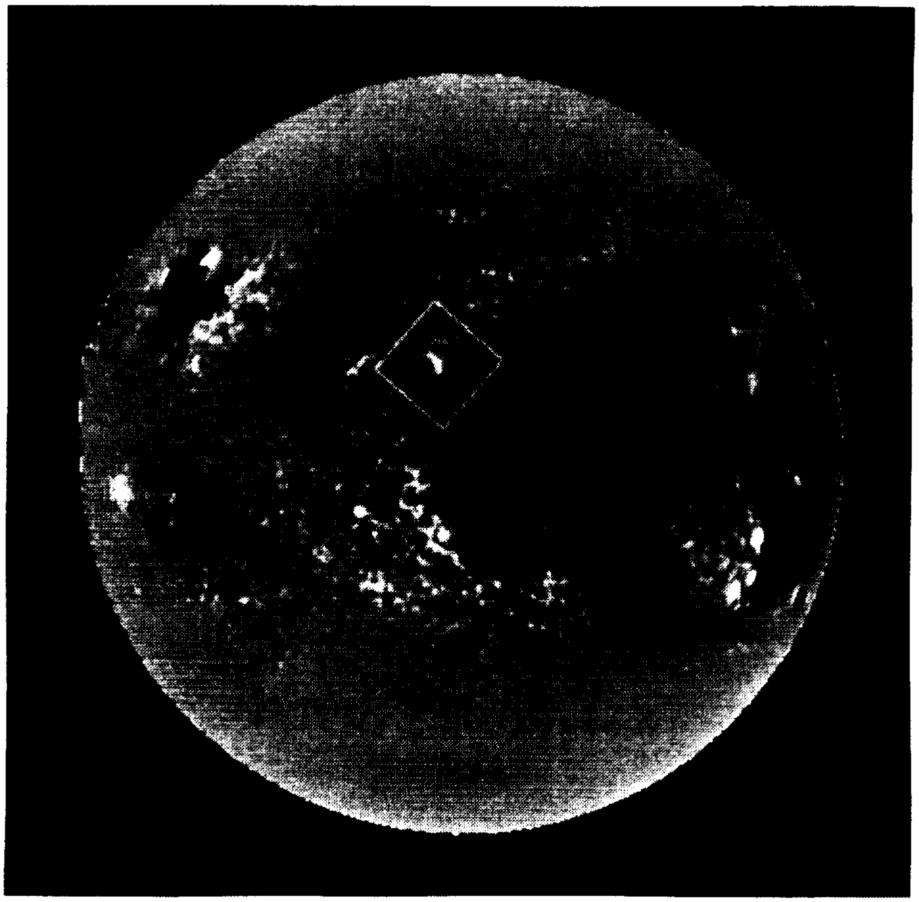

Figure 4.2: Full-disk magnetogram from the National Solar Observatory at Kitt Peak. The field of view containing AR6181 is outlined.

143 min with good/variable seeing that deteriorated in the last 30 min of the run. To obtain more information about the active region, the SEISNAFE sequence was run before and after the NAFAST runs. A continuum image is shown in figure 4.3, a high resolution magnetogram, in figure 4.4, and, an offband H α image, in figure 4.5.

ORIGINAL PAGE
BLACK AND WHITE PHOTOGRAPH

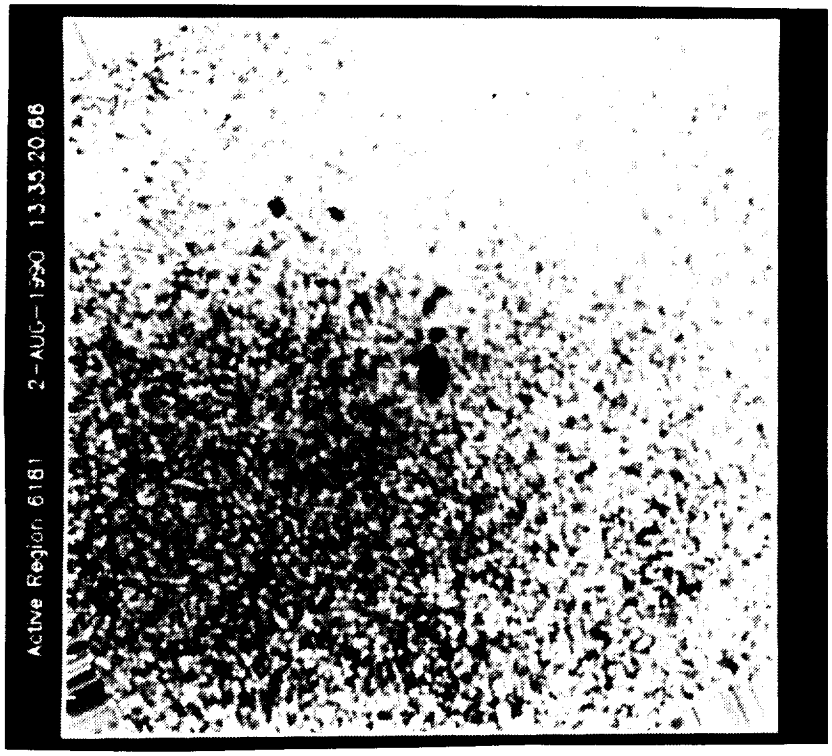
Active Region 6181
2-AUG-1990
13:35:20.66

Figure 4.3: Continuum intensity (5575Å) image of AR6181. The small tick marks are 5″.

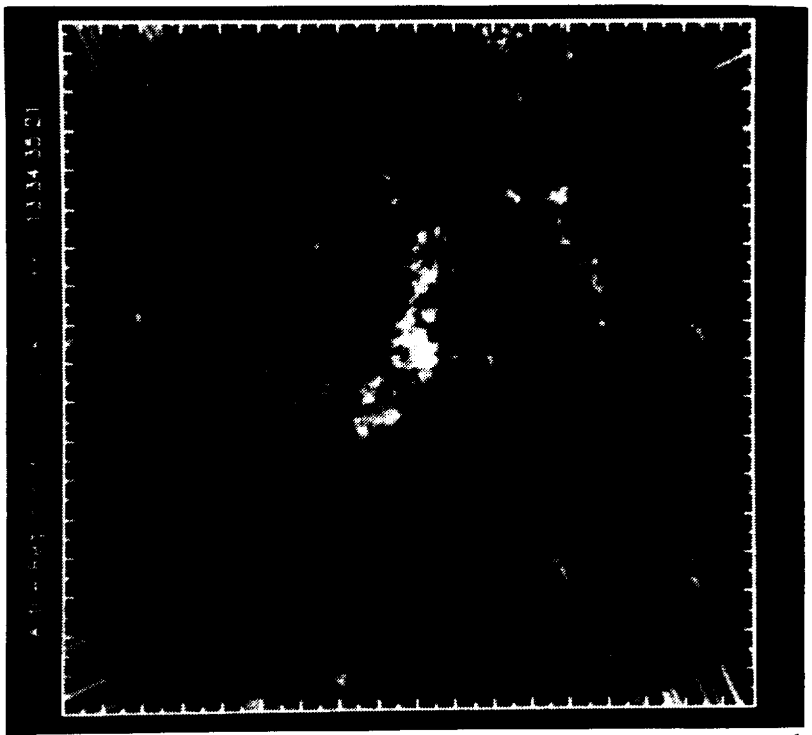

Figure 4.4: Magnetogram of AR6181. Network field is visible around the sunspot. The small tick marks are 5″.

ORIGINAL PAGE
BLACK AND WHITE PHOTOGRAPH

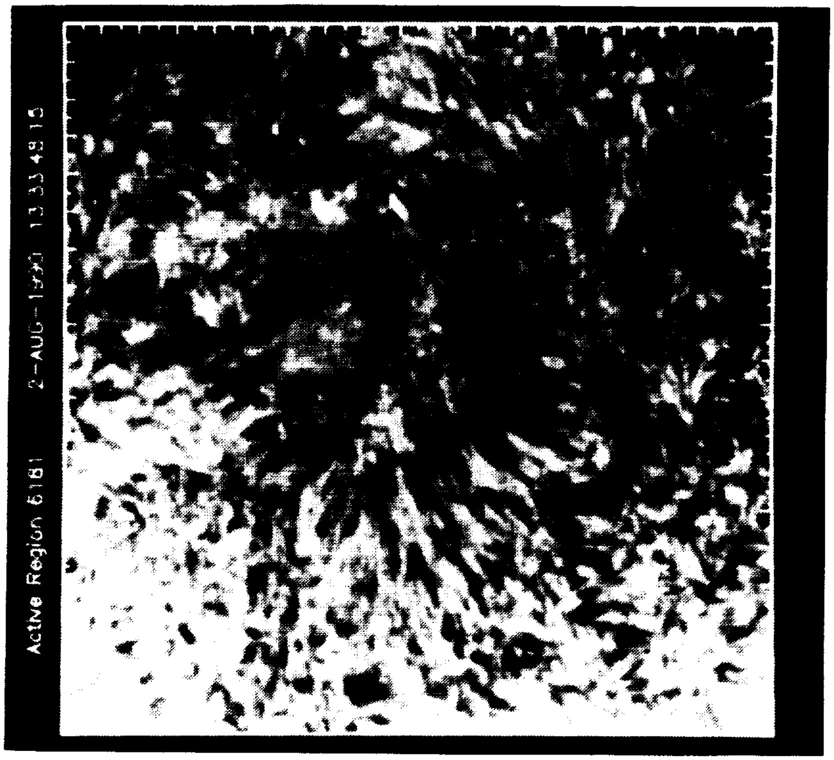
Active Region 6181 2-AUG-1990 13 33 49 15

Figure 4.5: H α image of AR6181 (400 mÅ in the blue wing). The small tick marks are 5″.

Chapter 5

Data Reduction

The raw data used for this dissertation reside on a (full) 2.2 Gigabyte Exabyte tape. In producing a power spectrum, the volume of data is reduced by a factor of $\sim 3 \times 10^4$. There is more to the reduction procedure, however, than extracting a manageable amount of information from a cumbersome data set. The quality of the data depends on careful calibration to account for instrument response, image rotation and drift caused by telescope motion, and, distortion caused by the atmosphere. The absolute spatial scale of the images must also be determined accurately. This chapter describes the details of and cross-checks for the data reduction procedures.

The reduction steps are listed below in the order they were performed:

1. Flat Fielding: Calibrate for variation in filter transmission and CCD gain, and subtract CCD dark current.
2. CCD Flaw Correction: Interpolate over nonfunctional pixels.
3. Correction for Atmospheric Blurring: Normalization of measured MTF.
4. Rigid Rotation: Compensate for image rotation caused by telescope tracking motions during observations.
5. Correction for Atmospheric "Shimmer." (Destretching)
6. Calculation of Dopplergrams and Line Center Intensity.
7. Rigid Alignment: Compensate for image drift caused by telescope tracking errors.

8. Fourier Transform of Dopplergrams and Intensities: Described in section 2.4.
9. Angular Scale Determination: Convert units from pixels to arcseconds.
10. Distance Scale Determination: Measurement of foreshortening and direction toward disk center. Described in section 6.1.1.
11. Measurement of Oscillation Properties: Described in chapters 6 and 7.

5.1 Flat Fielding

The flat fielding scheme is explained in section 4.2. We can use equation 4.9 to calibrate filtergrams, given dark currents D and gain corrections $\mathcal{G}_i$. The dark current is an average of four filtergrams made with a light stop placed in front of the filter. The gain correction is constructed using equation 4.8 as follows.

The three flat field measurements F_c^S, F_c^L, and F_i^L are each made from an average of four filtergrams. Because the filter stepping motors did not always find the correct positions, it was sometimes necessary to throw out one of the four measurements and use only three to make the average. A filtergram was thrown out if the spatial average of the central 64 × 64 pixels of the image differed by more than 5σ from the spatial averages of subareas of the other three images, where σ is defined by inefficient statistics.

$$\sigma_I = \frac{I_{\max} - I_{\min}}{N_I} \tag{5.1}$$

The gain correction is the product of $(F_c^S - D_S)^{-1}$ and $(F_c^L - D_L)/(F_i^L - D_L)$. The latter is the ratio of the transmittance in continuum to transmittance an λ_i. This ratio should be slowly varying over the field of view. The dark currents are not constant with time, however, and the very long exposure times required for slide projector flats (2–3 s) caused accumulation of large charges at some small groups of pixels. It was, thus, necessary to "deflaw" F_c^L and F_i^L (see next section), and smooth the transmittance ratio using a Gaussian point-spread function of 18 pixel *fwhm*.

The procedure described here produced (flat fielded) images with signal to illumination ratios that were constant to within about 3% across the field of view, and, more importantly, to within about 5% across the wavelength range of an absorption line. These numbers were measured from filtergrams of defocused sunlight (the flat field illumination source) at continuum wavelengths.

5.2 CCD Flaw Correction

Of the 2.5×10^5 pixels (in 2×2 summing mode), 4513 were not functional. An additional 491 pixels had exceptionally high dark currents for exposure times greater than about 500 ms. To minimize problems caused by the missing data, values were filled in at these pixel locations by linear interpolation from adjacent pixels. This procedure is termed "deflawing".

A good map of nonfunctional pixel locations was available for exposure times below 500 ms. For the longer exposure times, a map was constructed using the dark current runs. To do this, a cubic trend was fitted to each row of a filtergram. Pixels which differed from the trend by more than 7% were flagged as "bad", and their locations, entered in the map.

5.3 Image Rotation

The altitude-azimuth axes of mirrors M1 and M2 cause the solar image to rotate during the day as the telescope tracks the sun. The rotational direction and rate are functions of date and time of day, and can be calculated from geometrical considerations. Standard software exists to determine the angle of rotation and regrid the images by bicubic interpolation. This removes the apparent rotation in a sequence of images, but some data is lost from the corners of the images.

5.4 Atmospheric Distortion

Turbulence in the earth's atmosphere will modify wavefronts of light before they reach the telescope. Any plane wave passing through the atmosphere will be distorted. The resulting wavefront, however, can be approximated by a set of planar patches.

The isoplanatic angle describes the angular extent over which image distortions are correlated. For excellent seeing conditions, it can be over $100''$ (von der Lühe 1988). For poor seeing, it can be less than $1''$.

A change in angle of incidence of a planar wavefront produces an image displacement. When different parts of an image are displaced in different directions, the image appears distorted. The distortions change with the atmospheric turbulence. This can occur over a range of timescales, from 1 to 1000 ms, with most power in the 10–100 ms range.

5.4.1 MTF Normalization

The distortion of a wavefront from a given object point differs over the telescope aperture. Moreover, local displacements of up to an arcsecond cause the image to move around in times of order 10 ms. For exposures lasting tens to hundreds of milliseconds, these changing distortions will be superimposed to produce a blurred filtergram. The effect is equivalent to convolving the image with some unknown point spread function. The Fourier transform of the point spread function is called the MTF. It is assumed here that the point spread function is the same everywhere in the field of view of a given filtergram.

The atmospheric MTF can be estimated from the spatial frequency spectrum of a filtergram $S(f)$. A contour plot of spatial frequency spectra is shown in figure 5.1 for the -40 mÅ filtergram set. The sharpest filtergrams in the set are assumed to be diffraction limited (atmospheric MTF = 1). Since the structure of solar images should not change appreciably over the observing run, the spatial spectra of diffraction limited images should be a constant $S_{\max}(f)$. Any difference between the spectrum of a given filtergram and $S_{\max}$ must, therefore, be due to the atmospheric MTF.

$$S(f) = \mathrm{MTF}_{\mathrm{atm}}(f) \cdot S_{\max}(f) \tag{5.2}$$

In practice the log-spectra were compared with the mean log-spectrum $\overline{\log S}$. Log-spectra of individual filtergrams were smoothed by convolution with a cosine-bell, and the difference between $\overline{\log S}$ and the smoothed spectrum was used as a correction

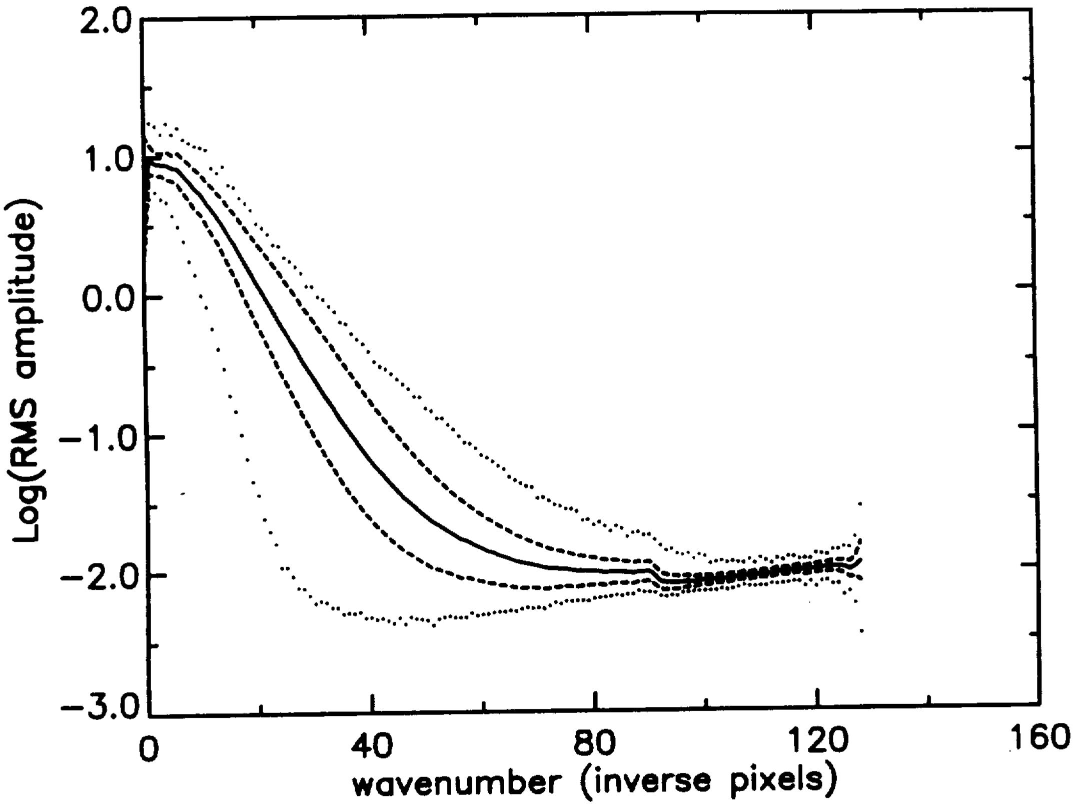

Figure 5.1: Spatial frequency log-spectra of Na D_1 −40 mÅ filtergrams. The solid central line is the mean log-power; the dashed lines are 1σ contours; the outer dotted lines are the maximum and minimum power at a given frequency of any image.

factor to the filtergram frequencies. Thus, the "MTF normalization" procedure forced the spatial spectrum of each filtergram to look like the average spectrum.

In principle the individual filtergrams could have been normalized to $S_{\max}$. This would have involved very large correction factors for the poorer filtergrams, and would have boosted the noise in these filtergrams considerably. Noise in filtergrams produces noise in dopplergrams and line center intensities in a nonlinear manner. So, instead, the difference between the mean spectrum and $S_{\max}$ was retained as a correction factor to be applied to the oscillation power. (See chapter 6.) As a final caveat, it should be noted that even the best images, assumed above to be diffraction limited, actually include some atmospheric blurring. Hence, the correction factor will provide an underestimate for power at the highest wavenumbers.

The MTF normalization procedure was checked by comparing filtergrams taken in poor seeing with filtergrams taken at almost the same time in good seeing. After normalization, both filtergrams showed the same solar structures.

5.4.2 Destretching

The displacements caused by atmospheric turbulence vary over the field of view. They are independent of one another over angular scales greater than the isoplanatic angle. Relative displacements between successive images can be measured by local correlation tracking (November 1986). This procedure finds the displacement of a small subarea of one image with respect to the other from the cross-correlation of the two. A displacement vector field is measured using a patchwork of subareas of the images. A relative displacement grid of 64 × 64 vectors was made, correlating each filtergram with the preceding one. This was done using standard software.

Local displacements are present not only because of seeing, but also because of wave motion and horizontal flows on the sun. We wish to remove the seeing displacements, but keep the real solar motions. It is possible to distinguish the two on the basis of timescale of the motion. Horizontal flows have characteristic timescales of hours, oscillations have timescales of minutes, and seeing has a timescale of tens of milliseconds. For filtergrams taken seconds apart, seeing motions will appear random, while solar motions will be coherent.

The seeing displacement grid was determined from the relative displacement grid as follows. For each vector component at each grid location, the relative displacements of preceding filtergrams were summed to produce a total net displacement (from the first frame). The total displacement was smoothed by convolution with a Gaussian of 90 s (5 bin) *fwhm*, and this smooth trend, subtracted to produce the seeing grid.

It is important to have high temporal resolution in the data. Correlation tracking can lock onto the crests of waves. So, if the impulse response function, used to smooth the data, is wider than ~ 120 s, the oscillations will be removed from the data along with the seeing. The standard Lockheed method for finding the seeing grid is designed for horizontal flow studies. It uses boxcar averages of 20 or more bins. This would be inappropriate for seismology studies.

With the seeing displacements measured, the images can be "destretched" to their undistorted states. The algorithm to do this treats images as rubber sheets, and stretches the sheets (by regridding) based on the local displacement vectors. This part of the process also used standard software. The set of filtergrams for each wavelength was destretched independently of the other wavelength sets. Destretched filtergrams taken at the same time, but different wavelengths, were then visually compared to ensure their features lined up.

5.5 Dopplergrams and Intensities

Velocity in m/s and line center intensity in arbitrary units were calculated at each pixel using equations 2.2 and 2.3. Because of the line centering problem described in section 4.1, the line center velocity and intensity were calculated using the −125, −40, and +40 mÅ filtergrams. The actual offsets of these measurements from the average line center was about −85, 0, and +80 mÅ. Each dopplergram and intensity image was given a time mark averaged from the time marks of the three filtergrams.

Filter tuning errors and seeing, which deteriorated toward the end of the run, produced some poor quality filtergrams in the data set. This in turned caused some nonsensical velocity and intensity determinations. Pixel velocities that were greater in magnitude than 10 km/s and intensities that were a factor of 10 greater than average were replaced with the mean velocity/intensity for that frame.

5.6 Image Drift

The rotational regridding assumes the images were rotating about a central point. In fact they rotate about the point centered in the spot tracker. This inconsistency produces a translational motion of the solar image. The point (on the sun) centered in the spot tracker, moreover, changes with time. This is caused by variable weighting of parts of the active region as the region evolves and as seeing conditions change.

From equation 2.27, it is evident that to keep oscillation frequencies from shifting by more than 60 μHz (0.5 frequency bins) at a wavenumber of 3 Mm^{-1}, the image drift must be less than 120 m/s. This is equivalent to 1.4 pixel/hr. Image drift is measured from the cross-correlation of successive images. (It is defined as the distance of the maximum of the cross-correlation from the origin.)

The image drift is traced out over time in figure 5.2. It was measured using the central 64×64 pixels of every tenth -125 mÅ filtergram. As can be seen from the figure, drift can be measured to significantly better than 1 pixel. The measured drift was smoothed by convolving the time series of each component of the vector with a Gaussian of 6 bin *fwhm*. The trend was then interpolated to the dopplergram and intensity time marks and removed from these images by regridding.

5.7 Angular Scale Determination

For full disk images of the sun, the image scale can be determined by measuring the radius of the solar disk. For high resolution images, however, the full disk is not visible, and indirect methods must be used. The scale of the La Palma images (0.8× lens) was determined by comparison of magnetograms from La Palma and the Kitt Peak National Observatory (figures 4.4 and 4.2). The Kitt Peak magnetogram was made at 15:17 UT on August 2, 1990, and has a scale of 1″/pixel to within 1% (Harvey 1991). The La Palma magnetogram was interpolated from magnetograms made at 13:35 UT and 16:27 UT.

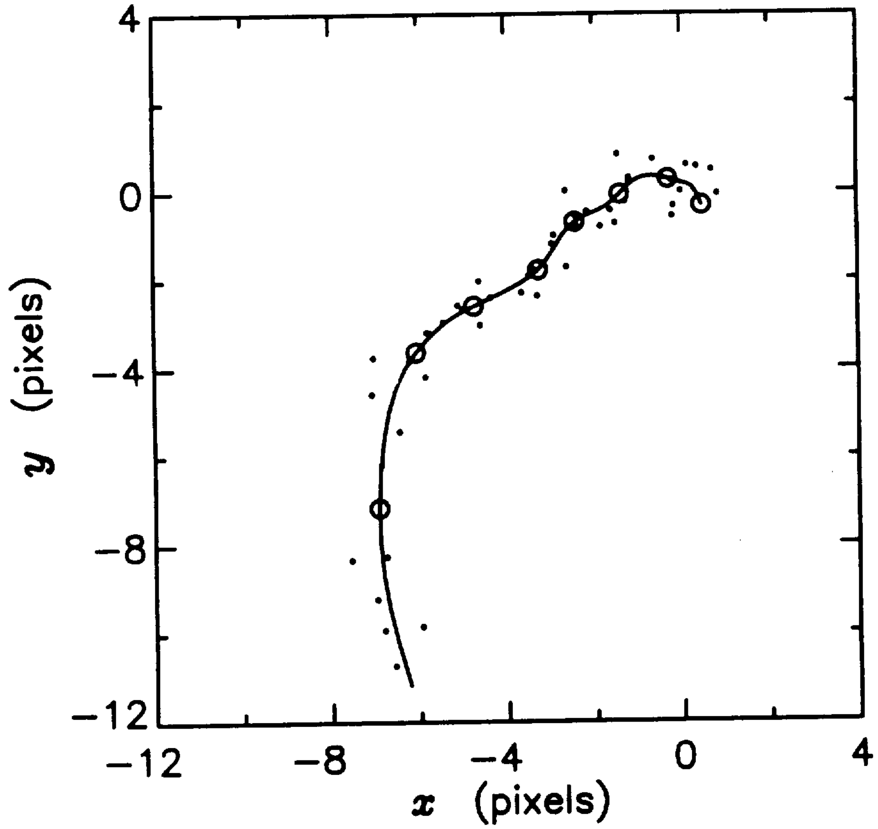

Figure 5.2: Image drift during observing run. Image motion determined by cross-correlation is traced out for the observing run. Points represent filtergrams taken 177 s apart; solid line shows low-pass filter of points; circles represent 18 min time marks ($t = 0$ is at upper right).

The interpolation method accounted for evolution of the active region by measuring the motion of the magnetic field structures using local correlation tracking. The two magnetograms were then stretched by the time-weighted local displacement grid. Finally, the time-weighted signals of the stretched magnetograms were added.

To compare magnetograms, 43 points on the La Palma magnetogram were flagged manually by cursor on a PIXAR computer. Corresponding points were flagged on the Kitt Peak magnetogram. Distances between a point and the centroid of the 43 points were then compared for the two magnetograms. The field of view for the La Palma images was, thus, determined to be (224.39 ± 0.70) Kitt Peak pixels. Assuming the Kitt Peak scale measurement,

$$\text{La Palma Field of View} = 224'' \pm 2'' \text{ (square)} \tag{5.3}$$

Chapter 6

Measurements from Power Spectra

The sets of dopplergrams and intensities were apodized in the space and time directions with Blackman-Harris functions (equation 2.32). Three-dimensional FFT's were calculated for the full field of view, as well as for the three $79'' \times 79''$ subfields shown in figure 6.1. The temporal and spatial Nyquist frequencies were 28.3 mHz and 9.9 Mm^{-1}, respectively. The frequency bin size was 117 μHz, and the wavenumber bin size, 0.039 Mm^{-1} for the full field, and, 0.11 Mm^{-1} for the subfields.

The squared modulus of each Fourier transform was calculated to produce a 3-d power spectrum $P(\vec{k}, \nu)$. The dispersion relations given by equations 1.7 and 1.9 are symmetric about the $k = 0$ axis. They define "trumpet" shaped surfaces (Hill 1988) of approximate form $\nu \propto |\vec{k}|^{1/2}$. (See figure 6.2.) This symmetry allows us to integrate the power over the azimuthal coordinate, in order to increase the signal to noise ratio. The resultant, collapsed power spectrum $P(k, \nu)$ will show ridges of power at frequencies given by the dispersion relations for the p-modes and f-modes.

Properties of the oscillations, such as the dispersion relation and mode power, were measured from the collapsed power spectra. This was accomplished by fitting one-dimensional slices of the spectra. Fits were then compared with theoretical predictions to evaluate models of the solar atmosphere. Magnetic versus nonmagnetic regions were compared to search for differences in wave properties between the two regions.

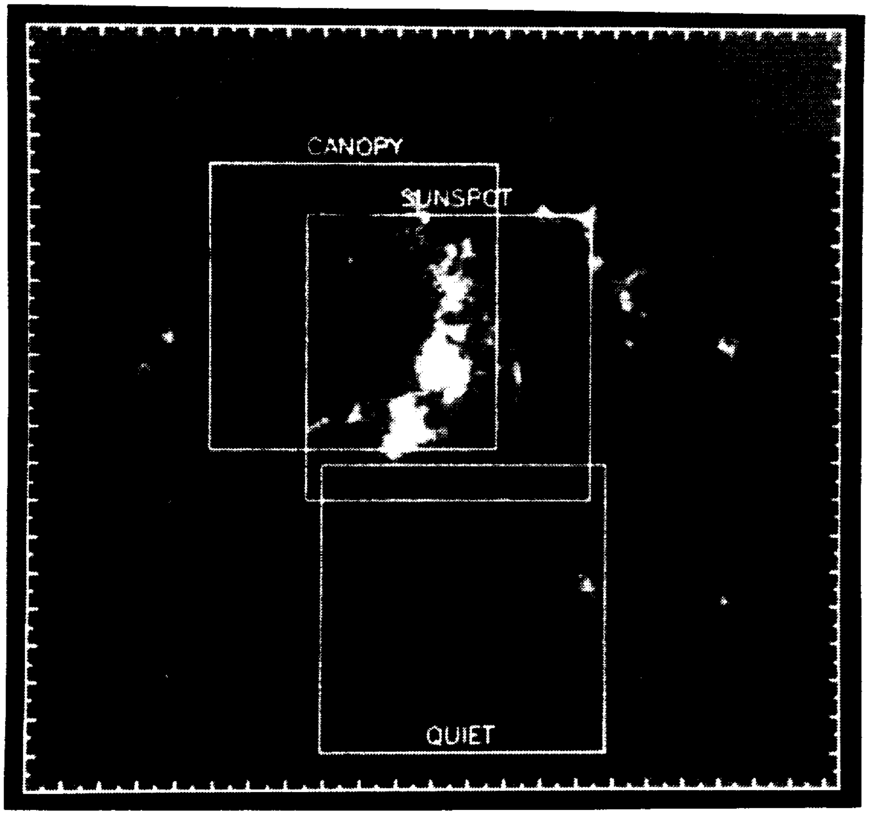

Figure 6.1: Magnetogram of AR6181. The three outlined subfields were used separately to measure wave properties in network field and quiet regions. The small tick marks are 5″.

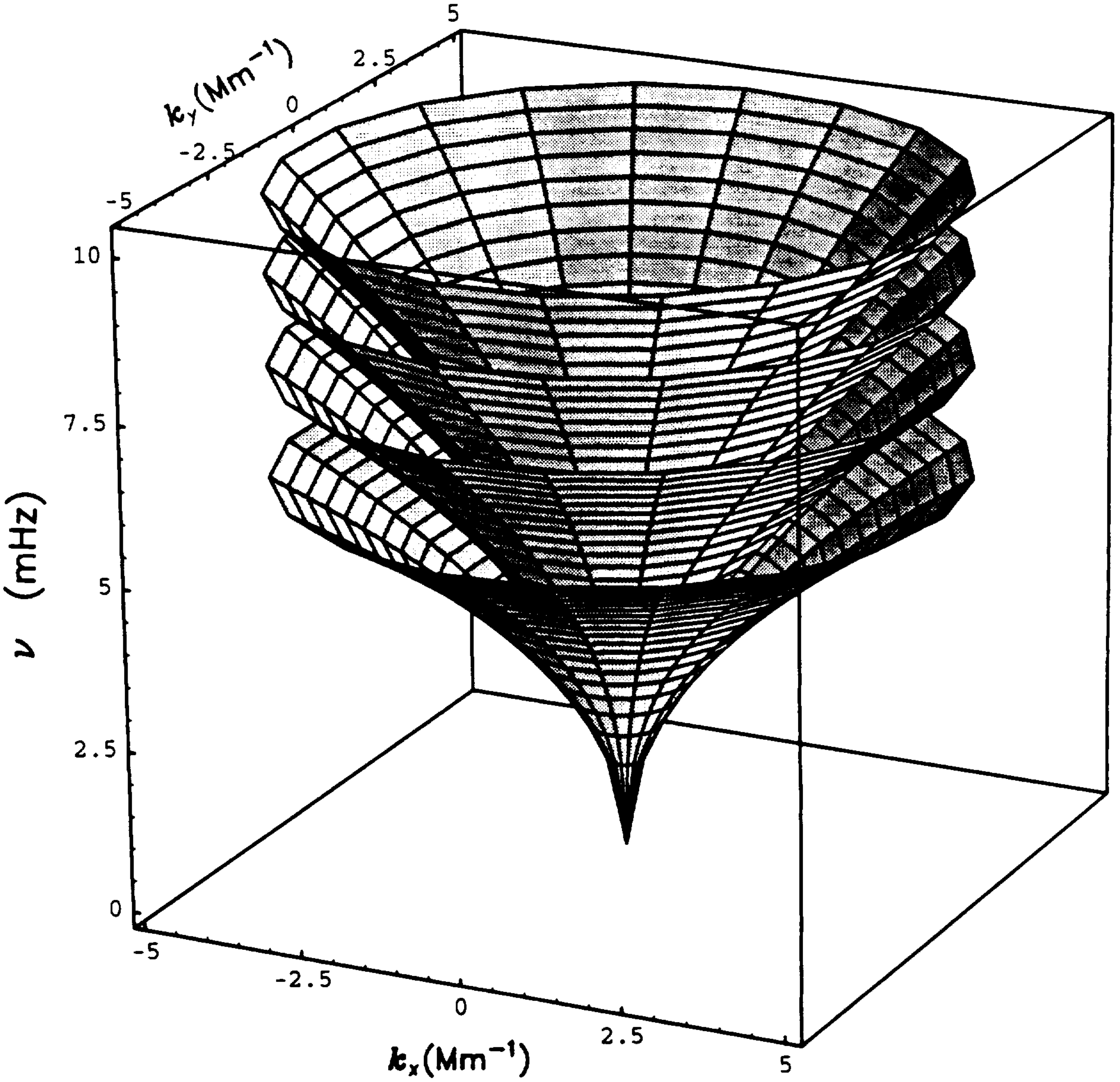

Figure 6.2: Surfaces of power in $(\vec{k}, \nu)$ space.

6.1 Collapsing 3-d Power Spectra

The azimuthal symmetry of equations 1.7 and 1.9 is realized only in solar coordinates, comoving with the gas. In practice, one or both of these conditions may not be met. The frequency shift described by equation 2.27 occurs, with a cosine dependence on azimuth θ, if there is a relative (horizontal) motion between the observer's coordinates and the gas. The rigid alignment procedure described in section 5.6 keeps the observational coordinates fixed with respect to the sunspot. It has been shown, however, that there is relative motion between magnetic flux and nonmagnetized gas (Snodgrass & Ulrich 1990). Hill (1988) finds flows of $\sim$ 100 m/s below the photosphere.

Visual inspection of the power spectra did not reveal evidence of flows. Thus, if present, flows produce frequency shifts of less than one frequency bin (117 μHz). If plane waves propagated isotropically, a sinusoidal frequency shift with θ would serve to widen the ridges in the collapsed power spectra. In the measured spectra, however, power depends mildly on angle θ. Thus, a horizontal flow would produce a slight asymmetry in addition to broadening a ridge.

The second condition affecting the symmetry of the trumpets is geometrical. For observations away from disk-center, the projection of solar coordinates onto observational coordinates causes foreshortening. Waves propagating toward or away from disk-center appear with shorter wavelength (higher wavenumber) than waves propagating in the perpendicular direction. This foreshortening distorts the cylindrical symmetry of the trumpets to give them an elliptical rather than circular cross section. Procedures to measure and compensate for this effect are described below.

6.1.1 Distance Scale Determination

The distance scale of the images or, equivalently, the wavenumber scale of the power spectra follows from trigonometry, once the magnitude and direction of foreshortening have been determined. This measurement was made by fitting an ellipse to the cross section of a trumpet in a 3-d power spectrum.

A constant frequency slice, in the 5-minute band, of the full-field Doppler spectrum is shown in figure 6.3. The slice has been remapped to cylindrical polar coordinates.

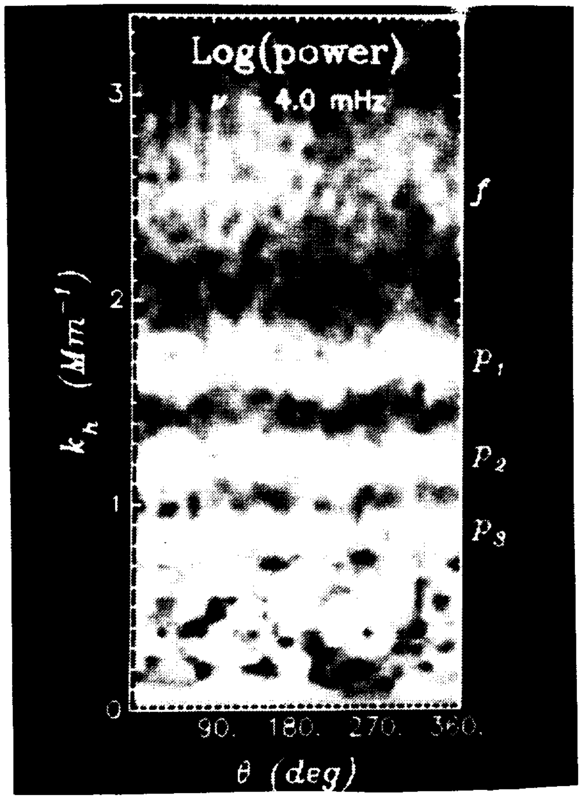

Figure 6.3: Constant frequency slice of the 3-d power spectrum. A slice at 3.99 mHz has been remapped to cylindrical polar coordinates. Log(*power*) is shown as a function of wavenumber and azimuth.

So, the cross section of a trumpet appears at roughly constant wavenumber for all values of θ. These horizontal bands of power are the "rings" described by Hill (1988). In polar coordinates, an ellipse centered at the origin has the form,

$$k = k_0[1 - (1 - \mu^2)\cos^2(\theta - \theta_0)]^{-\frac{1}{2}} \tag{6.1}$$

where k_0 is half the minor axis (the true wavenumber); θ_0 is the angle of the major axis (direction toward disk-center); and μ is the ratio of minor to major axes (the fractional foreshortening). A close inspection of figure 6.3 shows that each of the bands exhibits this oscillatory behavior of k as a function of θ.

The values of k_0, θ_0, and μ were fitted to the measured wavenumber $k(\theta)$ for the p_1 ring in the frequency slice $\nu = 3.99$ mHz. The function $k(\theta)$ was defined as the wavenumber at peak power in the constant frequency slice. It was determined by quadratic interpolation. The measured fractional foreshortening was,

$$\mu = 0.956$$

This corresponds to a distance from disk-center of 17°, which agrees with an approximate measurement made from the full-disk magnetogram in figure 4.2.

The assumption of a planar atmosphere has been made here, in treating the foreshortening as constant across the field of view. If the foreshortening varies appreciably, modes of different wavenumber will be mixed in the 3-d power spectrum. This will smear the trumpet surfaces in $(\vec{k}, \nu)$ space in a manner which cannot be corrected. For large fields of view, the images must be mapped to "flattened" coordinates before transforming to Fourier space. The aplanarity for the data analyzed here was not great enough to warrant such treatment.

The 224″ field of view represents 13° along a great circle on the Sun. Since the average distance from disk-center was about 17°, plane waves propagating along the direction of foreshortening will be mixed over a wavenumber range of ±3.5%. While this may seem large, only the waves propagating exactly along a diameter of the disk experience mixing to this extent. Waves propagating in the perpendicular direction are not mixed at all. The net widening of the ridges is, thus, small. This can be seen in figure 6.3. The width of the ridges appears independent of θ. The width, therefore, is not an artifact of the coordinate system.

6.1.2 Azimuthal Projection

The power was integrated around ellipses in the (k_x, k_y) plane. To do this, k_0 was computed from equation 6.1 for each ordered pair (k_x, k_y) in the 3-d spectrum, and power from that bin was added to the appropriate k bin in the 2-d spectrum. Bins in the 2-d spectrum were normalized by (multiplying by) the ratio of the area of an elliptical band to the number of bins accumulated from the 3-d spectrum. The area A of an elliptical band was approximated by,

$$A = w\frac{\pi}{2}\sqrt{a^2 + b^2} \tag{6.2}$$

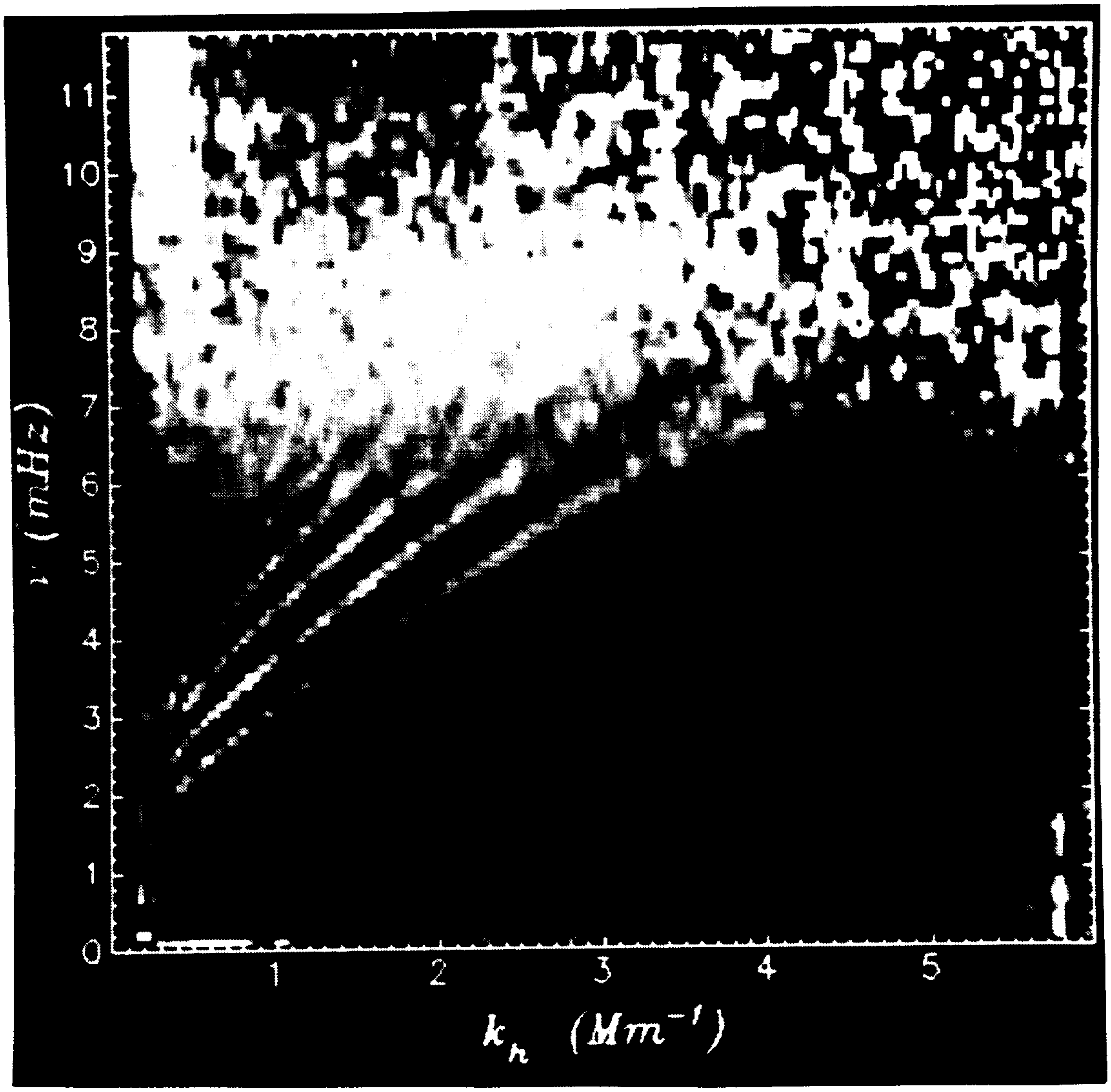

Figure 6.4: Scaled velocity-power spectrum. A portion of the collapsed power spectrum for the full field of view, with variable gray-scaling in the k and ν directions. Background has been subtracted. The noise visible at the top of the spectrum is an artifact of the scaling. From Fernandes *et al.* (1992).

where a and b are the major and minor axes of the ellipse; and w is the width of a wavenumber bin in the 2-d spectrum. The two-dimensional spectrum $P(k, \nu)$ for the full-field dopplergrams is shown in figure 6.4.

6.2 Parametrization and Least-Squares Fitting

6.2.1 Fitting Procedure

The frequencies, widths, and heights of the ridges were measured as functions of wavenumber. To do this, constant wavenumber slices of the power spectra were individually fitted by least-squares method. Examples of slices at constant wavenumber appear in figure 6.5. A single isolated mode should have a Lorentzian profile.

$$P(\nu) = \frac{P_0 \Gamma / 2\pi}{(\nu - \nu_0)^2 + \Gamma^2/4} \tag{6.3}$$

where P_0 is the mode power; ν_0 is the mode frequency; and Γ is the *fwhm*. The high frequency mock modes described by Kumar *et al.* (1990) should have a sinusoidal profile.

$$P(\nu) \propto \frac{\sin^2(\omega x_0/c)}{\omega^2 - {\omega_c}^2 \sin^2(\omega a/c)} \tag{6.4}$$

where x_0 is the source depth; ω_c is the acoustic cutoff; and a is the height of the upper reflecting surface. Solar processes such as horizontal flow fields, and measurement effects such as seeing and apodization tend to smear the shape to produce a Gaussian profile.

$$P(\nu) = \frac{P_0}{\sigma\sqrt{2\pi}} e^{-\frac{(\nu-\nu_0)^2}{2\sigma^2}} \tag{6.5}$$

where P_0 is the mode power; ν_0 is the mode frequency; and $\sigma = fwhm/2.36$.

The ridges lie on top of a background which decreases monotonically with wavenumber. In the photosphere, the granulation is caused by overshoot of convective cells into the overlying convectively stable layers. The power, in the photosphere, below the *f*-modes is caused by this convective overshoot. Extrapolation of calculations of Nesis & Mattig (1989) to the low chromosphere suggests a similar explanation for the background power there.

Because of the uncertainty of the physical description for the background, there is no proper way to parametrize it. Nevertheless, the background must be accounted for to avoid contaminating the ridge fits. It can either be included as an extra term in the fits, or fit independently and subtracted from the power spectrum before fitting the ridges.

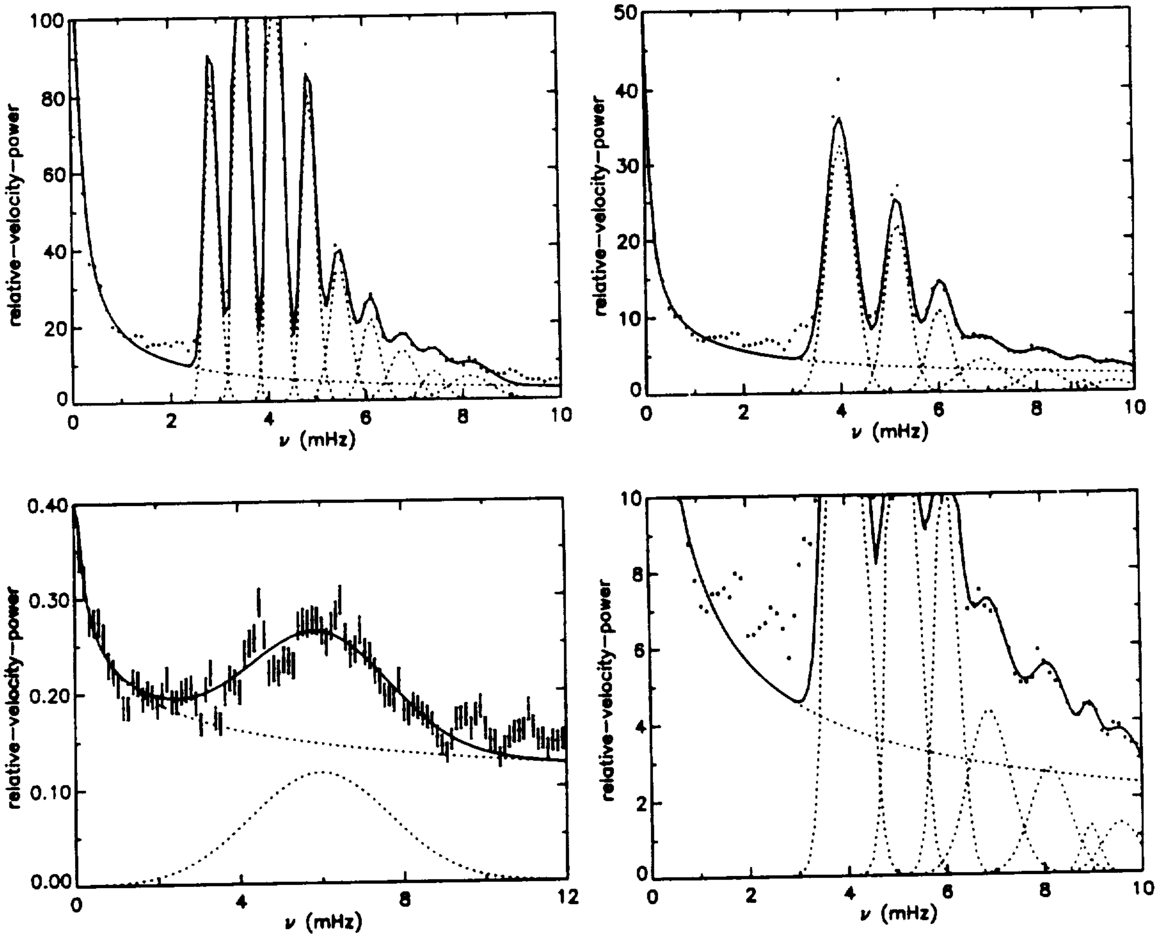

Figure 6.5: Constant wavenumber slices of the 3-d power spectrum. Data are plotted as points with error bars. Background and individual Gaussian modes are plotted as dashed lines; and the sum of background and modes is plotted as a solid line. Top left: k = 1.16 Mm^{-1}; Bottom left: k = 5.25 Mm^{-1}; Right (top & bottom): $k = 2.34$ Mm^{-1}.

The latter method was chosen because the background could be well characterized using the range of frequencies on either side of the ridges. The shape of the background P_k suggested a power law parametrization.

$$P_k(\nu) = A_k \nu^{-B_k} \tag{6.6}$$

where A_k and B_k are parameters fitted independently for each wavenumber slice. The frequency ranges used for the background fits include: $(0.12 < \nu/\mathrm{mHz} < 1.3)$ and $(12.0 < \nu/\mathrm{mHz} < 15.0)$.

The ridges were fitted after subtracting the background. As can be seen from figure 6.5, the ridges overlap, and so must be fitted simultaneously. With three parameters per Gaussian, and up to eight visible ridges, the fits involved up to 24 parameters at a time. This large parameter space combined with noisy data necessitated the development of a very robust fitting algorithm.

The fitting program is described in the next section. It provides a nonlinear, weighted, least-squares fit to ungridded data. The weights used in the least-squares fit were the measurement errors. Hence, the fitting procedure minimized χ^2. The error on the power was estimated from equation 2.38. This in turn assumed the velocity and intensity errors derived in section 2.1.

6.2.2 Levenberg-Marquardt Method for Nonlinear Regression

The basic algorithm follows the Levenberg-Marquardt procedure (Press *et al.* 1989). The method attempts to minimize the χ^2 in parameter space $(\vec{a})$, given N measured values $y_i \pm \sigma_i$ at points x_i.

$$\chi^2(\vec{a}) = \sum_{i=1}^{N} \left(\frac{y_i - y(x_i; \vec{a})}{\sigma_i} \right)^2 \tag{6.7}$$

where $y(x; \vec{a})$ is the fitted function.

The minimum of the surface $\chi^2(\vec{a})$ is searched for in an iterative manner. Successive guesses for the parameter vector $\vec{a}$ are made based on the gradient and curvature matrix for the χ^2 surface. When the distance to the minimum, as estimated from the curvature, is large, the gradient is weighted more heavily in the guess. When the minimum is near, the curvature carries more weight. The algorithm assumes it has found the minimum when it can no longer reduce χ^2 by more than 0.1. The covariance matrix for the fit is simply the inverse of the curvature matrix at the minimum.

To prevent runaways, the parameters are tested after each iteration of the algorithm in which χ^2 is reduced. Parameters that are not within set limits are fixed at appropriate values, and no longer varied in the fit. The remaining parameters are reset to their initial values $\vec{a}_0$, and the procedure starts again from the beginning.

For Gaussian ridges, the limits for the height parameter are ϵ (small, positive) and $h_{\max}$ (very large). Values falling outside the limits are fixed at the limit. The limits for the width parameter are one-half and twice the expected width. Again, values falling outside the limits are fixed at the limit. The limits for the frequency parameter fall halfway between the expected positions for ridges ($\vec{a}_0$). For the bottom (top) ridge in a fit, the lower (upper) limit is defined such that the two limits are equidistant from the expected ridge position. Values falling outside the limits are fixed at the initial guess $\vec{a}_0$.

The reason for this treatment of parameter limits is to prevent noisy ridges from disturbing the fits of adjacent ridges. *Ridges which are too noisy to be properly fitted are treated as background.*

For the first spectrum to be fitted, initial guesses at a number of wavenumbers were made by eye, using cross hairs on a workstation display. Guesses at other wavenumbers were interpolated or extrapolated from the nearest four fitted wavenumber slices. For the remaining power spectra, initial guesses were interpolated from the already fitted spectra.

In addition to the background and ridge fits, the least-squares fitting program was used to interpolate and extrapolate mode frequencies to make the initial guesses, and to determine the parameters of equation 6.1 in section 6.1.1.

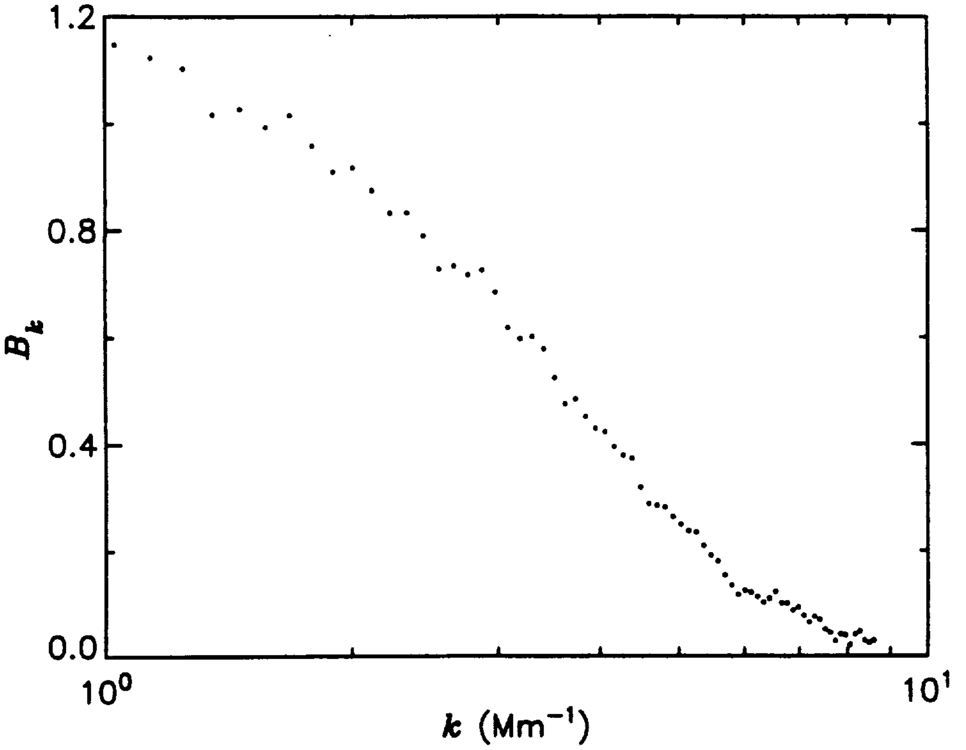

Figure 6.6: Power law exponent for background fit. Exponent vs. wavenumber.

6.3 Results of Fits

6.3.1 Background

The exponent to the power law fit is plotted in figure 6.6. The background velocity power, integrated over frequency, is plotted in figure 6.7. The spectrum falls off much more slowly with wavenumber than the spectrum of convection in the photosphere reported by Chou *et al.* (1991). The root-mean-square (RMS) velocity is about 820 m/s. Nesis & Mattig (1989) have measured RMS velocities, due to "mechanical overshoot", that increase with height in the upper photosphere. Their model predicts the height dependence, for line-of-sight velocities, shown in figure 6.8. A smooth extrapolation of this curve to the height of formation of the Na D_1 line (500–700 km) yields an RMS velocity of 700–1100 m/s, in agreement with our measurements.

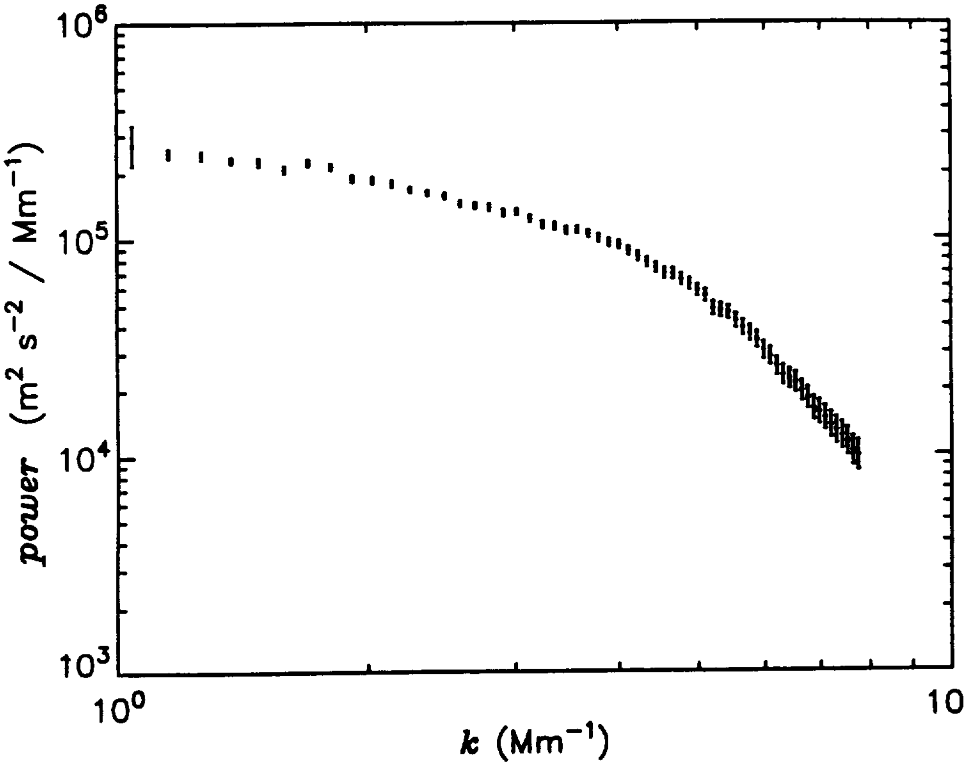

Figure 6.7: Background velocity power integrated over frequency. Background was fitted from the "quiet" subfield spectrum. From Fernandes *et al.* (1992).

6.3.2 Mode Frequencies

Frequencies of ridges from the full-field velocity and intensity spectra, and the quiet subfield velocity spectrum are tabulated with their respective statistical errors in appendix A. The velocity points are plotted in figure 6.9. All tabulated points correspond to fits in which the offset, width, and height of the Gaussian converged to physically reasonable values, and the integrated power under the Gaussian was at least 4 standard deviations above the background.

All six fitted p-mode ridges extend up to at least 7.0 mHz. The p_5 and p_6 ridges extend up to a frequency of 9.5 mHz. There is no deviation from a smooth extrapolation of the ridges at lower frequencies. Libbrecht, Woodard & Kaufman (1990) have made measurements that overlap with ours at frequencies up to 5.3 mHz. As can be seen from figure 6.10, the fitted frequencies are consistently higher than those of Libbrecht *et al.* by an average of (35 ± 13) μHz. This difference, however, is only a quarter of the frequency bin width, and is indicative of the systematic error in the

Q-2

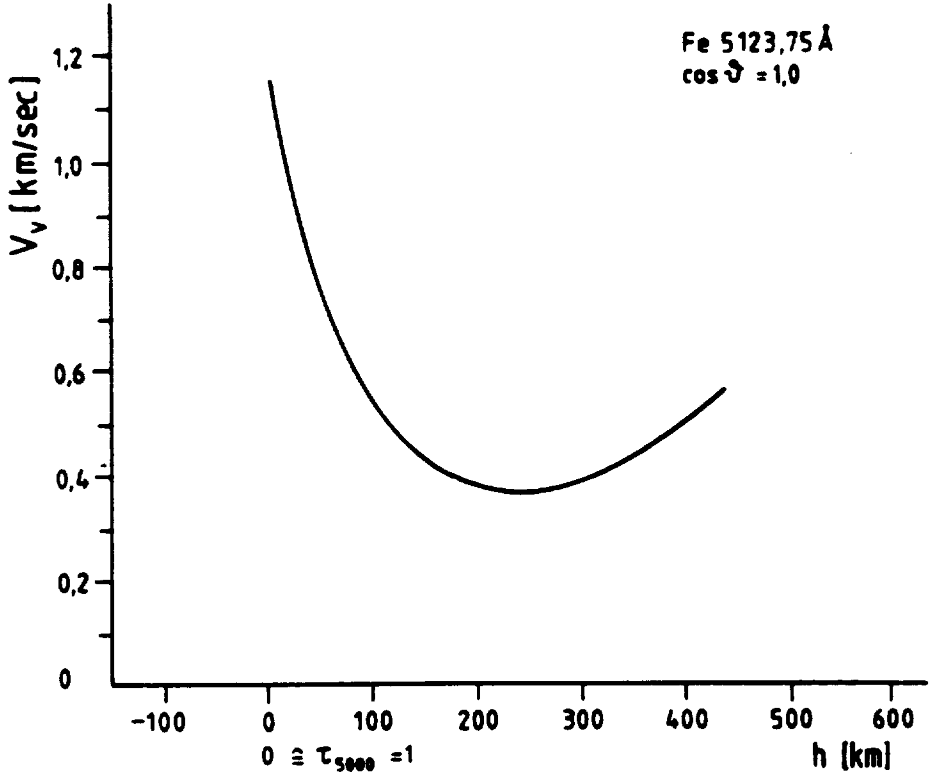

Figure 6.8: Calculated Doppler velocity vs. height for the Fe I (5123.75 Å) line. From Nesis & Mattig (1989).

measurement.

The *f*-ridge is visible at wavenumbers up to 5.57 Mm^{-1}. There is, however, a systematic discrepancy between frequencies fitted from the velocity and intensity spectra as can be seen from figure 6.11. Frequencies measured from the velocity spectra are consistently higher than those from the intensity spectra by up to 50 μHz at wavenumbers below 2.5 Mm^{-1}. This difference increases to $\sim$ 100 μHz at 4 Mm^{-1}. The discrepancy may in part be due to a difference between background shapes in the velocity and intensity spectra.

Libbrecht *et al.* (1990) report a Gaussian background, centered near 3 mHz, in their velocity spectrum. Inclusion of such a background in our velocity fit would bring the *f*-ridge frequencies into better agreement with the intensity data at wavenumbers below 1.1 Mm^{-1}, but would push them farther apart at higher wavenumbers. Fitting such a background function, moreover, would require a longer time series with correspondingly better signal-to-noise ratio. It is noteworthy that the *f*-mode frequencies measured from the intensity spectra differ with those reported by Libbrecht *et al.* by

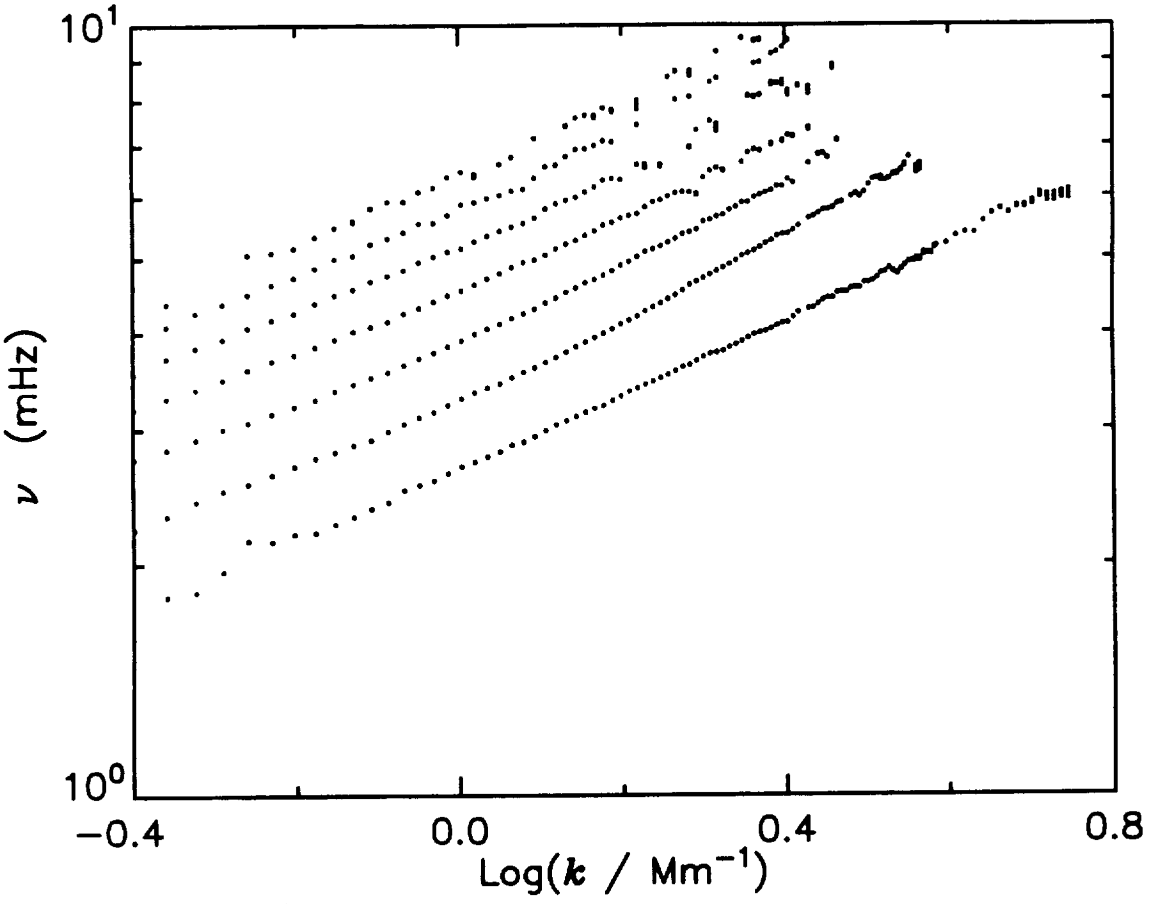

Figure 6.9: Measured mode frequencies (from velocity spectra): ν vs. $\log_{10} k$. Frequencies of the f and p_1–p_6 ridges are plotted with 1 σ error bars. For $k < 3.82$ Mm^{-1}, frequencies are taken from the full-field spectrum. At higher k, values from the quiet subfield are plotted.

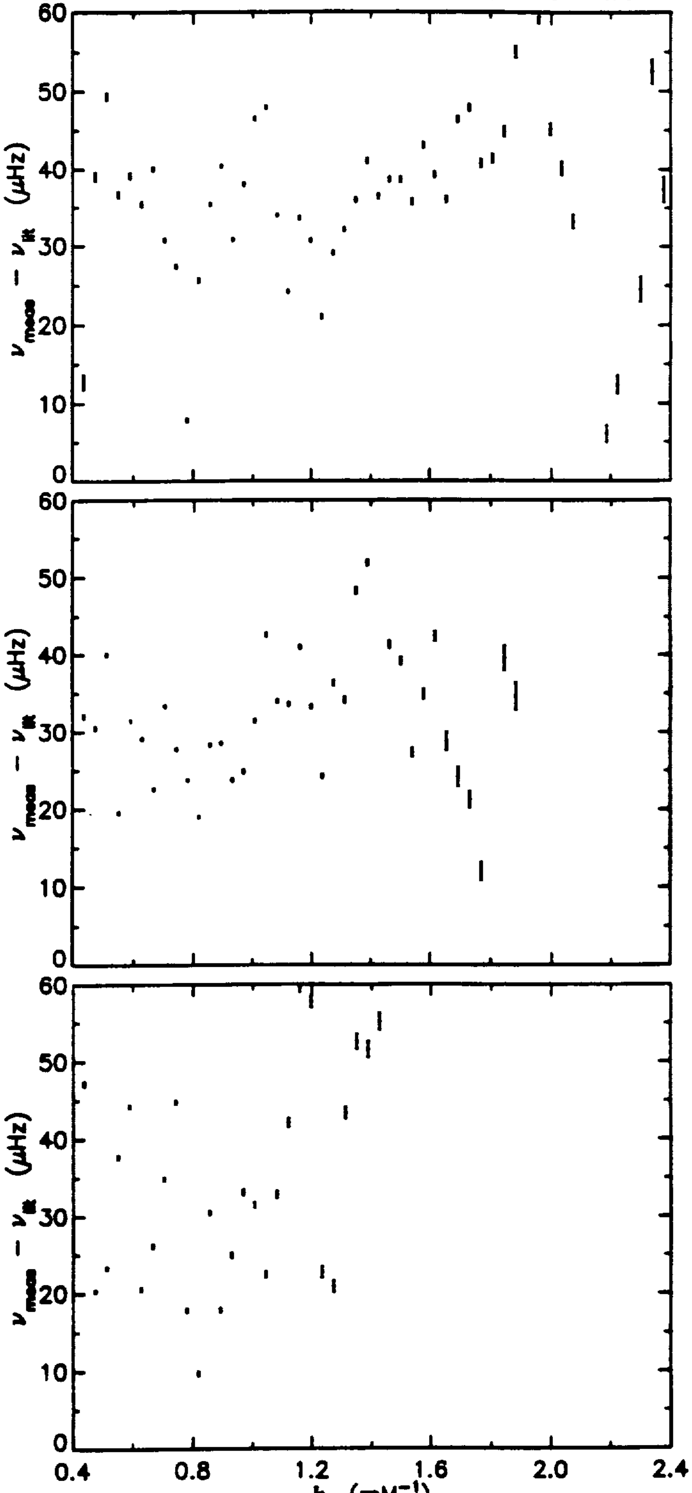

Figure 6.10: Comparison of measured p-mode frequencies with Libbrecht *et al.* (1990). Frequency difference vs. k is plotted for p_1, p_2, p_3 (from top down).

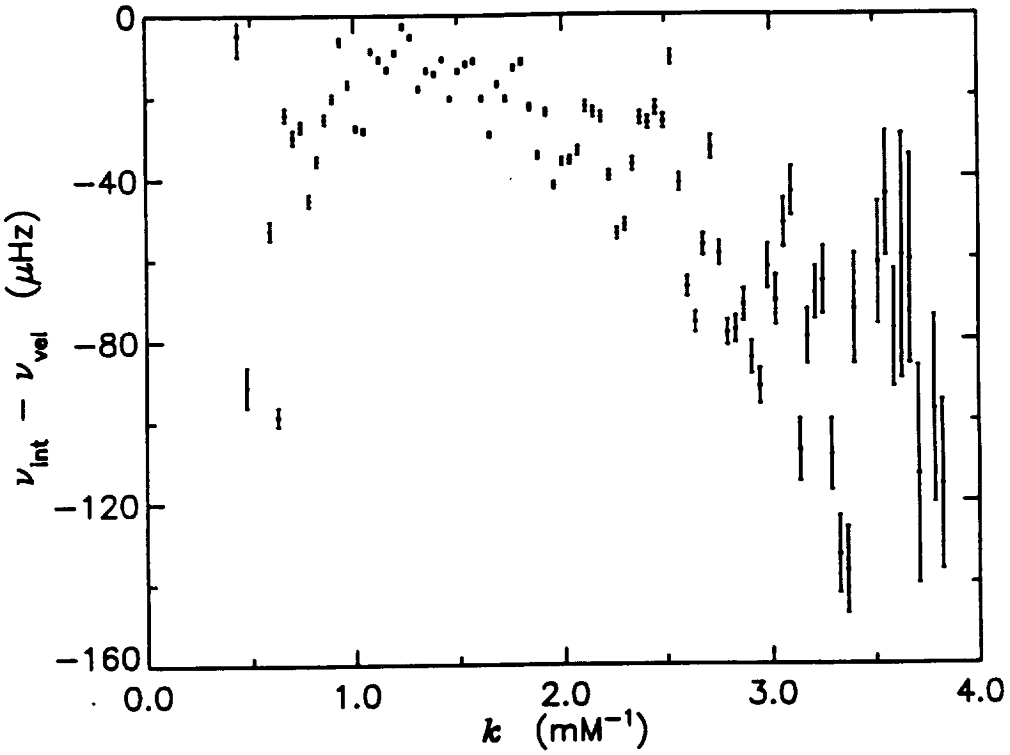

Figure 6.11: Comparison of f-mode frequencies measured from velocity and intensity. Frequency difference vs. k.

under 30 μHz, as shown in figure 6.12.

The weighting of magnetic regions is different for intensity and velocity spectra. However, as shown in section 6.3.5, the discrepancy is not caused by a difference in mode frequencies in the magnetic and nonmagnetic regions within the field of view. Regardless of which set of f-mode frequencies we use, the measured frequencies lie below the theoretical frequencies given by equation 1.9 at wavenumbers greater than 1 Mm^{-1}. The difference is 100–200 μHz at 4 Mm^{-1}. The fractional difference between measured and theoretical frequencies is plotted in figure 6.13.

6.3.3 Mode Widths

Ridge widths are plotted as error bars to the frequencies in figure 6.14. The ridge widths at low frequency are due to the apodizing function. At high frequency, the ridges are broader than expected for mock modes. The measured widths probably do not represent the true widths. The width is the most sensitive parameter to noise in

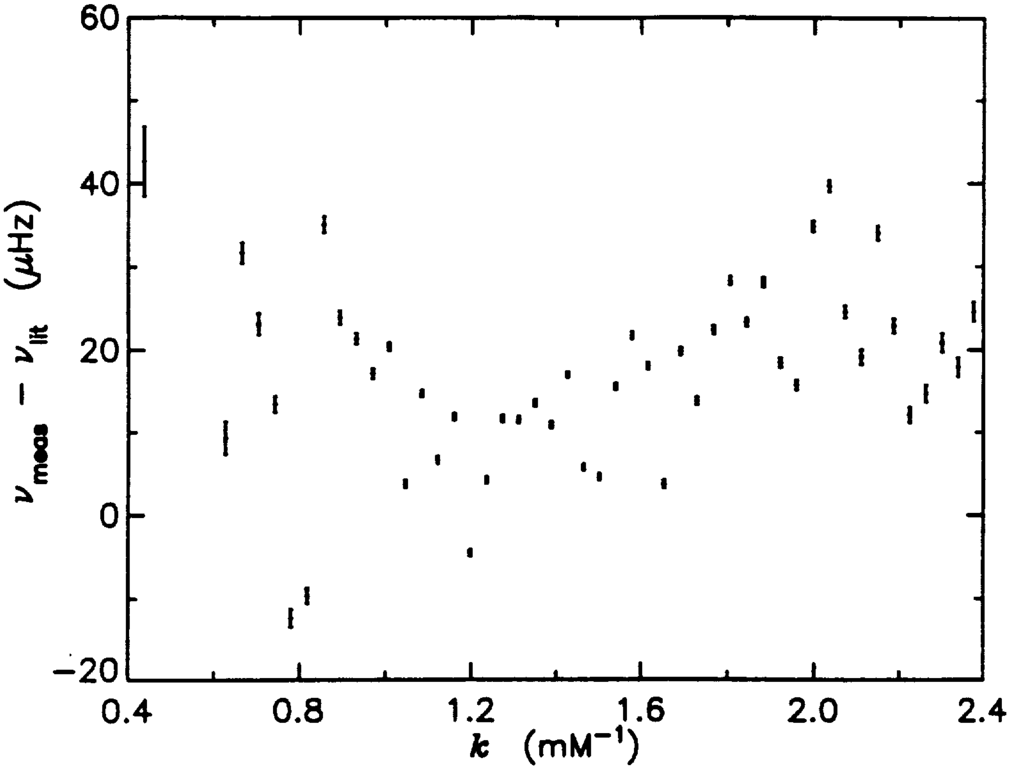

Figure 6.12: Comparison of f-mode frequencies from full-field intensity spectrum with Libbrecht *et al.* (1990).

the fitted power spectrum.

6.3.4 Mode Power

Mode power is defined as the integral under the fitted Gaussian.

$$P = \frac{\sqrt{2\pi}}{2.36} hw \tag{6.8}$$

where h is the height of the ridge; and w, the *fwhm*. The error on the power is given by,

$$\sigma_P = P\sqrt{\left(\frac{\sigma_h}{h}\right)^2 + \left(\frac{\sigma_w}{w}\right)^2 + 2\frac{\sigma_{hw}{}^2}{hw}} \tag{6.9}$$

where $\sigma_{hw}{}^2$ is the covariance of the height and width. The mode power is plotted as a function of frequency in figure 6.15. The p-mode power has the same frequency dependence for all p-ridges. There is very little explicit wavenumber dependence. Power increases as $\nu^{7.3}$ to a maximum at 3.4 mHz, at which point it turns over and

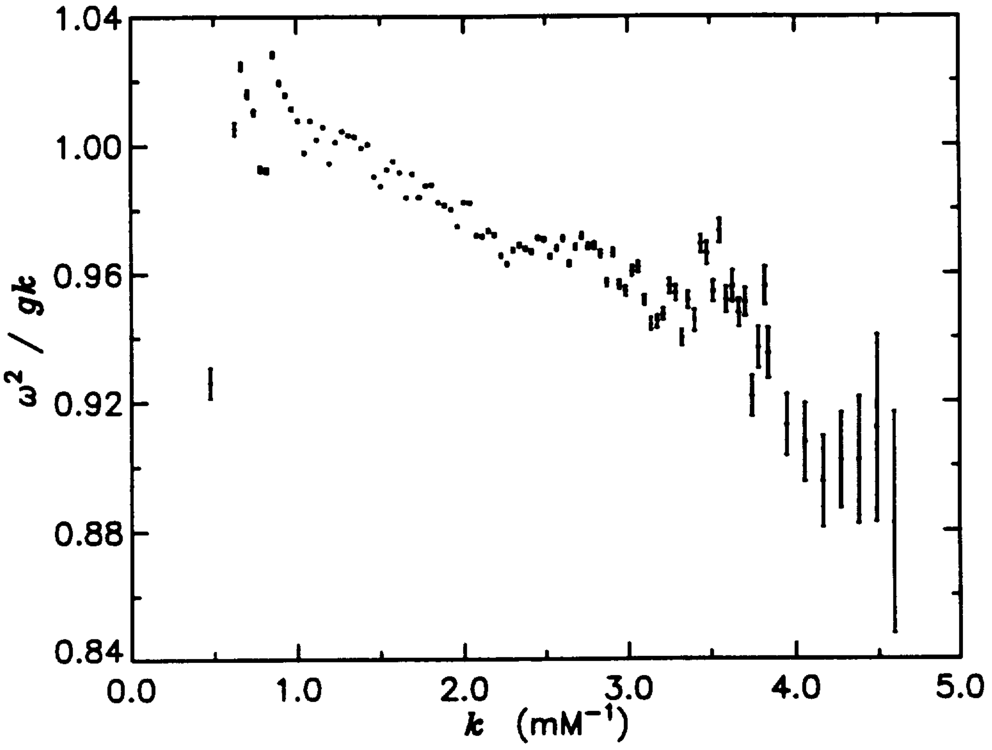

Figure 6.13: Comparison of measured f-mode frequencies with theory. Frequencies from the full field intensity spectrum are compared with the relation $\omega^2 = gk$ ($g = 274.1\ m/s^2$).

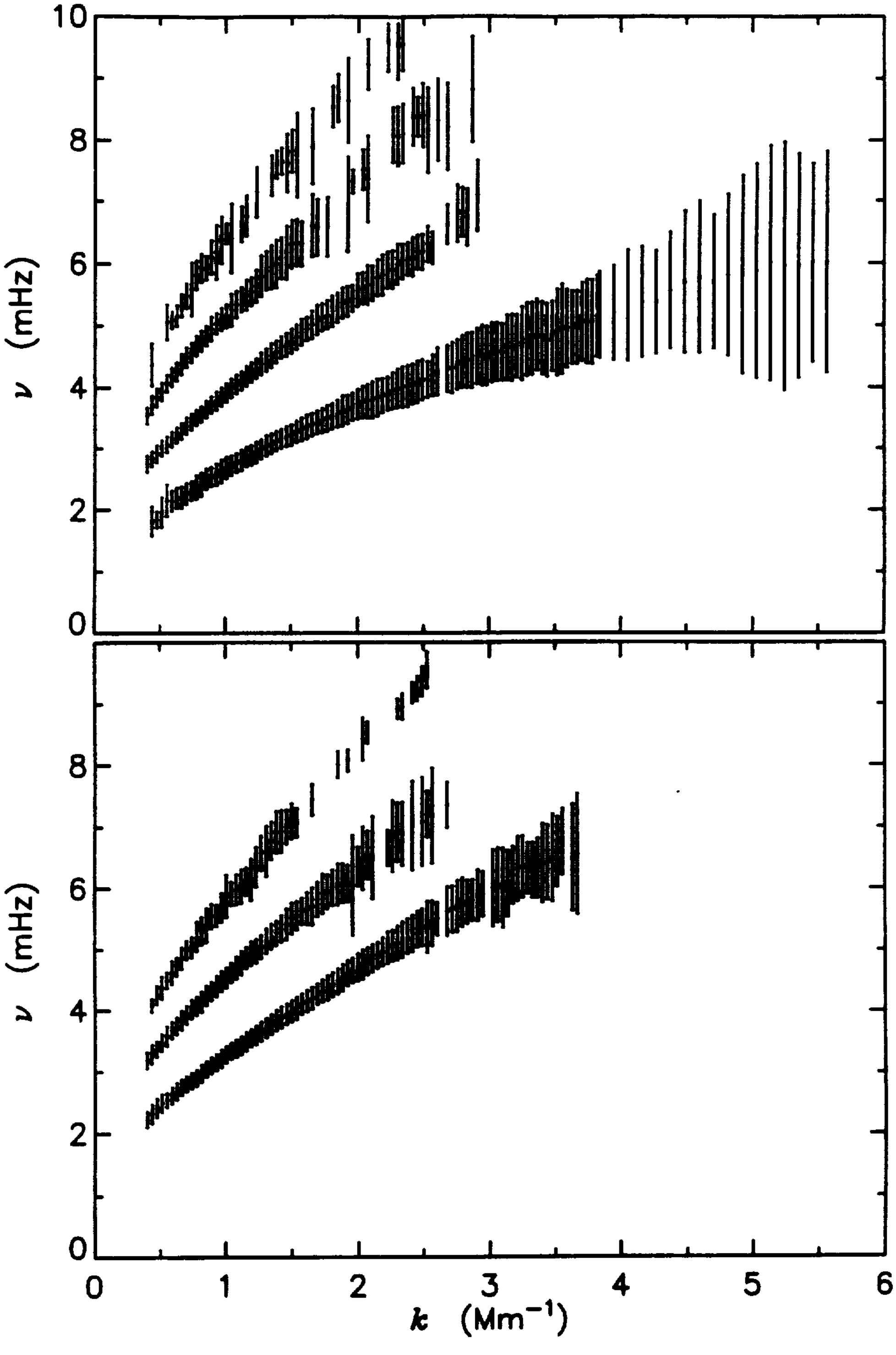

Figure 6.14: Frequency and ridge width vs. k. Top plot shows f-modes and even order p-modes. Bottom plot shows odd ordered p-modes. Error bars represent the *fwhm* from the fit.

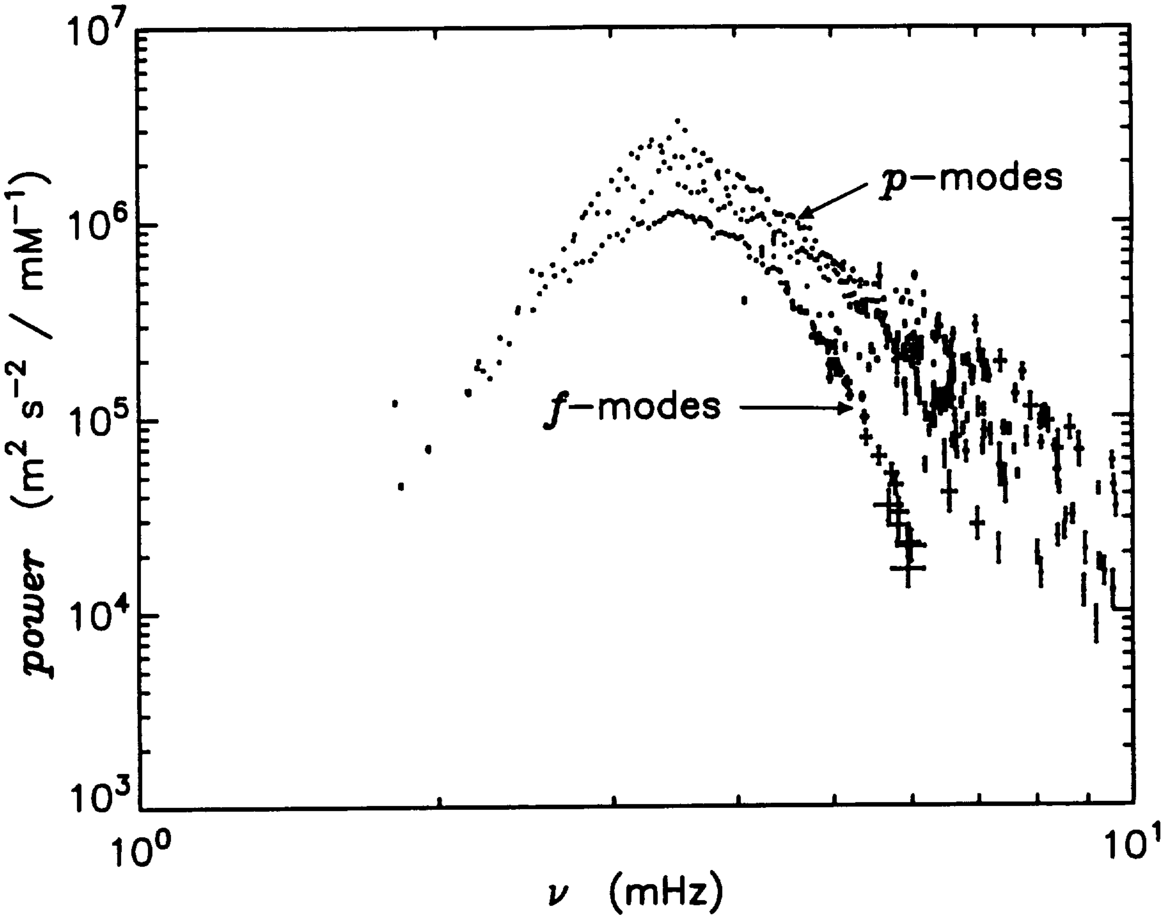

Figure 6.15: Velocity power vs. mode frequency. From Fernandes *et al.* (1992).

falls off again as $\nu^{-4.6}$. The f-modes have less power at a given frequency than the p-modes. As surface gravity waves with very little compression they are physically different from the p-modes and are not expected to show the same power spectrum.

An MTF correction was made to the power plotted in figures 6.7 and 6.15 by combining the calculated MTF of the telescope and CCD with the estimated atmospheric MTF. See sections 3.4 and 5.4.1.

6.3.5 Comparison of Magnetic and Nonmagnetic Regions

Mode frequencies were compared for the quiet, canopy, and sunspot subareas shown in figure 6.1. The frequency differences are plotted in figures 6.16 and 6.17. The frequencies of ridges in each subarea agree with those of the other subareas to within

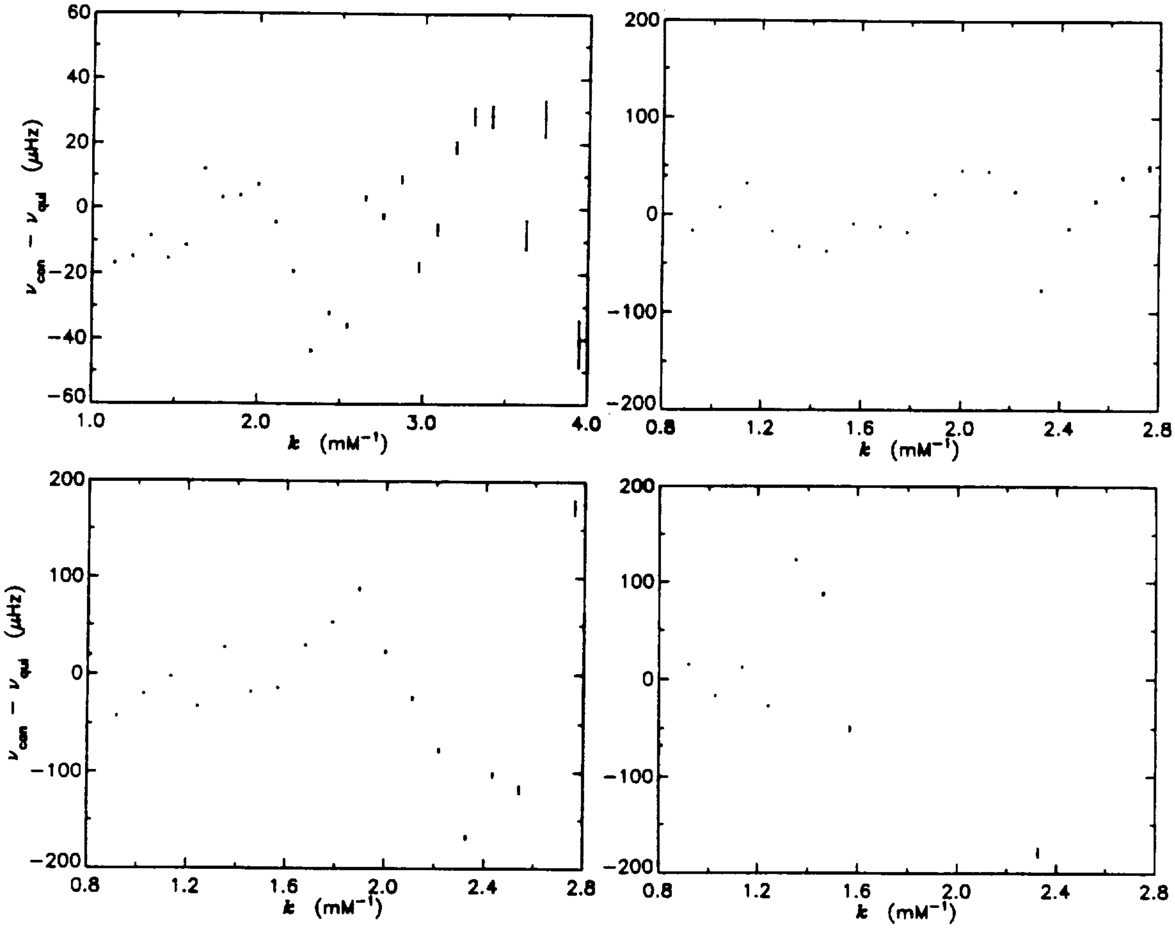

Figure 6.16: Mode frequency differences for canopy and quiet subfields. Top left, f-mode; top right, p_1; bottom left, p_2; bottom right, p_3.

the scatter of the data (± 40 μHz).

The experimental scatter is much larger than the error bars derived from the fit. This may simply indicate an underestimation of the velocity error, or it may be a result of solar noise. Modes of finite lifetime have an intrinsic frequency uncertainty. Determination of the frequency of the cavity resonance ν_0 requires observations for several mode lifetimes. The 2.4 hr observing run probably constitutes less than one mode lifetime over much of the wavenumber range. Hence, the measured frequencies will be distributed about ν_0 in a manner which depends on the mode lifetime, and shape of the wavepackets.

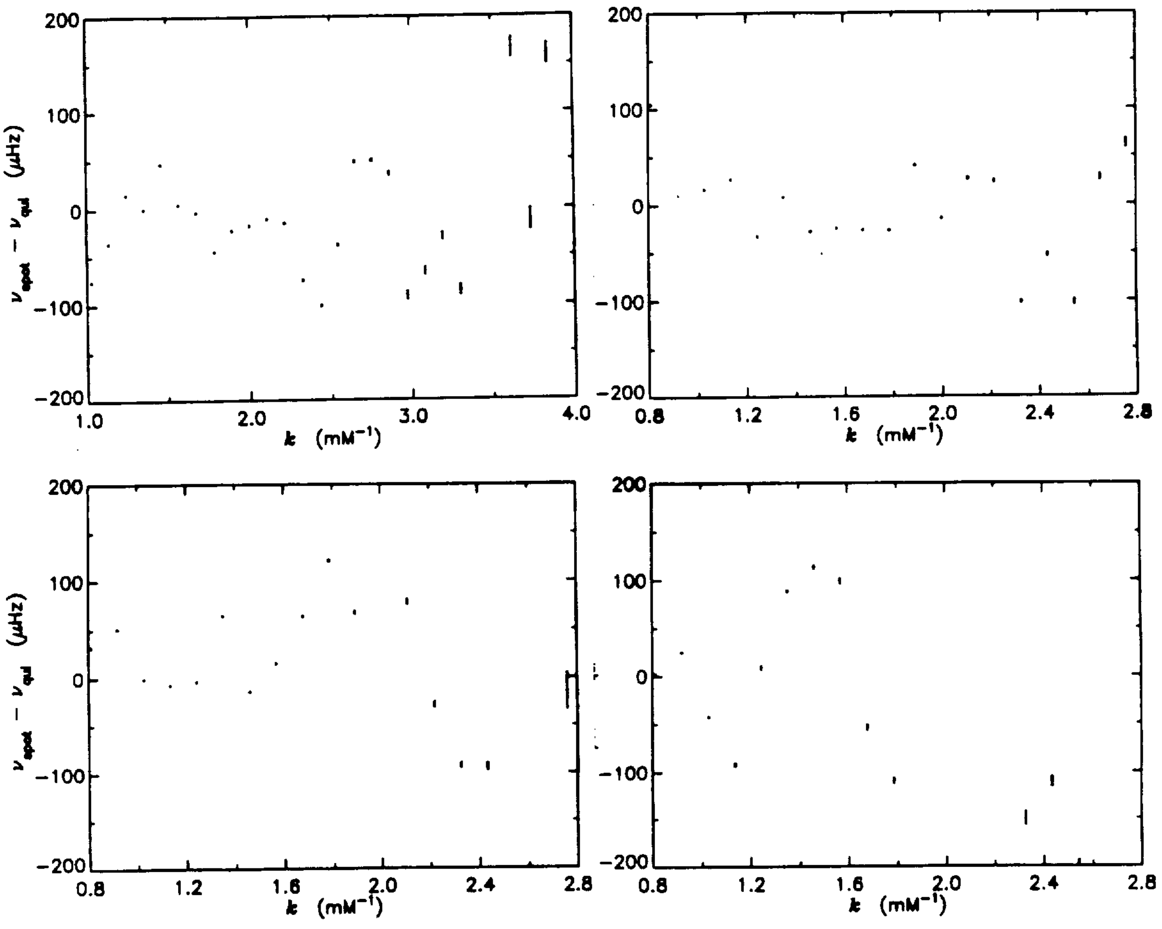

Figure 6.17: Mode frequency differences for sunspot and quiet subfields. Top left, *f*-mode; top right, p_1; bottom left, p_2; bottom right, p_3.

Chapter 7

Spatial Distribution of Power

The spatial distribution of power was measured for groups of modes, as well as for the sub-fundamental region of the power spectrum. To do this, the set of dopplergrams $V(\vec{x},t)$ was masked using $W(\vec{x})$ from equation 2.33, and a 3-d FFT, calculated for the full field of view. A spectral mask $M(\vec{k},\nu)$ was then applied to the Fourier transform to remove all but a small range of wavenumbers of a given ridge. An inverse Fourier transform of this masked 3-d spectrum yielded velocity $V_M(\vec{x},t)$ for a specific set of modes.

$$V_M(\vec{x},t) = \mathcal{F}^{-1}\Big\{M(\vec{k},\nu)\,\mathcal{F}^3\{W(\vec{x})\,V(\vec{x},t)\}\Big\} \tag{7.1}$$

The mean power was calculated at each pixel to make a velocity power map $P_M(\vec{x})$.

$$\begin{aligned} P_M(\vec{x}) &\equiv \frac{1}{T}\int_0^T |V_M(\vec{x},t)|^2\,dt && (7.2)\\ &= \frac{1}{T}\int_{-\nu_{\rm nyq}}^{\nu_{\rm nyq}} \Big|\mathcal{F}_S^{-1}\Big\{M(\vec{k},\nu)\,\mathcal{F}^3\{W(\vec{x})\,V(\vec{x},t)\}\Big\}\Big|^2\,d\nu && (7.3)\end{aligned}$$

where $\mathcal{F}_S^{-1}$ denotes the spatial, inverse Fourier transform.

7.1 Mode Masks

Masks were constructed for the f through p_3-modes in 6 wavenumber ranges. In addition, two sub-fundamental and a high frequency set of masks were made for the same wavenumber ranges. The mask limits are shown in figure 7.1. Three-dimensional masks were made from these 2-d limits by rotating the loci in the azimuthal direction. To account for the foreshortening, the rotation followed ellipses described by equation 6.1.

7.2 Results

Two sample power maps are compared with a magnetogram and an H α image in figure 7.2. Only the central disks of the frames are visible due to the apodizing window. The sub$_1$-f and f-mode maps were both made for the wavenumber range $1.95 < k/\mathrm{Mm}^{-1} < 2.31$. This is equivalent to a wavelength of about 4″, or 3 Mm. The mottled appearance of the power maps is an artifact of random interference of waves in a finite time series. The sub$_1$-f map shows little variation other than an overall trend of higher power in the upper right hand corner. The f-mode map shows a depression in power in the active region.

A selection of power maps is shown in figure 7.3. An estimate of the RMS velocity in each map can be obtained from figure 7.4. The power in high wavenumber modes is depressed in the active region. At low wavenumbers, the active region has little effect on the power. The sub$_1$-f and sub$_2$-f maps show no correlation of power with magnetic field at any wavenumber. The high frequency maps, though not shown in figure 7.3, looked very similar to p-mode maps of the same wavenumber range at lower frequency. There is little difference between the f, p_1, p_2, and p_3 maps for a given wavenumber range.

A horizontal slice through the f-mode map from figure 7.2 was made above the sunspot. The slice was low pass filtered using a Gaussian impulse response function (16 bin *fwhm*). See figure 7.5. This low pass filtered slice is compared with the magnetogram signal in figure 7.6. The power depression is significantly broader than the spatial extent of the photospheric magnetic field. It is narrower than the canopy field at ~ 1200 km, as can be seen from the H α image in figure 7.2. The filaments visible in H α are streams of gas traveling along magnetic field lines. The filaments, thus, trace out the field lines which form a canopy above the photosphere and lower chromosphere.

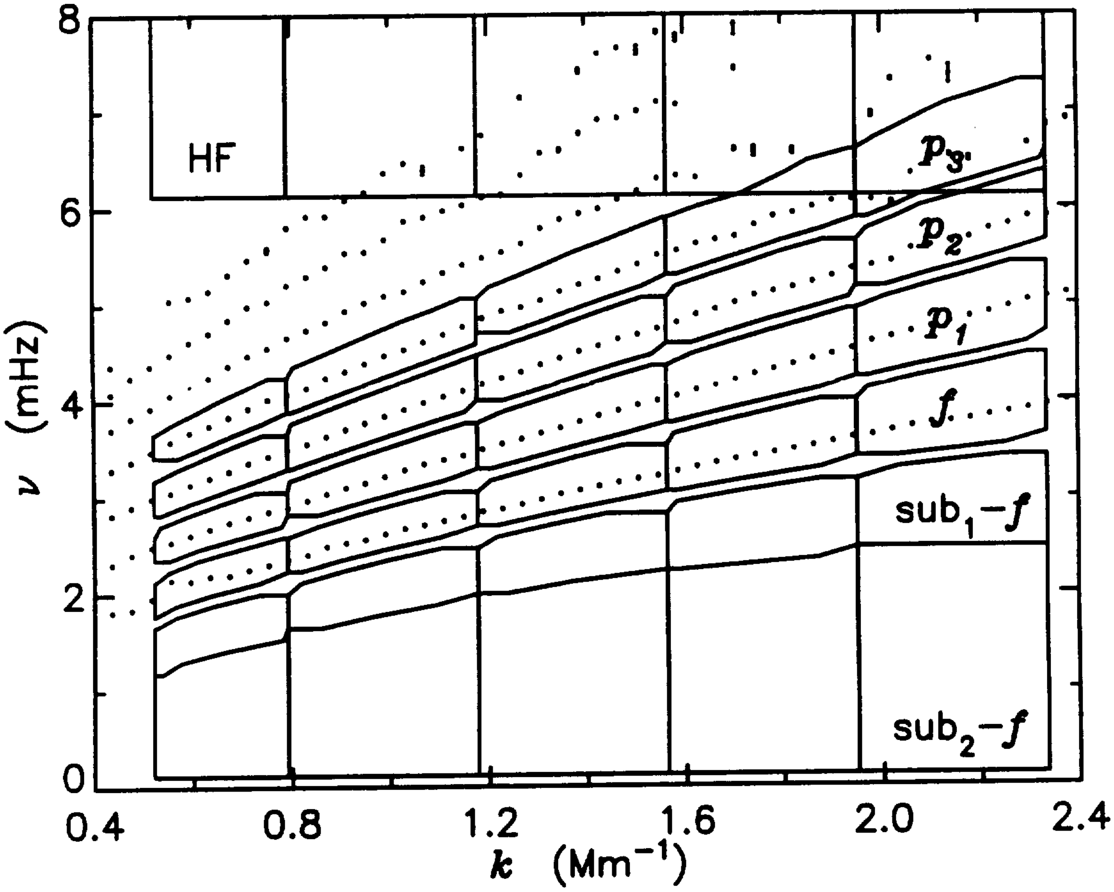

Figure 7.1: Masks for power distribution maps. Measured mode frequencies are shown as dots. Mask limits are shown as solid lines. The high frequency (HF) masks covered the range $6.0 < \nu/\mathrm{mHz} < 10.0$; the p-mode mask limits were set halfway between modes; the f-mode limits were set equidistant from the f-mode; the sub_2-f band extends from the f-mode down to $\nu = 0$; the sub_1-f band is the same width as the f-mode band. It is a subset of the sub_2-f band.

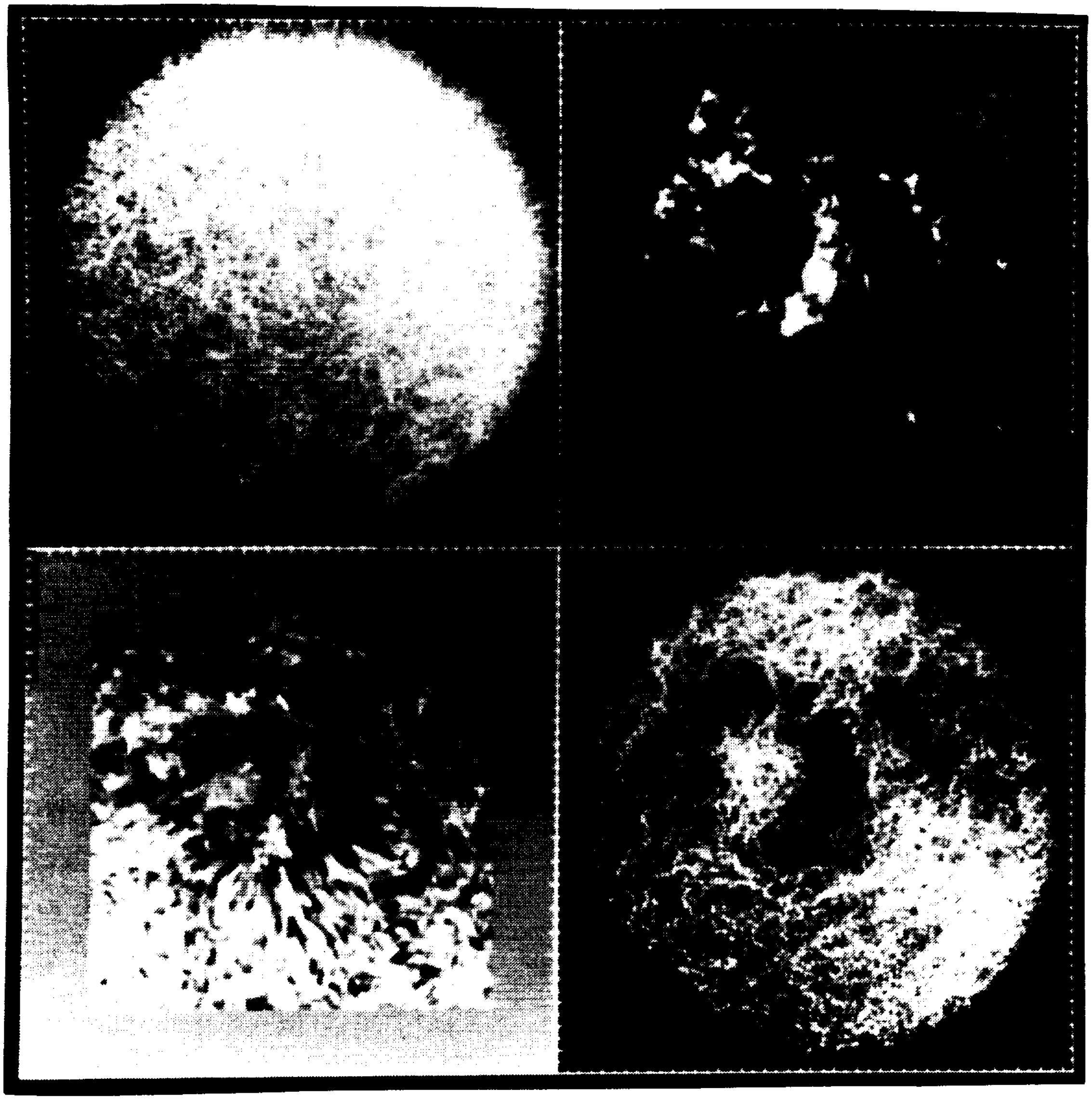

Figure 7.2: Comparison of power maps with magnetic fields. Top left: log power for sub$_1$-f ($1.95 < k/\mathrm{Mm}^{-1} < 2.34$). Top right: absolute value of magnetogram (log scale). Bottom left: Hα − 100 mÅ image. Bottom right: log power for f-mode ($1.95 < k/\mathrm{Mm}^{-1} < 2.34$). The small tick marks are 5″.

ORIGINAL PAGE
BLACK AND WHITE PHOTOGRAPH

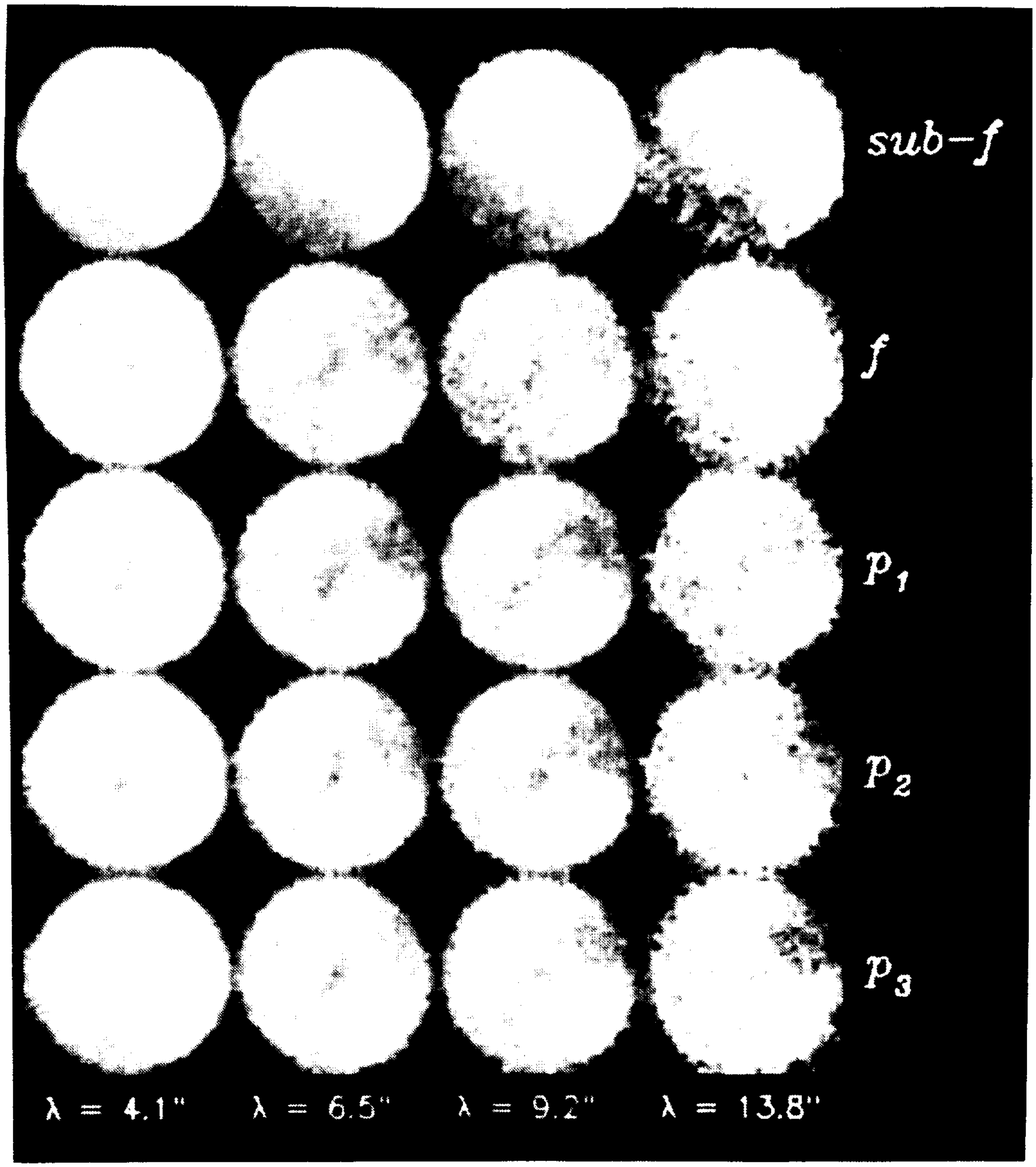

Figure 7.3: Power distribution for selected masks. Log power is displayed for sub_2-f, f, p_1, p_2, and p_3 maps with wavenumber ranges: [1.95, 2.34], [1.17, 1.56], [0.78, 1.17], [0.51, 0.78] Mm^{-1}.

ORIGINAL PAGE
BLACK AND WHITE PHOTOGRAPH

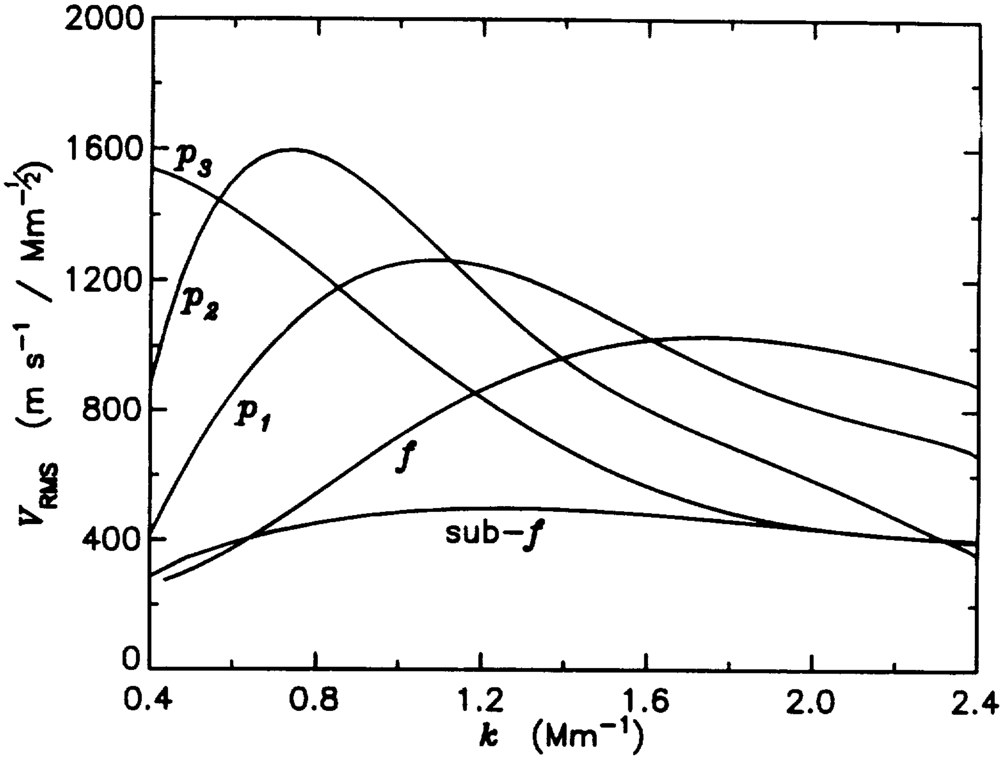

Figure 7.4: RMS velocity vs. k. Curves fitted from quiet subfield velocity spectrum. Curve labeled sub-f is taken from the background fit.

It is surprising that the sub-fundamental power is not correlated with magnetic field. The RMS convective power in the photosphere is a factor of 2 lower in plage (network field) than in nearby quiet regions (Title *et al.* 1992). Moreover, the sub$_2$-f band lies just below the f-mode band, but shows completely different behavior. At the same wavenumber, and almost the same frequency, oscillation amplitudes are reduced in active regions, whereas non-oscillatory motion is not.

It is impossible to distinguish between instrumental backgrounds and solar backgrounds from a single data set. It is difficult, however, to come up with an observational effect that would produce the measured background. Filter transmission variation should affect only the very low wavenumber part of the spectrum. Seeing variations should be independent of frequency; whereas, the observed background decreases with frequency.

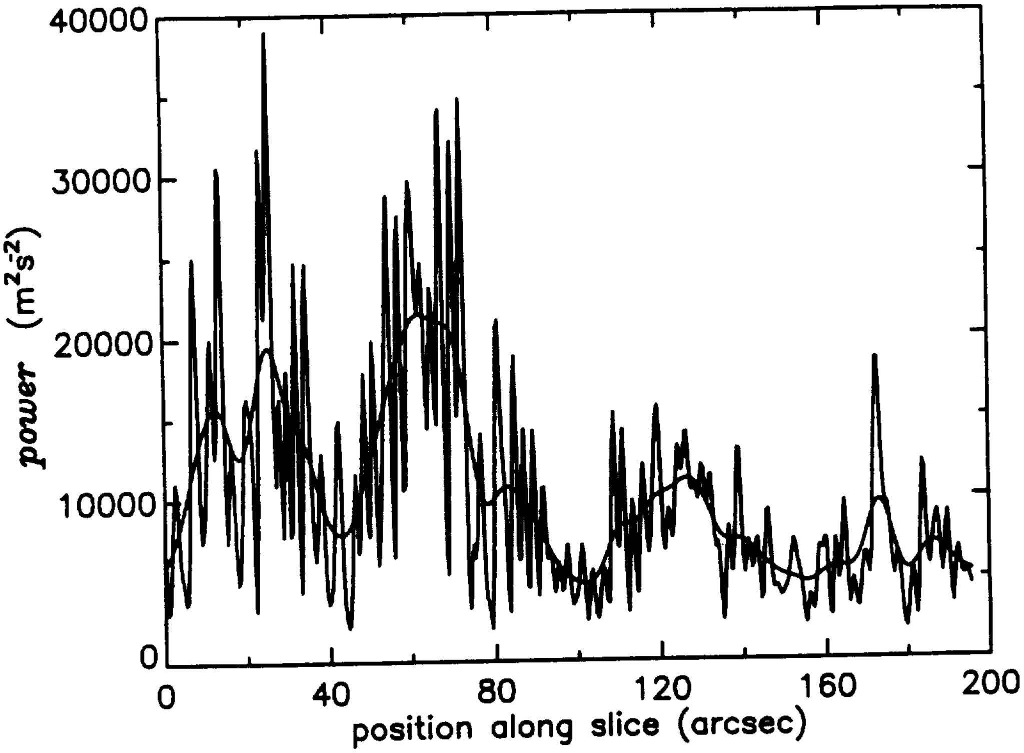

Figure 7.5: Slice of *f*-mode map. Horizontal slice from the [1.95, 2.34] Mm^{-1} map. Also shown is a low pass filter of the slice.

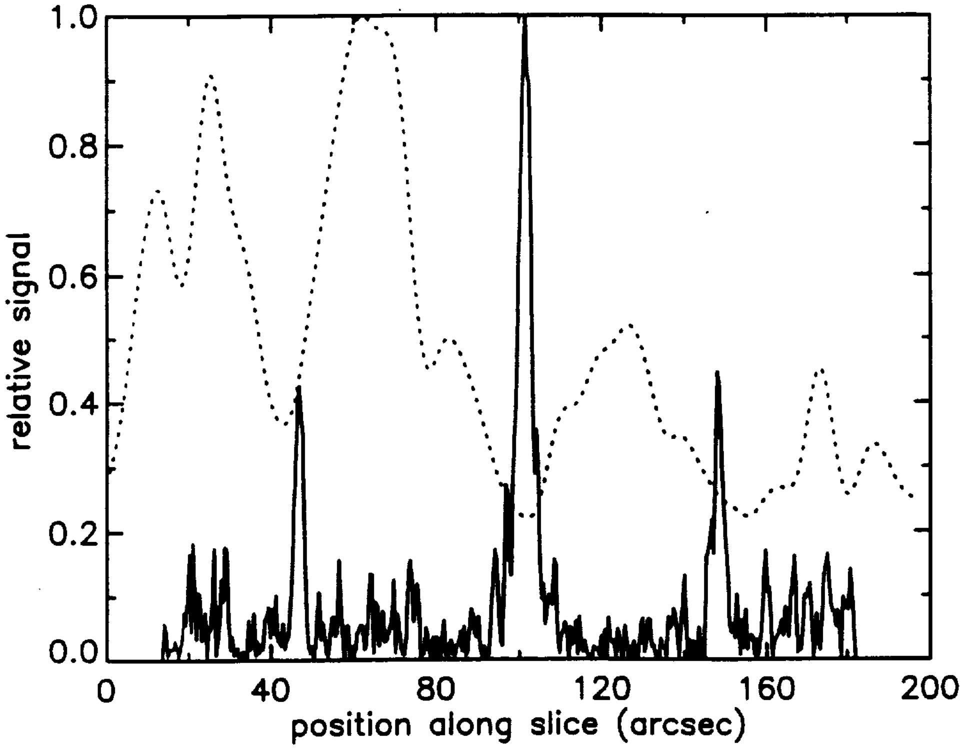

Figure 7.6: Comparison of f-mode slice with magnetic field. Dashed line shows low pass filter of slice (arbitrary scale). Solid line shows magnetogram signal (arbitrary scale).

Chapter 8

Conclusions and Discussion

8.1 Surfaces and Cavities

The existence of a chromospheric cavity is expected to produce a resonance consisting of a horizontal band of power and "avoided crossings" at about 5.5 mHz. (See figure 1.4.) This cavity is required by the model of Balmforth & Gough (1990) to explain the existence of high frequency modes. The p-mode and f-mode ridges shown in figures 6.4 and 6.9 are clearly visible at 5.5 mHz, but there is not a horizontal band of power nor are there "avoided crossings". The clear absence of this resonance in our data shows that there is no chromospheric cavity. Either the reflection coefficient at the base of the corona is too low or the surface is too irregular to form a good cavity.

This result supports the alternate hypothesis of Kumar *et al.* (1990), that the high frequency ridges are a purely geometrical artifact. The result is in agreement with the conclusion of Woodard & Libbrecht (1991); and it contradicts the claim of Damé *et al.* (1984) that there is a horizontal ridge of power at 5.5 mHz. Our power spectrum has a significantly better signal to noise ratio than that of Damé *et al.*

The f-modes are sensitive to conditions in the chromosphere and transition region. The fact that f-mode frequencies are lowered at high wavenumber may indicate interaction with chromospheric magnetic fields, energy leakage into the corona, or horizontal inhomogeneities in the chromosphere-corona boundary. The last of these three possibilities is interesting from the standpoint of acoustic cavities. Perhaps irregularities in the interface between the chromosphere and corona are responsible for both lowering the f-mode frequencies, and for reducing coherent reflection of acoustic waves.

8.2 Waves in Magnetic Fields

There is no frequency shift for f and p-modes in magnetic network fields of 100 – −1000 gauss to within the scatter of the data (~ 50 μHz). This limit is not stringent enough to determine whether the frequency shifts measured by Woodard *et al.* (1991) result from small shifts over the whole disk, or larger local shifts, in active regions, which contaminate the full-disk measurement. The modes measured by Woodard *et al.* have widths of order 1 μHz. Hence, to contaminate such a measurement, mode frequencies in active regions would have to be distributed within a few μHz of the quiet sun values. A measurement of such precision would require observations of at least 20 hr duration, assuming the waves are coherent for the observing period. At La Palma, 20 hours of observations can be made in two days. Hence, the waves would add coherently if the mode lifetime is ≥ 34 hr. If the mode lifetime is less than this, the signal to noise ratio increases only as the square root of time, so a much longer observing time would be necessary.

Power maps for oscillations in the low chromosphere show that, at high wavenumber, wave amplitudes are suppressed 15 Mm outside of the photospheric magnetic field. (See figure 7.6.) In the photosphere, the power is suppressed within one (horizontal) wavelength from the field (Tarbell *et al.* 1988). The vertical distance between the photospheric and chromospheric observations is under 0.5 Mm, and the (true) wavelength of the oscillations is ~ 2 Mm. Diffraction cannot account for the spreading of the region of the power depression because the waves have traveled less than one wavelength in the interval over which the spreading occurs. The power suppression must, therefore, be produced by interaction of the oscillations with the field *in the layer in where the waves are observed.*

The area containing magnetic flux was not measured directly at the height of the observations. Its extent can be inferred, however, from the magnetogram made in the mid-photosphere, and the H α image in the mid-chromosphere. The field lines spread out rapidly above the photosphere. Hence, the extent of the field at the observed height should be intermediate between the limits of the mid-photospheric and mid-chromospheric fields. This is consistent with the above conclusion.

The *f*-modes propagate without compression, so they produce no pressure fluctuations in the region where oscillations are suppressed. The mechanism suppressing the wave motion must, therefore, act through the velocity fluctuations.

8.3 Directions for Future Work

The frequency measurements presented here show the existence of high frequency and high wavenumber oscillations. They show general characteristics of the dispersion relations such as the smooth continuation above the acoustic cutoff. They are not, however, high precision measurements in comparison with existing low wavenumber observations. Precision of the measurements can be improved with longer observing times. This would improve the signal to noise ratio, and enable better fitting of the background and ridges. With better frequency resolution, it would become necessary to correct the fitted frequencies for their weighting with mode power (Korzennik 1991).

Important characteristics of the solar oscillations can be inferred from their phases (Deubner & Fleck 1989, 1990; Fleck & Deubner 1989). Trapped and nontrapped oscillations can be distinguished by the phase difference between velocity and intensity measurements. Propagating and evanescent waves can be distinguished by the phase lag between velocities at different heights in the atmosphere. An attempt was made to measure velocity-intensity phase differences. The attempt failed, possibly because of the large height range included in the measurement (see section 1.4), and possibly because of the large number of modes included in a single frequency bin (Braun *et al.* 1992a).

The interaction of magnetic fields with oscillations can be better quantified by measuring both wave amplitudes and magnetic fields at a range of heights in the atmosphere. Improvements that have been made to the tunable filter system since the 1990 observing season will allow Doppler measurements *restricted* to either the core or wings of the Na D_1 line. In addition, magnetograms can be made in the core or wings of the line by finding the difference between dopplergrams made with left and right circularly polarized light.

Braun *et al.* (1992b) report halos of enhanced high frequency acoustic power around active regions. A search was made for such halos in power maps made with the HF masks shown in figure 7.1. No enhancement of power was found. This does not contradict the result of Braun *et al.*, as they measured intensity fluctuations in the photosphere, in a lower wavenumber regime. It would be interesting to repeat the analysis with continuum brightness measurements for a field of view of at least 6 arc minutes.

The cause of the sub-fundamental background is, currently, unknown. Experiments should be done to discriminate between observational and solar backgrounds. For example, a set of filtergrams taken at fixed wavelength with a high cadence could be used to make artificial dopplergrams, and check the effect of seeing on background. Another set of filtergrams taken at the nominal, observing wavelengths could be made, using integrated sunlight, to check the effect of filter-transmission variation on background.

An attempt was made to find the oscillation sources described by Brown (1991). A temporally high-pass filtered movie of velocities was scanned visually for evidence of spatially and temporally localized sources of power. No good candidates were found. A better method might be to construct the two-dimensional acoustic Pointing vector described by Braun *et al.* (1992b). Large positive divergences of this vector field for high-pass filtered data could point out oscillation sources.

Appendix A

Frequency Tables

Table A.1: Mode frequency $\nu \pm \sigma_\nu$ (μHz) as a function of wavenumber k (Mm^{-1}) — measured from dopplergrams. For $k < 3.82$ Mm^{-1}, frequencies are taken from the full-field spectrum. At higher k, values from the quiet-subfield are tabulated.

k	0.399		0.437		0.475		0.513		0.551		0.589	
f	--		1815	12	1839	12	1959	13	2150	13	2142	12
p1	2223	13	2314	13	2415	13	2493	13	2545	13	2616	13
p2	2744	11	2824	11	2910	11	3002	11	3061	11	3146	11
p3	3191	13	3295	13	3377	13	3479	13	3587	13	3683	13
p4	3537	16	3711	16	3830	16	3930	16	4066	16	4166	16
p5	--		4080	24	4251	25	4369	24	4490	24	4620	24
p6	--		4369	57	--		--		5052	57	5084	57

k	0.627		0.665		0.703		0.741		0.780		0.818	
f	2191	12	2200	12	2257	12	2308	12	2363	12	2409	12
p1	2685	13	2751	13	2802	13	2861	13	2903	13	2978	13
p2	3214	11	3281	11	3364	11	3432	11	3501	11	3560	11
p3	3750	13	3839	13	3929	13	4021	13	4075	13	4141	13
p4	4249	16	4372	16	4479	16	4558	16	4666	16	4744	16
p5	4716	24	4853	24	4991	24	5040	24	5213	25	5301	24
p6	5152	57	5323	57	5474	57	5578	62	5808	58	5921	57

k	0.856		0.894		0.932		0.970		1.008		1.046	
f	2497	12	2535	12	2570	12	2626	12	2683	12	2720	12
p1	3048	13	3110	13	3160	13	3226	13	3291	13	3348	13
p2	3637	11	3710	11	3775	11	3845	11	3912	11	3989	11
p3	4243	13	4314	13	4394	13	4476	13	4539	13	4618	13
p4	4826	16	4941	16	5025	16	5097	16	5146	16	5247	17
p5	5396	25	5542	24	5552	24	5684	25	5871	25	5911	25
p6	5922	57	6093	58	6173	57	6370	57	6470	57	6397	71

k	1.084		1.122		1.160		1.198		1.236		1.274	
f	2762	12	2804	12	2859	12	2885	12	2933	12	2986	12
p1	3393	13	3437	13	3502	13	3558	13	3608	13	3667	13
p2	4049	11	4110	11	4180	11	4242	11	4301	11	4379	11
p3	4698	13	4777	13	4865	13	4937	13	4976	13	5046	13
p4	5337	16	5419	16	5488	16	5548	17	5636	17	5793	17
p5	5977	25	6034	25	6113	25	6142	28	6346	25	6573	25
p6	--		6624	93	6760	93	--		7144	94	--	

k	1.312		1.350		1.388		1.426		1.464		1.502	
f	3041	12	3079	12	3117	12	3158	12	3193	12	3222	12
p1	3721	13	3780	13	3842	13	3895	13	3948	13	3996	13
p2	4443	11	4514	11	4573	11	4643	11	4688	11	4749	11
p3	5140	13	5211	13	5267	13	5342	13	5415	13	5511	13
p4	5883	17	5942	17	5991	17	6086	17	6175	17	6306	17
p5	6602	30	6777	27	6914	25	6928	25	7001	26	7092	26
p6	--		7417	96	7598	93	7656	93	7629	103	7821	94

k	1.540		1.578		1.616		1.654		1.692		1.730	
f	3270	12	3313	12	3356	12	3391	12	3429	12	3458	12
p1	4048	13	4110	13	4157	13	4208	13	4274	13	4323	13
p2	4811	11	4892	11	4946	11	5015	11	5094	11	5134	11
p3	5556	13	5628	13	5671	13	5703	14	5818	14	5911	15
p4	6335	17	6314	17	--		6606	23	6581	54	--	
p5	7068	26	--		--		7439	28	--		--	
p6	7758	100	--		--		7901	146	--		--	

k	1.768		1.806		1.844		1.882		1.920		1.958	
f	3495	12	3531	12	3569	12	3616	12	3639	12	3682	12
p1	4374	13	4428	13	4480	13	4538	13	4613	13	4659	13
p2	5177	11	5232	11	5290	11	5366	11	5396	11	5440	12
p3	5944	14	6008	13	6065	14	6084	14	6079	14	6043	25
p4	6588	36	--		--		--		6957	33	7322	20
p5	--		--		8008	30	--		8074	28	--	
p6	--		8554	93	8695	96	--		8651	130	--	

k	1.996	2.034	2.072	2.110	2.148	2.186
f	3726 12	3760 12	3773 12	3796 12	3834 12	3867 12
p1	4708 13	4758 13	4810 13	4858 13	4909 13	4964 13
p2	5572 11	5600 12	5653 12	5684 12	5772 12	5819 12
p3	6350 14	6485 15	6539 19	6496 28	--	--
p4	--	7520 20	7373 93	--	--	--
p5	--	8423 30	8527 26	--	--	--
p6	--	--	9237 94	--	--	--

k	2.224	2.262	2.300	2.339	2.377	2.415
f	3901 12	3943 12	3982 12	4003 12	4022 12	4053 12
p1	5031 13	5066 13	5107 13	5159 13	5215 13	5261 13
p2	5896 12	5903 12	5987 12	6031 12	6074 12	6110 13
p3	6656 17	6843 20	6909 19	6882 20	--	7015 35
p4	--	8090 33	8070 31	8115 27	--	8389 55
p5	--	--	8917 28	8950 30	--	9181 32
p6	9617 97	--	9539 99	9569 100	--	--

k	2.453	2.491	2.529	2.567	2.605	2.643
f	4090 12	4123 12	4128 12	4195 12	4257 12	--
p1	5331 13	5361 14	5369 14	5427 14	5498 14	--
p2	6184 15	6189 13	6315 13	6250 13	--	--
p3	--	7084 35	7201 21	7177 31	--	--
p4	8394 26	8414 81	8168 76	--	8339 34	--
p5	9247 27	9361 34	9549 43	--	--	--

k	2.681	2.719	2.757	2.795	2.833	2.871
f	4302 12	4316 12	4364 12	4414 12	4436 12	4439 12
p1	5623 14	5658 14	5707 15	5768 14	5773 15	5804 14
p2	6630 21	--	6801 29	6825 17	6738 20	--
p3	7350 42	--	--	--	--	--
p4	8228 101	--	--	--	--	8830 76

k	2.909	2.947	2.985	3.023	3.061	3.099
f	4503 12	4515 12	4510 13	4561 13	4573 13	4569 13
p1	5880 16	5905 15	--	5999 18	6053 17	6000 19
p2	7096 30	--	--	--	--	--

k	3.137	3.175	3.213	3.251	3.289	3.327
f	4642 13	4643 13	4666 13	4711 13	4776 14	4793 14
p1	6077 19	6210 18	6314 18	6343 18	6324 49	6287 19

k	3.365	3.403	3.441	3.479	3.517	3.555
f	4853 14	4799 16	4767 15	4829 16	4889 17	4946 17
pl	6327 22	6405 25	6418 26	6491 28	6589 32	6753 24

k	3.593	3.631	3.669	3.707	3.745	3.783
f	4951 16	4969 30	4974 26	5061 27	5064 19	5058 19
pl	--	6494 76	6552 81	--	--	--

k	3.821
f	5153 18

k	3.840	3.948	4.056	4.164	4.272	4.380
f	5172 48	5205 48	5324 49	5380 49	5375 49	5565 49

k	4.489	4.597	4.705	4.813	4.921	5.029
f	5698 51	5775 51	5702 51	5810 56	5820 58	5883 65

k	5.138	5.246	5.354	5.462	5.570
f	6013 70	5963 81	5967 86	6015 83	6026 103

Table A.2: *f*-mode frequency $\nu \pm \sigma_\nu$ (μHz) as a function of wavenumber k (Mm^{-1}) — measured from intensities.

k	0.399	0.437	0.475	0.513	0.551	0.589
f	--	1810 12	1748 12	--	--	2089 11

k	0.627	0.665	0.703	0.741	0.780	0.818
f	2093 11	2176 11	2228 11	2281 11	2318 11	2373 11

k	0.856	0.894	0.932	0.970	1.008	1.046
f	2472 11	2515 11	2563 11	2610 11	2655 11	2692 11

k	1.084	1.122	1.160	1.198	1.236	1.274
f	2754 11	2793 11	2846 11	2876 11	2931 11	2981 11

k	1.312	1.350	1.388	1.426	1.464	1.502
f	3023 11	3066 11	3103 11	3147 11	3173 11	3209 11

k	1.540	1.578	1.616	1.654	1.692	1.730
f	3258 11	3302 11	3336 11	3361 11	3412 11	3438 11

k	1.768	1.806	1.844	1.882	1.920	1.958
f	3482 11	3520 11	3547 11	3581 11	3615 11	3641 11

k	1.996	2.034	2.072	2.110	2.148	2.186
f	3690 11	3724 11	3740 11	3773 11	3811 11	3842 11

k	2.224	2.262	2.300	2.339	2.377	2.415
f	3862 11	3890 11	3931 11	3967 11	3996 11	4026 11

k	2.453	2.491	2.529	2.567	2.605	2.643
f	4067 11	4097 11	4117 11	4154 11	4191 11	4204 11

k	2.681	2.719	2.757	2.795	2.833	2.871
f	4245 11	4283 11	4306 11	4336 11	4359 11	4368 11

k	2.909	2.947	2.985	3.023	3.061	3.099
f	4418 11	4424 11	4448 11	4491 12	4522 12	4525 12

k	3.137	3.175	3.213	3.251	3.289	3.327
f	4535 12	4564 12	4598 12	4646 12	4668 12	4660 13

k	3.365	3.403	3.441	3.479	3.517	3.555
f	4716 13	4726 14	4812 13	4832 14	4828 14	4902 14

k	3.593	3.631	3.669	3.707	3.745	3.783
f	4874 15	4910 17	4914 16	4948 16	4896 20	4961 20

k	3.821
f	5037 19

Bibliography

[1] Avrett, E. H., 1992, Workshop on the Solar Electromagnetic Radiation Study for Solar Cycle 22, ed. R. F. Donnelly, preprint.

[2] Balmforth, N. J., Gough, D. O., 1990, *Astrophys. J.*, **362**, 256–266

[3] Bogdan, T. J., Zweibel, E. G., 1987, *Astrophys. J.*, **312**, 444–456

[4] Bracewell, R. N., 1986, The Fourier Transform and Its Applications, 2 Ed., Rev., (New York: McGraw-Hill)

[5] Braun, D. C., Duvall, T. L. Jr., LaBonte, B. J., 1987, *Astrophys. J. Lett.*, **319**, L27–L31

[6] Braun, D. C., Duvall, T. L. Jr., LaBonte, B. J., 1988, *Astrophys. J.*, **335**, 1015–1025

[7] Braun, D. C., Duvall, T. L. Jr., LaBonte, B. J., Jefferies, S. M., Harvey, J. W., Pomerantz, M. A., 1992a, *Astrophys. J. Lett.*, in press.

[8] Braun, D. C., Lindsey, C., Fan, Y., Jeffries, S. M., 1992b, preprint.

[9] Bray, R. J., Loughhead, R. E., 1964, Sunspots, (London: Chapman)

[10] Bray, R. J., Loughhead, R. E., Durrant, C. J., 1984, The Solar Granulation, (Cambridge: Cambridge)

[11] Brown, T. M., 1991, *Astrophys. J.*, **371**, 396–401

[12] Campbell, W. R., Roberts, B., 1989, *Astrophys. J.*, **338**, 538–556

[13] Chitre, S. M., Davila, J. M., 1991, *Astrophys. J.*, **371**, 785–792

[14] Chou, D.-Y., LaBonte, B. J., Braun, D. C., Duvall, T. L. Jr., 1991, *Astrophys. J.*, **372**, 314–320

[15] Christensen-Dalsgaard, J., Gough, D. O., 1980, *Nature*, **288**, 544–547

[16] Damé, L., Gouttebroze, P., Malherbe, J.-M., 1984, *Astron. & Astrophys.* , **130**, 331–340

[17] Deming, D., Glenar, D. A., Käufl, H. U., Hill, A. A., Espenak, F., 1986, *Nature*, **322**, 232–234

[18] Deubner, F.-L., Fleck, B., 1989, *Astron. & Astrophys.* , **213**, 423–428

[19] Deubner, F.-L., Fleck, B., 1990, *Astron. & Astrophys.* , **228**, 506–512

[20] Duvall, T. L. Jr., Dziembowski, W. A., Goode, P. R., Gough, D. O., Harvey, J. W., Leibacher, J. W., 1984, *Nature*, **310**, 22–25

[21] Duvall, T. L. Jr., Harvey, J. W., Jefferies, S. M., Pomerantz, M. A., 1991, *Astrophys. J.*, **373**, 308–316

[22] Evans, D. J., Roberts, B., 1990, *Astrophys. J.*, **356**, 704–719

[23] Evans, D. J., Roberts, B., 1991, *Astrophys. J.*, **371**, 387–395

[24] Fernandes, D. N.,Scherrer, P. H., Tarbell, T. D., Title, A. M., 1992, *Astrophys. J.*, **392**, 000

[25] Fleck, B., Deubner, F.-L., 1989, *Astron. & Astrophys.* , **224**, 245–252

[26] Goldreich, P., Kumar P., 1988, *Astrophys. J.*, **326**, 462–478

[27] Goodman, J. W., 1968, Introduction to Fourier Optics, (San Francisco: McGraw-Hill)

[28] Gough, D. O., 1976, The Energy Balance & Hydrodynamics of the Solar Chromosphere & Corona, ed. R. M. Bonnet, P. Delache, (Clermont-Ferrand: G. de Bussac), 3–36

[29] Gough, D. O., 1983, *Phys. Bull.*, **34**, 502

[30] Gough, D. O., 1990, Progress of Seismology of the Sun and Stars, ed. Y. Osaki, H. Shibahashi, (Berlin: Springer-Verlag), 283–318

[31] Gough, D. O., Toomre, J., 1991, *Annu. Rev. Astron. Astrophys.*, **29**, 627–684

[32] Gough, D. O., 1992, private communication.

[33] Gurtovenko, E. A., Sheminova, V. A., Sarychev, A. P., 1991, *Solar Phys.*, **136**, 239–250

[34] Harris, F. J., 1978, *Proc. of the IEEE*, **66**, 51–83

[35] Harvey, J. W., 1991, private communication.

[36] Hill, F., 1988, *Astrophys. J.*, **333**, 996–1013

[37] Hollweg, J. V., 1988, *Astrophys. J.*, **335**, 1005–1014

[38] Jackson, J. D., 1975, Classical Electrodynamics, 2 Ed., (New York: Wiley)

[39] Jefferies, S. M., Pomerantz, M. A., Duvall, T. L. Jr., Harvey, J. W., Jaksha, D. B., 1988, Proc. Symp. Seismology of the Sun and Sun-Like Stars, ed. V. Domingo, E. J. Rolfe, (Noordwijk: ESA ESTEC), 279–284

[40] Jones, W. L., 1969, *Solar Phys.*, **7**, 204–209

[41] Knuth, D. E., 1986, The TEXbook, (Reading: Addison-Wesley)

[42] Kopp, G., 1990, Dissertation, Stanford University

[43] Korzennik, S. G., 1990, Dissertation, University of California at Los Angeles

[44] Kumar, P., Goldreich, P., 1989, *Astrophys. J.*, **342**, 558–575

[45] Kumar, P., Duvall, T. L. Jr., Harvey, J. W., Jefferies, S. J., Pomerantz, M. A., Thompson, M. J., 1990, Progress of Seismology of the Sun and Stars, ed. Y. Osaki, H. Shibahashi, (Berlin: Springer-Verlag), 87–92

[46] Kumar, P., Lu, E., *Astrophys. J. Lett.*, 1991, **375**, L35–L39

[47] LaBonte, B. J., Ryutova, M., 1992, *Astrophys. J.*, submitted.

[48] Lamb, H., 1932, Hydrodynamics, 6 Ed., (Cambridge: Cambridge)

[49] Lamport, L., 1986, LaTeX: A Document Preparation System, (Reading: Addison-Wesley)

[50] Leibacher, J. W., Stein, R. F., 1971, *Astrophys. Lett.*, **7**, 191–192

[51] Leighton, R. B., 1960, *Proc. IAU Symp.*, **12**, 321–325

[52] Libbrecht, K. G., 1988, *Astrophys. J.*, **334**, 510–516

[53] Libbrecht, K. G., Woodard, M. F., Kaufman, J. M., 1990, *Astrophys. J. Suppl.*, **74**, 1129–1149

[54] Nesis, A., Mattig, W., 1989, *Astron. & Astrophys.* , **221**, 130–136

[55] November, L. J., 1986, *Appl. Optics*, **25**, 392–397

[56] Palle, P.L., Regulo, C., Roca Cortes, T., 1989, *Astron. & Astrophys.* , **224**, 253–258

[57] Press, W. H., Flannery, B. P., Teukolsky, S. A., Vetterling, W. T., 1989, Numerical Recipes, (Cambridge: Cambridge)

[58] Roberts, B., 1991, private communication.

[59] Rosenthal, C. S., 1992, private communication.

[60] Scharmer, G. B., Brown, D. S., Pettersson, L., Rehn, J., 1985, *Appl. Optics*, **24**, 2558–2564

[61] Scherrer, P. H., Tarbell, T. D., 1988, *Bull. of the AAS*, **20**, 702

[62] Schleicher, H., 1976, Dissertation, University of Göttingen

[63] Schleicher, H., 1992, private communication.

[64] Schmieder, B., 1976, *Solar Phys.*, **47**, 435–460

[65] Snodgrass, H. B., Ulrich, R. K., 1990, *Astrophys. J.*, **351**, 309–316

[66] Stix, M., 1989, The Sun: an introduction, (Berlin: Springer-Verlag)

[67] Tarbell, T. D., Peri, M., Frank, Z. A., Shine, R. A., Title, A. M., 1988, Proc. Symp. Seismology of the Sun and Sun-Like Stars, ed. V. Domingo, E. J. Rolfe, (Noordwijk: ESA ESTEC), 315–319

[68] Title, A. M., Topka, K. P., Tarbell, T. D., Schmidt, W., Balke, C., Scharmer, G., 1992, *Astrophys. J.*, in press.

[69] Title, A. M., Rosenberg, W. J., 1981, *Optical Eng.*, **20**, 815–823

[70] Ulrich, R. K., Rhodes, E. J., 1977, *Astrophys. J.*, **218** 521–529

[71] Ulrich, R. K., 1970, *Astrophys. J.*, **162**, 993–1002

[72] Vernazza, J. E., Avrett, E. H., Loeser, R., 1981, *Astrophys. J. Suppl.*, **45** 635–725

[73] von der Lühe, O., 1988, *Astron. & Astrophys.* , **205**, 354–360

[74] Whitney, C., 1958, *Smithsonian Cont. Astrophys.*, **2**, 365

[75] Wolfram, S., 1988, Mathematica: A System for Doing Mathematics by Computer, (Redwood City: Addison-Wesley).

[76] Woodard, M. F., Kuhn, J. R., Murray, N., Libbrecht, K. G., 1991, *Astrophys. J. Lett.*, **373** L81–L84

[77] Woodard, M. F., Libbrecht, K. G., 1991, *Astrophys. J. Lett.*, **374** L61–L63

[78] Woods, D. T., Cram, L. E., 1981, *Solar Phys.*, **69**, 233–238